Dipl.-Ing. Hartmut Popp, MSc, BSc

State Estimation of Lithium-Ion Secondary Batteries by Means of Non-Destructive Mechanical Methods

PhD Thesis

to achieve the university degree of
Doktor der technischen Wissenschaften
Doctoral Programme: Information and Communications Engineering

submitted to
Graz University of Technology

Supervisor
Univ.-Prof. Mag.rer.nat. Dr.rer.nat. Alexander Bergmann
Institute of Electrical Measurement and Sensor Systems

Reviewer
Assoc.-Prof. Dr. Erik M. Kelder
Delft University of Technology, Faculty of Applied Sciences
Mekelweg 15, 2629 JB Delft, The Netherlands

Institute of Electrical Measurement and Sensor Systems
Head: Univ.-Prof. Mag.rer.nat. Dr.rer.nat. Alexander Bergmann

Vienna, December 2020

question (your) assumptions . . .

Affidavit

I declare that I have authored this thesis independently, that I have not used other than the declared sources/resources, and that I have explicitly indicated all material which has been quoted either literally or by content from the sources used. The text document uploaded to TUG-online is identical to the present PhD thesis.

16.12.2020 

Date Signature

Acknowledgements

First of all I want to thank my supervisor Alexander Bergmann. From the beginning he was very excited by this emerging topic and of great help and support throughout all the phases of the doctorate. Thanks to my reviewer, Erik Kelder for the helpful inputs regarding chemistry and the prompt processing of all the tasks that come with such a review.

A special thanks goes to Irina Gocheva for the (initial) discussions on the topic, the scientific review of all the papers and this thesis.

Thanks to my colleagues at AIT Austrian Institute of Technology GmbH where the main work of this thesis was performed. Helmut Oberguggenberger and Marcus Jahn for giving enough freedom to open this field of research in our company. Gregor Glanz and Kristijan Rajinovic for being my right hand each. Wernfried Berghold for support with test benches and applied measurement techniques in general. Hansjörg Kapeller, Marcus Jahn, Markus Koller and Martin Kriegisch for the scientific discussions and review of some of the chapters. A thousand thanks to Boschidar Ganev for linguistic corrections.

Cheers to Harald Brandstätter, who recommended signing up at the Institute of Electrical Measurement and Sensor Systems to conduct my studies under the supervision of Alexander Bergmann.

Thanks to all my co-authors of the manuscripts. Thanks to the staff and colleagues from Graz University of Technology. Thanks to Muhammad Luthfi for the exceptionally good work he did during his master thesis under my co-supervision. Thanks to all the others who supported this work in any kind of way.

Of course a special thanks to my family for being supportive over all those uncounted years of my education.

This work received financial support by the Austrian Research Promotion Agency (FFG) under the funding scheme 'Mobilität der Zukunft' within the collaborative research projects 'VALERIE' (Grant 865148) and 'MOGLI' (Grant 879610). The author wants to express his sincerest gratitude for the financial support.

Abstract

Lithium-ion secondary batteries are the ubiquitous source of electrical power for many applications nowadays, ranging from consumer electronics, over power tools to electric vehicles. Great progress has been achieved over the last years to bring down cost and to increase lifetime, performance and safety of lithium-ion secondary batteries by improving its (active) materials and its production process. Optimized operational strategies can further increase the use of the battery and bring down the total cost of ownership by facilitating it fully.

For this, precise knowledge of, among others, the state-of-charge and the state-of-health during the operational life of the battery is required. Knowledge of the cells internal state is also paramount for further research and development on lithium-ion secondary batteries. Hence, reliable methods for state estimation of lithium-ion secondary batteries are required. State-of-the-art battery management systems derive the parameters indirectly from the electrical two pole behaviour of the battery, which can lead to inaccurate values. Laboratory equipment on the other hand is mostly based on imaging methods which are bulky, expensive and most of the time cannot be used in-operando.

To overcome these issues, an alternative route is followed in this thesis by investigating non-destructive testing methods for their potential and their boundaries for monitoring lithium-ion secondary batteries as an inexpensive method which can be used in-operando. Acoustic methods in the audible and the ultrasonic region are deployed to lithium-ion secondary battery pouch cells and checked for their capability for state estimation under laboratory conditions and under realistic scenarios like dynamic load profiles and changing ambient temperature. While the methods in the audible region were found to be more suited for deriving mechanical parameters in laboratory which are useful for battery pack design than for state estimation, the ultrasonic methods were found to be suited for state estimation also under realistic conditions and for laboratory use to gain insights in the cell. In a detailed review of the recent state of non-destructive testing of lithium-ion secondary batteries expansion-based, force-based, strain-based, and acoustic emission methods were also investigated for their capabilities. Especially force- and strain-based methods show promising results for implementation in applications while expansion-based and acoustic emission methods are more suited to reflect internal processes in the laboratory.

Kurzfassung

Lithium-Ionen-Sekundärbatterien sind heute die allgegenwärtige Quelle elektrischer Energie für viele Anwendungen, die von der Unterhaltungselektronik über Elektrowerkzeuge bis hin zu Elektrofahrzeugen reichen. In den letzten Jahren wurden große Fortschritte erzielt, um die Kosten zu senken und die Lebensdauer, Leistung und Sicherheit von Lithium-Ionen-Sekundärbatterien zu erhöhen, indem die (aktiven) Materialien und die Produktionsverfahren verbessert wurden. Optimierte Betriebsstrategien können den Nutzungsgrad der Batterie steigern und so die Gesamtkosten über die Produktlebensdauer senken.

Dazu ist eine genaue Kenntnis unter anderem des Lade- und des Gesundheitszustands während des Betriebs der Batterie erforderlich. Die Kenntnis der Zell-internen Zustände ist auch für die weitere Forschung und Entwicklung von Lithium-Ionen-Sekundärbatterien von größter Bedeutung. Daher sind zuverlässige Methoden zur Zustandsabschätzung von Lithium-Ionen-Sekundärbatterien erforderlich. Moderne Batteriemanagementsysteme leiten die Parameter indirekt aus dem elektrischen Zweipolverhalten der Batterie ab, was zu ungenauen Werten führen kann. Laborgeräte hingegen basieren oftmals auf bildgebenden Verfahren. Diese Geräte sind sperrig, teuer und können meist nicht im laufenden Betrieb eingesetzt werden können.

Um diese Probleme zu überwinden, wird in dieser Arbeit ein alternativer Weg beschritten, indem zerstörungsfreie Prüfverfahren auf ihr Potenzial und ihre Grenzen für die Überwachung von Lithium-Ionen-Sekundärbatterien als kostengünstige Methode untersucht werden, welche auch in-operando eingesetzt werden können. Akustische Methoden im Hör- und Ultraschallbereich werden an Lithium-Ionen Pouch-Zellen erprobt und auf ihre Fähigkeit zur Zustandsabschätzung sowohl unter Laborbedingungen als auch unter realistischen Szenarien wie dynamischen Lastprofilen und wechselnden Umgebungstemperaturen geprüft. Während sich die Methoden im hörbaren Bereich eher für die Ableitung mechanischer Parameter im Labor, die für das Batteriepack-Design nützlich sind, als für die Zustandsabschätzung eigneten, erwiesen sich die Ultraschallmethoden für die Zustandsabschätzung auch unter realistischen Bedingungen und für den Laboreinsatz zur Gewinnung von Erkenntnissen in der Zelle als geeignet. In einer detaillierten Übersicht über den aktuellen Stand der zerstörungsfreien Prüfung von Lithium-Ionen-Sekundärbatterien wurden auch Expansions-, Kraft-, Dehnungs- und Eigenschallemissions-basierte Methoden auf ihre Eignung zur Abschätzung von Batterieparametern untersucht. Insbesondere Kraft- und Expansionsbasierte Methoden zeigen vielversprechende Ergebnisse für die Umsetzung in Anwendungen, während Dehnungs- und Eigenschallemissions-basierte Methoden besser geeignet sind, interne Prozesse im Labor abzubilden.

Contents

List of Figures

List of Tables

Nomenclature

Al	Aluminum
BMS	Battery management system
CB	Carbon black
CMC	Sodiumcarboxymethyl cellulose
Co	Cobalt
CO_2	Carbon dioxide
DOD	Depth-of-discharge
DUT	Device Under Test
EC	Ethylene carbonate
EIS	Electrochemical impedance spectroscopy
EMA	Experimental Modal Analysis
EMF	Electromotive force
Fe	Iron
FFT	Fast Fourier Transformation
FRF	Frequency Response Function
GWh	Gigawatt hours
H.P.	Hartmut Popp
HOMO	Highest occupied molecular orbital
LCO	Lithium-Cobalt-Oxide
LFP	Lithium-Iron-Phosphate

Li^+	Lithium-ion
LIB	Lithium-ion secondary battery
$LiPF_6$	Lithium hexafluorophosphate
LLI	Loss of lithium inventory
LMO	Lithium-Manganese-Oxide
LTO	Lithium-Titanium-Oxide
LUMO	Lowest unoccupied molecular orbital
Me	Metal
Mn	Manganese
NCA	Lithium-Nickel-Cobalt-Aluminium
NDT	Non-destructive testing
Ni	Nickel
NMC	Lithium-Nickel-Manganese-Cobalt-Oxide
PVDF	Polyvinylidene fluoride
SBR	Styrene butadiene rubber
Si	Silicon
SOC	State-of-charge
SOH	State-of-health
SOX	State-of-X
TCO	Total cost of ownership
TOF	Time-of-flight
US	Ultra-Sonic

Chapter 1

Introduction

This chapter gives an overview on the motivation and the objectives of this work, an outline, and the author's contribution to the scientific papers that were published as part of this cumulative thesis.

1.1 Motivation

Our today's society is strongly dependent on energy from fossil sources to power our economy and satisfy our everyday needs. In the year 2015, 81.7 % of the world's primary energy consumption was covered by coal, natural gas and oil [1]. Within the European Union the share of those sources amounted to 70.4 % in the year 2017 [2]. As fossil fuels are carbon-based and usually are burned to make their chemically stored energy accessible for our use, this energy mix leads to a significant output of carbon dioxide (CO_2) by humanity, which peaked at an all-time high of 22 gigatonnes CO_2 worldwide in 2019 [3]. CO_2 is a greenhouse gas and anthropogenic CO_2 plays a major role in global warming. Exhausts from burning fossil fuels also drive air pollution, negatively impacting our well-being and health with more than 400,000 premature deaths yearly in Europe alone [4]. To mitigate global warming and air pollution, a shift to energy from renewable sources is needed and is one of the biggest challenges of our modern society. The European Commission for example set a path with specific goals for reducing the emissions of the European Union. For the year 2030 the goals are

- 40 % cuts in greenhouse gas emissions,
- 32 % share for renewable energy, and
- 32.5 % improvement in energy efficiency

all compared to the year 1990 [5]. Transportation and electrical power generation are two main sectors where major de-carbonization is needed and achievable. In terms of transportation this calls for an electrification of the propulsion system as partially or pure electric drive trains have higher efficiency than drive trains that are solely based on internal combustion engines. Partial electrification leads to

drastically reduced overall and local emissions. Full electrification leads to zero local emissions and reduced or zero overall emissions, depending on the primary energy source the electrical power is converted from. In terms of electrical power generation, a shift to renewable sources like solar or wind is required. Those renewable sources have the drawback of being volatile and thus leading to unwanted fluctuations in electrical energy generation. So, for both tasks (de-carbonisation of transport and electrical energy generation), storage technologies for electrical energy are required.

The lithium-ion secondary battery (LIB) is seen as the technically and economically most viable storage technology solution for both sectors at the moment. Additionally, LIBs are widely used for other applications such as portable consumer devices and power tools. Considering these drivers, the total worldwide market for LIB is estimated to grow to 880 GWh (base scenario) or 1200 GWh (realistic scenario) in the year 2030 [6], which is at least 5.5 times more than in the year 2018 when the output amounted to 160 GWh. A main driver will be the cost of the storage system which is expected to fall by more than 50 % in the next decade [6, 7]. Costs can be saved by reducing material cost, reducing production and overhead cost and by reducing the cost of auxiliaries [7]. Another possibility is to reduce the total cost of ownership (TCO) of the LIB by maximizing its efficiency and cycle life and thus lowering the operational cost. Crucial for such optimized operation is the exact knowledge of battery state indicators like state of charge (SOC), depth of discharge (DOD), state of health (SOH) and temperature of the LIB (cell). Estimation of those values is performed by the battery management system (BMS). State-of-the-art BMS use the electrical two-pole behaviour of the battery in some cases combined with the temperature to estimate state of X (SOX) values, with X including a range of state values of interest. Estimation of SOX via the electric two pole response is an indirect way of measurement and can therefore suffer from insufficient data. This stands in the way of optimized operation and an alternative source of data to overcome these issues is required.

In LIB, but also for batteries in general, the physical properties change with cycling and over the operational life. This has a large impact on both safety of the system, as well as its use in second life applications. This also impacts the viability of some common market practices in the automotive industry, such as second hand car trade, which depends heavily on the life time expectation of the vehicle.

As lithium-ions (Li^+) are shuttled from anode to cathode during discharge and vice versa during charge, the electrode materials are altered in their morphology and subsequently their mechanical behaviour. As the battery ages by cycling and over time, its materials are also altered over its operational life by decay processes [8, 9]. This means, knowing the mechanical or physical properties of the cell, allows to determine both SOC and SOH or SOX in general. This is a direct way to measure SOX values. While this type of examination has been performed for decades on LIB in laboratories using imaging methods, in recent years also other non-destructive testing (NDT) approaches have received more attention [10]. Promising methods are analysis with dilation and resulting strain / force measurement, as well as inspection with acoustic analysis. These methods bear the potential for instrumentation in laboratories as well as implementation in applications as they are capable of in-situ and in-operando measuring. Improvements towards applicability, accuracy, cost reduction,

miniaturization, and reliability of these methods are required for further implementation. However, NDT mechanical methods can bring a reliable second source for estimation of SOX parameters without any cycling as well as for quick quality inspection of new and used cells and also contribute knowledge for further improvements of LIB by a better understanding of internal material-related phenomena during LIB operation.

1.2 Objective

This work aims to transfer the methods of NDT to LIB to reveal internal processes in-situ and in-operando. Special focus is on acoustic methods in the audible region and ultrasonic (US) probing. This approach is inspired by the bouncing tests [11] on alkaline primary battery cells, which change their mechanical behaviour drastically over the SOC: when dropped on a solid surface, fully charged batteries bounce several times, while empty ones do not bounce at all as changes in the internal morphology alter the mechanical behaviour of the cell drastically. As for example the graphite anode of LIB shows changes in volume of around 10 % during cycling [12] and this expansion can also be measured on the outside of the cell [10, 13], the hypothesis of this work is that these physical changes must be also be observable from the outside by applying acoustic methods.

To examine this hypothesis, different acoustic methods are investigated mainly for their ability to reveal changes in mechanical behaviour like stiffness and damping from the outside and their correlation with the SOX of the cell. The methods developed should be suited to monitor the behaviour continuously during operation, without influencing the device under test (DUT). All the methods should be evaluated both for laboratory use and their potential for implementation. So for validation realistic scenarios are chosen in terms of power profiles and operational temperature.

First, excitation with sound in the audible region is investigated. An electrodynamic shaker in combination with an impedance head is used to excite 20 Ah commercial pouch cell with frequencies from 20 Hz to 3 kHz. This is done for new and aged cells. The evolution of the frequency response function (FRF) is then used to analyse the mechanical behaviour of the cell over SOC and SOH and for various temperatures. These interdependencies and correlations are provided and elaborated in terms of their information content regarding the cell state.

Second, the possibilities of US diagnosis are examined. Special focus is on reducing the complexity of the system to bring it from the laboratory approach, where its applicability is already proven [14–18], closer to application. To reduce complexity and cost, mainly the excitation and the measurement and post-processing of the signal provide room for improvement. For actuators and sensors, piezo transducers like those demonstrated in [16–18] are already a low-cost and low-complexity design. Furthermore, this method is to be checked for proper operation with dynamic load profiles and different temperatures like those which can be found in applications.

Third, with NDT testing on LIB, as already stated, being a relatively new and emerging topic, a detailed and comprehensive review of the methods (without imaging methods) is still missing. The different approaches presented in today's literature have to be examined with regard to their suitability

and the possibilities they offer for use in the laboratory as well as for battery management systems within application.

Last, a summary of the whole topic of NDT in LIB, the current status and an outlook are given.

1.3 Outline

This cumulative dissertation is based on three open-access peer-reviewed journal publications that can be found in the appendix (see appendix B, C and D) and are listed in Tab. 1.1. All are focused on NDT of LIB for estimation of SOX. In paper 1 [19] mechanical frequency response function (FRF) and experimental modal analysis (EMA) are performed in order to estimate SOC and SOH of a commercial LIB pouch cell; in paper 2 [20] the applicability of US probing of LIB pouch cells for SOC estimation under real-world conditions is investigated, the focus being on implementation of the method for BMS; in paper 3 [10] a comprehensive review of non-destructive mechanical testing methods for LIB is given. This review includes methods based on volume change (dilation, strain and force) as well as EMA, US probing and acoustic emission (AE) approaches.

To complement these papers the main body of this thesis first provides additional theoretical background on LIB and NDT; second, the context and interdependencies of the published articles are elaborated; and third, the scientific progress achieved on the topic and an overall conclusion is given.

Table 1.1 Table of peer reviewed articles.

Paper 1,	Hartmut Popp, Gregor Glanz, Karoline Alten, Irina Gocheva, Wernfried Berghold, Alexander Bergmann; 'Mechanical Frequency Response Analysis of Lithium-Ion Batteries to Disclose Operational Parameters'; Energies, 11(3) (2018), Paper Number 541; https://doi.org/10.3390/en11030541
Paper 2,	Hartmut Popp, Markus Koller, Severin Keller, Gregor Glanz, Reinhard Klambauer, Alexander Bergmann; 'State Estimation Approach of Lithium-Ion Batteries by Simplified Ultrasonic Time-of-Flight Measurement'; IEEE Access, 7 (2019), Pages 170992 - 171000; https://doi.org/10.1109/ACCESS.2019.2955556
Paper 3,	Hartmut Popp, Markus Koller, Marcus Jahn, Alexander Bergmann; 'Mechanical Methods for State Determination of Lithium-Ion Secondary Batteries: A Review'; Journal of Energy Storage, 32, (2020), Paper Number 101859; https://doi.org/10.1016/j.est.2020.101859

1.4 Authors' Contributions to the Articles

Table 1.2 lists the contribution of the authors to the journal publications. Focus of the list is on the contributions from the author of this thesis (Hartmut Popp (H.P.)).

Table 1.2 Authors' contributions to scientific articles.

Paper 1,	Hartmut Popp (H.P.) is first author, conceived and designed the experiments and test setups, monitored the experimental phase, did the data analysis with assistance of Gregor Glanz, Karoline Alten, Irina Gocheva and Alexander Bergmann, coordinated all the activities and wrote the original draft with support of the co-authors, reviewed the work together with Irina Gocheva, Karoline Alten and Alexander Bergmann, and performed the activities concerning submission. Gregor Glanz did the main part of the practical testing with support of H.P.. Wernfried Berghold did the programming and adaptation of the test benches and the automated test setup.
Paper 2,	H.P. is first author, conceived and designed the experiments and test setups, monitored the experimental phase, did the data analysis and the estimator strategy, coordinated all the activities and wrote the original draft with support of the co-authors, reviewed the work together with Alexander Bergmann, and performed the activities concerning submission. The electronics for the BMS were designed by H.P. in collaboration with Markus Koller, who also performed the full coding part for the electronics. Gregor Glanz, Markus Koller and H.P. did the practical testing. Severin Keller, Reinhard Klambauer and Alexander Bergmann did the calculation for the velocities of sound waves in the battery and wrote major parts of the section 'theoretical background' and the 'appendix'.
Paper 3,	H.P. is first author, did the conceptualization of the paper with Marcus Jahn and Alexander Bergmann, performed the literature review, wrote the original draft with support of Markus Koller for the section 'Implementation', did the formal analysis, writing review & editing with support of the co-authors, coordinated the writing process and performed all activities concerning submission. The section 'Other relevant phenomena' was mainly written by Marcus Jahn with partial support of H.P..

Chapter 2

Fundamentals of Lithium-Ion Secondary Batteries

This section gives an introduction to LIB and provides relevant information for understanding of the subsequent content of this work. First, the working principle of LIB is explained; second, the mechanical setup and materials are summarized; third, information on safe operation and ageing are given and fourth, common electrical test methods for LIB are briefly elaborated.

2.1 Working Principle

The system known as LIB is a secondary battery, meaning it is rechargeable. Since the desired source- and end- product is electrical energy, but the energy is stored chemically, conversion between those states is required upon charging and discharging. LIBs are electro-chemical converter and chemical storage in one unit. This distinguishes them from fuel-cells or flow-cells where energy conversion and energy storage take place in different components. This brings the benefit of easy handling but the drawback of the energy content being coupled with the size of the converter [8].

LIBs are galvanic or voltaic cells consisting of a pair of electrodes (positive and negative), an electrolyte, usually a separator and a casing. State-of-the-art LIB cells have a more complex architecture which is explained further. In fig. 2.1 the working principle is shown. As LIBs operate on a rocking chair principle, neither the anode (negative electrode) nor the cathode (positive electrode) consist of pure metallic lithium, which would otherwise cause safety issues due to its intrinsic nature of forming dendrites upon plating and stripping off the metal surface (see also sec. 2.2.1). Rather, Li^+ are stored in host lattices. In the case of the anode, this host lattice is nowadays mostly graphite and in the case of the cathode mostly lithium-metal-oxides or lithium-metal-phosphates [8–10, 21]. Upon discharge the Li^+ is solvated on the surface of the anode and travels, driven by the electromotive force (EMF), through the electrolyte and the separator to the cathode, where it is de-solvated on the surface. When charging, the process is vice versa. To balance the difference in charge, an electron e^- has to travel over the electrical circuit, so an electrical current is established. In eq. 2.1, 2.2 and 2.3

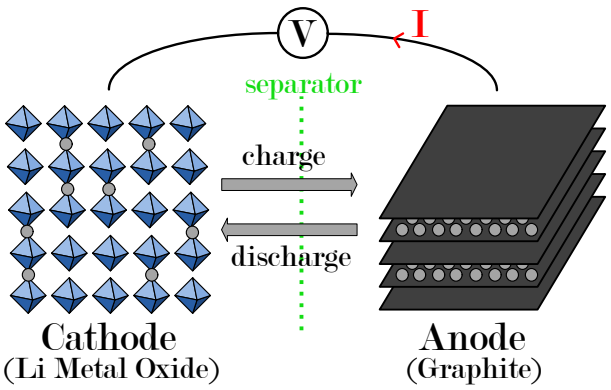

Figure 2.1 Working principle of LIB (modified from [10]) (CC BY 4).

the reaction equation for each electrode and the overall cell is shown in an exemplary way for a cell with a graphite (C_6) anode and a Lithium-Cobalt-Oxide (LCO) ($LiCoO_2$) cathode [8, 21]. This LCO / graphite system was the first commercialised LIB technology [21]. For other materials the reaction equation can vary.

$$\text{Anode: } nC + xLi^+ + xe^- \Longleftrightarrow Li_xC_n \tag{2.1}$$

$$\text{Cathode: } LiCoO_2 \Longleftrightarrow Li_{1-x}CoO_2 + xLi^+ + xe^- \tag{2.2}$$

$$\text{Overall cell: } LiCoO_2 + nC \Longleftrightarrow Li_{1-x}CoO_2 + Li_xC_n \tag{2.3}$$

Many cathode materials are not suited to be fully de-lithiated. So in eq. 2.2 this means $x < 1$. In the case of LMO, x is at maximum 0.5. Graphite can be fully de-lithiated with $0 \leq x \leq 1$ [8]. However, due to an overhang (overdimension) of the anode, this is usually not the case [10, 22, 23]. More information on LIB materials can be found in sec. 2.2.

Nowadays LIB cells are produced in two main formats, prismatic and cylindrical; while the prismatic ones can be further divided into hard case- and soft- case cells [10]. Soft- case prismatic cells commonly are referred to as pouch cells. In fig. 2.2 those cell formats are shown. Cylindrical cells mostly have a lower maximum size than the other types and thus have typically a maximum capacity of < 10 Ah. The other formats are available in larger casings ranging from a few Ah up to over a hundred Ah [8].

In fig. 2.2 also the typical mechanical setup of LIB cells is shown. It is composed of different layers of anodes and cathodes with separators in between. The electrodes are made of current collector foils that are coated with the electrode material, which consists of active material, conductive additive and polymeric binder. For the anode the foil consists of copper and has a typical thickness of around 9 to 12 µm. For the cathode aluminium is used and the typical thickness is around 12 to 20 µm due to its lower electrical conductance. The conventional coated active material layer thickness varies between 30 µm and 200 µm on either side of the current collector, depending on whether the cells are power or energy cells. Also the compression and thus the loading (g/cm^2) of the active material is very different

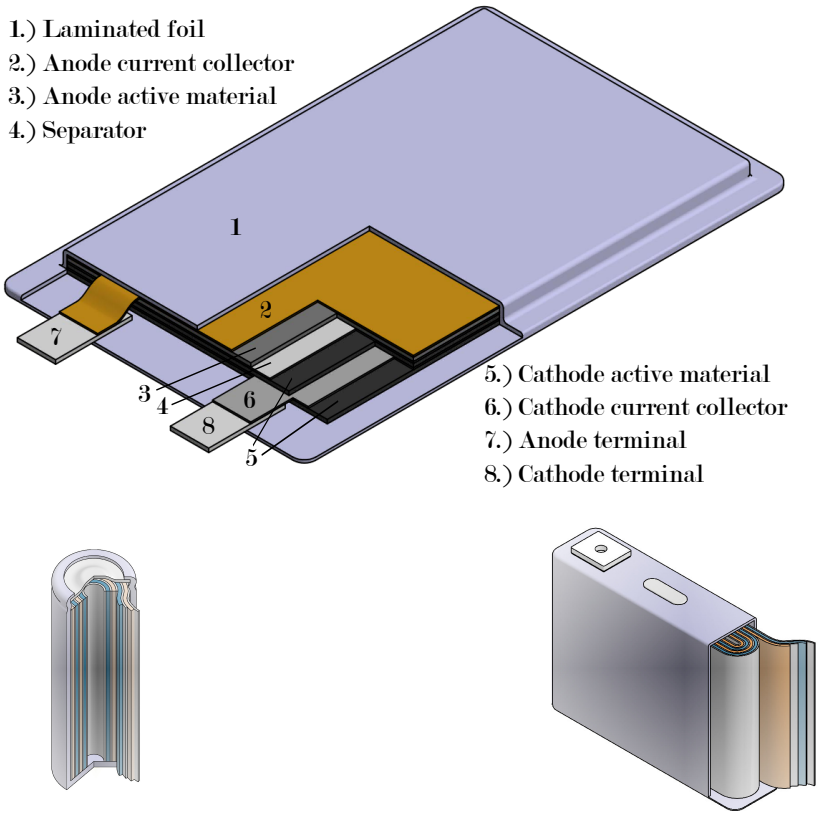

Figure 2.2 Sketch of pouch (top), cylindrical (bottom left) and prismatic cell (bottom right) (extended from [10] (CC BY 4)).

with power or energy cells. Power cells have lower compression of the layers. Thus the porosity is higher, leading to larger paths for ion diffusion and higher surface area for phase transition and thus lower impedance. High energy cells have higher loadings as more active material can intercalate more ions [8, 24].

2.2 LIB Materials

This section covers commonly used materials and promising future materials for LIB cells. The active materials used in the cell do not only influence the capacity and impedance but also the voltage of the battery due to the difference in electrode potential [8]. To have high energy density cells, the goal is to maximize operating voltage and cell capacity (eq. 2.4).

$$E_n = U_n \cdot C_n \tag{2.4}$$

With E_n being the nominal energy content in Wh, U_n being the nominal voltage in V, and C_n being the nominal capacity in Ah. So ideally, anode and cathode materials with high difference in electrode potential and high capacity have to be applied to get high-energy-density-cells. However, tradeoffs have to be made as other important parameters for active materials are the stability, safety and cost of the material, which often stand in opposition to the above-mentioned values. Thus, commercial state-of-the-art energy-optimized cells show an energy density of around 250 to 280 Wh/kg [22, 25] even when materials allowing for much higher energy density would be already available today. The most important points of common materials are discussed below in this section. The values given for the specific capacity of the material are always the theoretical ones. Experimental and typical ones are usually lower mainly because of reversible and non-reversible capacity (see tab. 2.2). For many materials not all of the theoretically available Li^+ can be removed without damaging the host structure significantly [26].

In general, active materials for LIBs are always composites. Usually they consist of the active material itself, but for better electrical conductivity a few percent of a conductive agent are added and to increase the cohesion also a few percent of a binder material acting as glue are required [24]. Very common materials for conductive agents are carbon black (CB) and for binders polyvinylidene fluoride (PVDF) is used on the cathode side and a mixture of styrene butadiene rubber and sodiumcarboxymethyl cellulose (SBR+CMC) is used for the anode side [27, 28]. Beside these commonly used ingredients, there may be additives e.g. for protective coating of the active material.

2.2.1 Anode

This subsection briefly summarizes the most commonly used and the most promising anode materials.

Lithium

Lithium is the third lightest element and the lightest solid one at ambient conditions. Is has the lowest reduction potential with -3.04 V versus the standard hydrogen electrode, and the smallest ionic radii among all candidates for metal-ion batteries. Its specific capacity is very high with 3860 mAh/g [25, 29, 30]. These properties render it the ideal candidate for use as anode in lithium batteries.

Lithium-metal batteries were developed in the 1970s. During the 1980s there were serious safety incidents of lithium-metal secondary batteries, leading to the transition to LIB in the early 1990s. Lithium-metal primary batteries are still on the market today. The biggest problem of lithium-metal secondary batteries is the disordered deposition of lithium during charging, leading to the growth of dendrites. These dendrites form spikes that can penetrate the separator, thus short-circuiting the cell, which can lead to fire or even more severe reactions [21, 25, 29, 30].

Nevertheless, due to its exceptional properties, research on lithium-metal anodes was never stopped and a lot of progress in terms of safety and cycle life has been made especially under 'mild' conditions with low current density and high excess lithium-metal [29]. For practical batteries,

further developments are required. Popular topics are ion-conductive protective layers and 3-D composite electrodes where lithium-metal is embedded in a host structure. Modifications on binders and electrolytes are also recent topics in research and development. For more information see reviews [29, 30]. Lithium-metal anodes are one of the most promising candidates for achieving 400 to 500 Wh/kg next generation cells especially combined with solid state electrolyte approaches [29, 30].

Graphite

Graphite since its introduction in the first commercial LIB in the year 1991 is still the most commonly used material for anodes in LIB. It has a specific capacity of 372 mAh/g and intercalation of Li^+ takes place at a potential between 0.25 and 0.01 V versus Li/Li^+ [10, 31–33]. This low potential is beneficial in terms of energy density, but it is below the electrochemical stability of, e.g., commonly used organic carbonate-based electrolytes, as these commonly decompose at about 0.8 V versus Li/Li^+ [33]. Thus a protective layer, the so-called solid electrolyte interface (SEI) is formed during the first cycles, hindering further decomposition. For more information see sec. 2.2.3 and 2.3. During cycling, graphite exhibits a change in volume of around 10 % between fully lithiated (LiC_6) and empty state (C_6). Cells with graphite-based anodes, depending on their design and purpose, achieve a cycle life between a few hundred to a few thousand cycles [22]. Graphite in combination with state-of-the-art cathode materials currently allows for energy densities of around 270 Wh/kg on cell level [22]. Incremental improvements are still possible.

Lithium-Titanate (LTO)

Lithium-Titanate anodes are made of Lithium-Titanium-Oxide ($Li[Li_{1/3}Ti_{5/3}]O_4$ = LTO). This type of anode has a comparatively low theoretical gravimetric capacity of 175 mAh/g. Also it has a very high potential of 1.55 V versus Li/Li^+ [34] leading to cells with low energy density. Nevertheless it is still a popular anode material because these properties bring other benefits. It is known as a zero strain material; this means there are no or only minimal changes of 0.1 to 0.3 % in volume with changing Li^+ [10] content leading to a very high cycle life of thousands of cycles. Its high potential is within the stable region of commonly used electrolytes (see sec. 2.2.3), thus no SEI is formed and decomposition processes are low. Additionally, deposition of lithium on the surface is very unlikely [34]. This renders it the ideal candidate where high-power, fault-tolerant and long-life cells are needed. Commercial batteries allow for constant charging and discharging rates of eight times the nominal current, a storage life of 25 years and a cycle life of over 25,000 cycles before the current capacity is below 80 % of the initial capacity [35].

Silicon

Silicon (Si) is a promising material for future high energy density cells. It has a specific capacity of 3579 mAh/g for $Li_{15}Si_4$, a potential between 0.37 and 0.45 V versus Li/Li_+ [36] and changes volume

between 280 to 400 % [10]. Silicon is the second most common element in the earth's crust mainly in form of silicon-dioxide and thus has high availability and moderate cost in its refined form. Si can bind oxygen and thus has a positive influence on cells under abusive conditions. Nevertheless, due to its extremely high changes in volume, Si anodes are not stable and lose a high share of their initial capacity irreversibly during the first cycles [36].

Other Anode Materials

Additional to the ones named above, also Aluminium- and Tin-based alloys could be used. Tin for example has a theoretical capacity of 993.4 mAh/g, is relatively cheap, but also faces changes in volume of around 300 % during cycling [10].

Summary Anode

There are several candidates for LIB anodes, all with their own pros and cons. At the moment, LTO and above all graphite are the most frequently used materials. Graphite also plays a role for future materials as it serves as a host or accompanying material for other higher-capacity materials such as lithium metal, silicon or tin [29, 30, 33]. Small amounts of silicon doping of around 1 % can be found already in commercial LIB cells [22], and the goal is to increase these values to 5 to 10 % in the mid term [10]. This is also a possible way of implementation for tin. The values for the energy densities given above are theoretical values for the pure material and cannot be reached in reality and of course vary for composite or alloy structures. Especially the high changes in volume of high capacity material are a limiting factor for practical anodes to even get close to the region of the theoretical capacity. In general it can be stated, that the higher the capacity, the higher the change in volume during cycling [10] and thus the higher the problems with mechanical stability (see sec. 2.3).

Tab. 2.1 shows a summary of the properties of anode materials. While not exceeding in any category, graphite shows the best tradeoff. This is why today it is found in every cell where higher energy content is needed [22, 32].

Table 2.1 Summary of anode materials' properties.

Material	Theoretical specific capacity (mAh/g)	Nominal potential vs. Li/Li^+ (V)	Stability	Safety
Lithium metal	3860	++	-	–
Graphite	372	+	+	+
LTO	175	–	++	++
Silicon	4200	∼	–	+

2.2.2 Cathode

This subsection briefly summarizes the most commonly used and the most promising cathode materials. In general cathodes mostly are realized as Li-Me-oxides with Me standing for metal, mostly Nickel (Ni), Manganese (Mn), Cobalt (Co), Iron (Fe) and/or Aluminium (Al) [10, 22].

Lithium-Cobalt-Oxide (LCO)

Lithium-Cobalt-Oxide ($LiCoO_2$ = LCO) was the cathode material for the first commercial LIB cell. Since then it was widely deployed and still is often found in consumer electronics since it has a high specific theoretical capacity of 274 mAh/g and a nominal potential of 3.8 V versus Li/Li^+ [26], low self-discharge and high cycle life under low currents. Due to its high Co content its price is above that of other common technologies. The implementation of Co additionally suffers from its toxicity and geopolitical challenges which have lead research to focus on lowering the Co content of cathodes, while maintaining a similar level of energy density found in LCO. Furthermore, LCO deteriorates quickly when subjected to higher currents. As cost and power are of high priority for electric vehicles, LCO cathodes do not play a role there [32].

Lithium-Nickel-Cobalt-Aluminium-Oxide (NCA)

Lithium-Nickel-Cobalt-Aluminium-Oxide ($LiNi_{0.8}Co_{0.15}Al_{0.05}O_2$ = NCA) cathodes have a specific theoretical capacity of 279 mAh/g and a nominal potential of 3.7 V versus Li/Li^+ [26]. They are basically the result of improving Lithium-Nickel-Oxide ($LNiO_2$ = LNO) electrodes which are thermally unstable and have low cycle life. By substitution with Co and small amounts of Al these effects can be mitigated, while mostly keeping the beneficial properties like potential, capacity and cost [26]. This is why the material is very popular for e.g. electric vehicles even when this material is more critical in terms of safety [32]. NCA changes its volume by about 4.5 % during cycling [10].

Lithium-Nickel-Manganese-Cobalt-Oxide (NMC)

Lithium-Nickel-Manganese-Cobalt-Oxide ($LiNi_{1-y-z}Mn_yCo_zO_2$ = NMC) nowadays is synthesised with different quantities of each material [22]. The classic form of this layered oxide-type electrode is $LiNi_{0.33}Mn_{0.33}Co_{0.33}O_2$ also called NMC111. This type of NMC has a specific theoretical capacity of 278 mAh/g and a nominal potential of 3.8 V versus Li/Li^+ [26]. In terms of expansion, data for NMC111 vary significantly. Values for changes in volume between -3.4 to 2.4 % are reported for de-lithiation [10]. Here too substitution of Co can reduce the cost and increase the overall capacity. Combinations such as NMC622 and NMC811 and others are under development [37] but also already found in commercial cells [22]. Nickel-rich NMC combinations face the same challenges in terms of cycle life and thermal stability as the LCO cathode [37]. Attempts to overcome these are ongoing.

Lithium-Iron-Phosphate (LFP)

Lithium-Iron-Phosphate ($LiFePO_4$ = LFP) cathodes have a specific theoretical capacity of 170 mAh/g and a nominal potential of 3.4 V versus Li/Li^+ [26]. Thus, they yield a lower energy density than the other common cathode materials. However, as Fe is inexpensive and the cathode itself has high cycle life, allows for high currents and shows safe behaviour it is employed often for applications where energy density is not crucial and/or high power and/or high cycle life are required. In terms of expansion it changes around 4.7 % during cycling [10].

Other

As already stated, the number of material combinations for cathodes is high. Beside the oxide structures (Li-Me-O_2 and partially Li-Me-O_3), also spinel (Li-Me-O_4) and olivine (Li-Me-PO_4) structures are commercialized and under research [26]. They can have high potential versus Li/Li^+ and in the case of spinel $LiMn_2O_4$, for example, can profit from the low cost and environmental friendliness of Mn. Before further implementation, cycle life and general stability have to be improved.

Summary Cathode

Currently, cathodes are mostly of the intercalation type realized with transition metals. The trend goes towards the increase of the electrodes' potential versus Li/Li^+ [26] and a reduction in cost. For an increase in potential, cathodes enabling a 5 V cell are realistic, but are currently hampered by electrolyte degradation beyond 4.5 V for commonly used electrolytes or 4.8 V for state-of-the-art high voltage electrolytes (see sec. 2.2.3). Cost can be reduced by minimizing the share of expensive metals, here mainly Co. A mixture of different materials and structures allows balancing several aspects like stability, cost, potential and capacity [38]. Tab. 2.2 provides a summary of the properties of the cathodes named above.

Table 2.2 Summary of cathode materials' properties [26].

Material	Specific capacity theor./pract. (mAh/g)	Nominal potential vs. Li/Li+ (V)	Stability	Cost
LCO	274/148	3.8	$\sim$	–
NMC111	278/160	3.8	$\sim$	-
LMO	148/120	4.1	-	+
LFP	170/140	3.4	++	++
NCA	279/199	3.8	+	$\sim$

2.2.3 Electrolyte

The electrolyte is a key component of the passive materials within LIBs. Electrolytes need to have low ionic impedance to mitigate high concentration polarizations during operation, which lead to faster ageing and low rate performance [21, 39]. Further requirements are [21]:

- Wide electrochemical stability window
- Low ionic impedance
- Low cost
- High thermal stability (translates to safety)
  - L ow melting point
  - H igh boiling point
  - H igh flashpoint
- Low toxicity
- Good processing
  - L ow viscosity
  - H igh wettability of electrodes and separator
  - H igh Li salt solubility of the solvents/matrix.

The stability window of a battery electrolyte is believed to be represented with the energy levels of highest occupied molecular orbital (HOMO) and lowest unoccupied molecular orbital (LUMO) of the solvent molecules (fig. 2.3). The electrochemical potential μ of the relevant active material for the anode (μ_{anode}) and cathode ($\mu_{cathode}$) should be both within the window of LUMO and HOMO to render the electrolyte stable from a thermodynamic point of view [33, 40]. Standard organic carbonate-based electrolytes e.g. lithium hexafluorophosphate ($LiPF_6$) in ethylene carbonate (EC) are stable between around 0.8 and 4.5 V versus Li/Li^+. Interfaces with materials that show values outside of this window lead to reduction or oxidation respectively [40, 39]. For cathodes this is not a problem for standard materials as they currently range up to 4.1 V versus Li/Li^+ (see sec. 2.2.2), while anodes like graphite with intercalation potentials of 0.25 down to 0.01 V versus Li/Li^+ are clearly outside this window [33, 39]. Graphite can still be used as a protective layer, the SEI, is formed, but this comes with disadvantages (see sec. 2.3).

However, as already stated, the goal is to have a large difference in potential between the positive and the negative electrode. This means that the potential of the cathode will also be higher, demanding for electrolytes to be stable above 4.5 V versus Li/Li^+. Extensive research is dedicated to this topic [26].

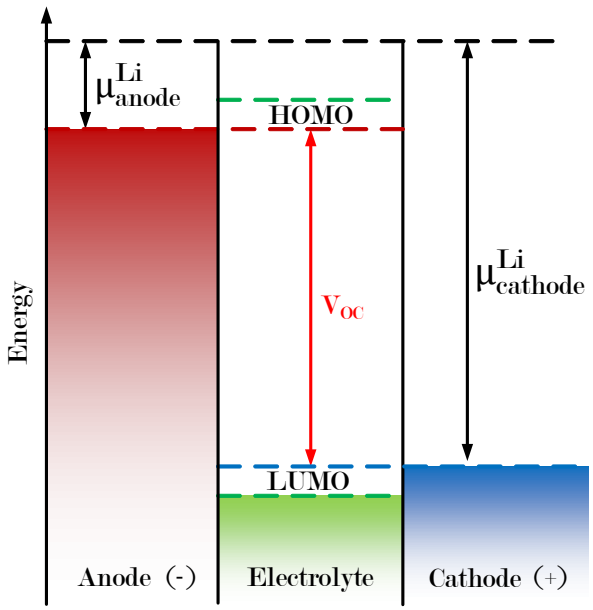

Figure 2.3 Energy levels of LIB cell electrode materials and electrolyte (own representation based on [40]).

2.2.4 Other passive components

Two other important passive components are the separators and the casing of the cell.

Separators for LIB ideally have high ionic conductivity while being electrically isolating. They also have a high impact on safety of the cell [41]. Shutdown separators, for example, irreversibly reduce their ionic conductivity by partial melting and consequent clogging of pores, when the cell temperature exceeds a certain temperature. Thus thermal runaway can be mitigated. From a mechanical point of view, the separator only plays a marginal role. It has a typical thickness between 16 and 25 µm and high porosity [41] and thus low stiffness and mass.

Casings for LIB vary significantly. As shown in fig. 2.2 they have different shapes and materials. The main goal is to preserve and contain the inner materials, to protect them mechanically and to seal them from the atmosphere [42]. Pouch cell casings usually are made of aluminium foil of around 40 µm thickness and additional synthetic materials on the inside and outside. The synthetic materials are for protection, isolation and heat sealing and can sum up to over 100 µm [43]. Hard-case cylindrical and prismatic cells are mostly made of aluminium. The thickness is around 0.2 to 0.3 mm for smaller cylindrical cells of format 18650 and 21700 [44] and around 1 mm for larger prismatic cells [45]. All forms of casings have a significant impact on the mechanical properties of the cell [10]. However, all cell formats are currently found within the EV market. No single format is dominating, which is partially down to their differences in possible capacity per cell as well as the ability to cool the cells during operation. Therefore, all formats have their application-specific advantages and disadvantages.

2.3 Ageing of LIB

LIB are subject to constant ageing, whether they are used or not. Also they age in every state, there are favourable conditions where ageing is slowed down [38, 39, 46]. As ageing is still of great concern, the following section elaborates this topic.

Ageing of the battery negatively impacts primarily its remaining capacity (capacity fade) and its impedance (impedance increase) [38, 39, 46]. Other values such as shorter operational range / time, lower power capability and higher heat generation can be derived directly from those two values. Ageing can be mainly classified in chemical ageing and in mechanical ageing. Chemical ageing takes place all the time, no matter if the cell is cycled or not; mechanical ageing is due to cycling. Chemical ageing mostly takes place in combination with the electrolyte (see sec. 2.2.3) [33, 38–40, 46]. As anode and cathode are subject to different phenomena, they are discussed separately below [38, 39]. The impact of ageing on the electrical values of the LIB is explained in sec. 2.4.

2.3.1 Anode Ageing

One of the main ageing mechanisms in state-of-the-art LIB cells with graphite anodes is the evolution of the SEI during the battery life [33, 38–40, 46]. As already discussed above, graphite (but also lithium metal and silicon) are outside the electrochemical stability window of standard electrolytes. Thus, a passivation film, the SEI, is formed on the surface which protects the anode and the electrolyte from further rapid degeneration. As depicted in fig. 2.4 the SEI forms during the first discharge cycle and matures during the subsequent cycles [33, 38–40, 46]. For formation of the SEI and also during its ageing, Li^+ is consumed. This leads to a loss of lithium inventory (LLI) which reduces the capacity of the battery. The SEI is not only permeable for Li^+ but also for other charged elements like anions and electrons or neutral elements like the solvent. So also during storage, side reactions on the anode are possible. Solvents can lead to exfoliation, creation of gases and can crack the SEI. Those cracks exhibit bare anode surface and thus lead to regrowth of the SEI there and also to consequent thickening of the SEI [38, 39]. The ageing of the SEI and the anode is fastest for $SOC > 80\,\%$, as the potential difference to the stability window of the electrolyte is the highest due to the high degree of lithiation of the anode. Under high cell temperatures, the SEI may dissolve and create lithium salts, which are less permeable for ions and thus increase the impedance of the electrode. Low temperatures can lead to reduced diffusion within SEI and graphite and thus increase the risk of lithium plating, which is the deposition of metallic lithium on the surface. Both effects lead to an increase of the electrode's impedance [38, 39, 46]. Even when the volume of graphite changes around 10 % between charge and discharge leading to strain and stress among the electrode material and its surroundings, structural changes are considered to only affect the ageing mildly [38, 39, 46]. In general, the SEI can be rendered stable enough to protect the anode and the electrolyte for years and / or hundreds to thousands of cycles.

A relatively new aspect for LLI, also explaining parts of the phenomenon of regenerative cycles / periods where the capacity increases up to 5 %, is the influence of the anode overhang. Here Li^+ is in

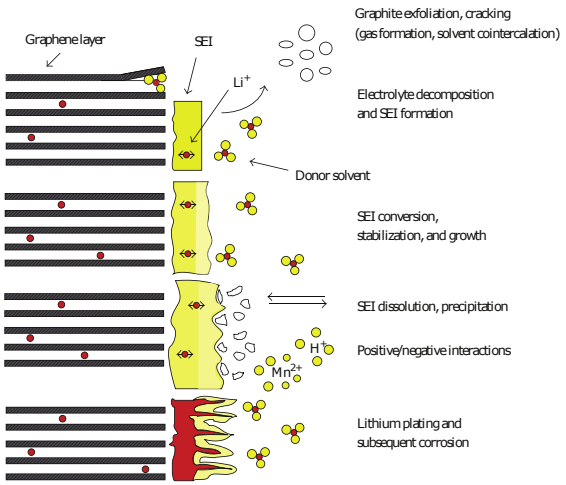

Figure 2.4 SEI evolution at the interface between anode and electrolyte [38] (CC BY 4).

the inactive regions of the anode where it does not overlap with the cathode and thus is not accessible under normal cycles [23, 47]. Li^+ can diffuse in this region e.g. under storage and also diffuse back under certain conditions.

Si also faces the formation of a SEI and additionally shows major mechanical disintegration due to its excessive change in volume. This leads to a rapid deterioration of its performance values, especially since the SEI is not stabilised. It therefore cracks and re-grows over the course of several cycles, leading often to a thick SEI that increases impedance by lowering ion transfer to and from the anode and to a LLI. For metallic lithium, see the problems stated in sec. 2.2.1.

For LTO, ageing is minimal as it does not form a SEI due to its high electrochemical potential within the stability window of the electrolyte and also it faces only minor expansion and contraction during cycling. Cells with LTO and LFP electrodes, for example, exhibit a cycle life of over 10,000 cycles.

2.3.2 Cathode Ageing

Cathode ageing is a complex topic as the materials, their mixtures and morphologies can be so different (see also sec. 2.2.2), as is their behaviour during ageing. In general, the cathode has a lower share of the overall cell decay than the anode [39]. Similar to the SEI on the anode a solid permeable interface forms also on the cathode [48]. This interface contributes to cathode ageing but has less impact on the overall ageing than the SEI [38, 39, 46]. Other general cathode ageing processes are shown in fig. 2.5.

Mechanically there is the wear of active mass because of cycling, with a resulting loss of contact between the active material (e.g. because of micro cracking) and conducting material. This can be increased by decomposition of the binder. When the contact is lost, the current collector is bared and subsequently becomes prone to corrosion, with corresponding local oxidation of the electrolyte.

Additionally to oxidation, the electrolyte degrades because of soluble species from other materials. Those materials mainly are dissolved from the cathode and can migrate through the electrolyte to the cathode, where they interact with the SEI and the anode materials. Some of the chemical processes involved can lead to the evolution of gas, mainly CO_2 [38, 39, 46].

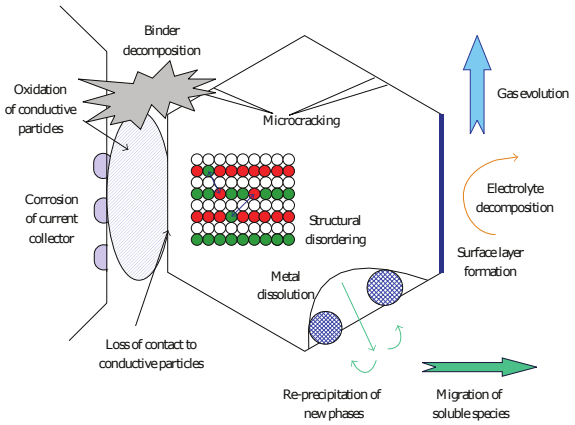

Figure 2.5 Ageing phenomena at the cathode [38] (CC BY 4).

Depending on the material there can also be crystal distortion due to phase transitions. This applies to e.g. LMO where its $LiMn_2O_4$ spinel has a cubic structure with Mn located on octahedral 16d sites and Li^+ on 8a tetrahedral sites in a cubic close-packed array of oxygen anions. During phases with low cathode potential (below 3 V versus Li/Li^+), the structure changes to a Jahn-Teller distorted $Li_2Mn_2O_4$ tetragonal phase by insertion of Li^+ in vacant octahedral sites [38, 46]. A subsequent significant phase change leads to mechanical damage of the cathode and thus to fading performance. Another drawback of this material is that Mn can be dissolved by the electrolyte, leading to a decrease of the capacity on the cathode side and further interference of this Mn with other components in the cell [38, 46]. The crystal distortion and Me dissolution is most pronounced with LMO spinel, but can also take place with other chemistries.

2.3.3 Summary Ageing

Ageing is a major issue for LIB since it has a direct impact on its main operational values. Due to the formation of gases, buil-up of films, gassing and the mechanical disintegration of structures, also its mechanical properties are changed. However, modern LIBs show cycle lives and storage times that already exceed the lifetime of many of the products they power.

For applications, the determination of the SOH of the cell is still of high importance, as it determines its remaining operational time or whether it can ensure operation at all, e.g. in terms of power. Until now, this task has been performed mainly by measurements based on the electrical values of the cell and with underlying models or statistical approaches [39]. In general these methods already show adequate precision and predictive accuracy when enough computational power and a

big enough dataset are available [39]. Mechanical methods, like those investigated in this thesis, have the potential to estimate SOH by analysing the materials properties, without knowledge of the cell history [10]. This is especially beneficial in case of e.g. second life classification of a cell.

2.4 Electrical Testing of LIB

Classical testing of LIBs is based on their electrical behaviour. The two main values that hold information about the system are its capacity and the (complex) impedance. Information about the cell and its condition can then be derived from these values. Capacity is determined by cycling and the impedance is determined by pulse or periodic excitation of the system without changing its SOC too much [8].

In fig. 2.6 the electric equivalent circuit of a LIB is shown. In this simple form it mainly consists of a voltage source that represents the open circuit voltage (OCV) of the cell and an impedance Z. The OCV is dependent on the SOC of the cell. The impedance reflects the drop in voltage due to internal over-voltages of the cell. These mainly consist of ohmic drops (e.g. electrical resistance of the conducting materials or ionic resistance of electrolyte and separator), charge transfer drops and diffusion drops [8, 49]. The resulting voltage on the terminals of the battery is the OCV minus the voltage drop on Z. Because of the effects involved, Z is dependent on time. Other influences like SOH, temperature and recent history of the battery have an impact on OCV and Z. In total, the electric two pole behaviour of LIB is non-linear [8, 9].

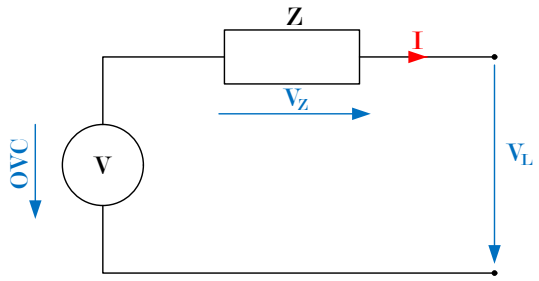

Figure 2.6 Electrical equivalent circuit of LIB.

The following sections describe briefly the electrical testing of LIB.

2.4.1 Capacity

The capacity (C) in Ah of a battery is the charge (Q) in As (conversion from As to Ah is performed by division of Q/3600) which can be transferred within its operational window with

$$Q = \int_0^\tau i(t)dt \tag{2.5}$$

for alternating currents or

$$Q = I \cdot t \tag{2.6}$$

for direct current. The current rate (C-rate) is the nominal capacity of the cell divided by an one hour period. So a discharge with a C-rate of 0.5 would theoretically mean a two hour discharge. For a cell with capacity of 10 Ah this would mean a current of 5 A. A discharge with a C-rate of 3 would lead to theoretical discharge time of 20 minutes. For a real application these values will differ. LIB usually are operated in a certain fixed voltage window with V_{MAX} for the maximum voltage during charge and V_{MIN} for the minimum voltage during discharge. With higher currents the limits are reached earlier due to the voltage drop caused by the internal impedance (see fig 2.6). In fig 2.7 the cell voltage over transferred capacity for various C-rates is shown as an example for a LIB cell with LFP cathode and graphite anode. The voltage is highest for the charge with the high C-rate and lowest for the discharge with the high C-rate because of the higher internal voltage drop V_Z due to cell impedance (fig. 2.6). As V_{MIN} is reached earlier because of the higher total drop in voltage, the capacity that can be withdrawn is lower. For charge this is also visible by longer phases with constant voltage at V_{MAX} where the current then is reduced to not overshoot this value [8]. In fig. 2.8 the development

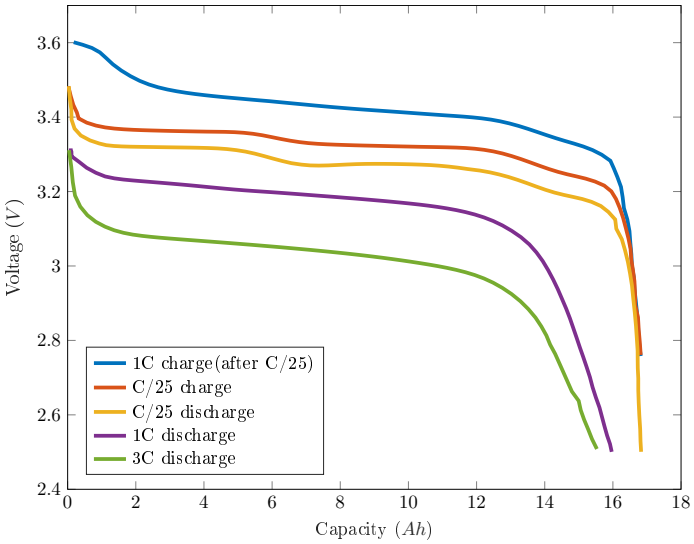

Figure 2.7 Charge and discharge curves of LIB cell for various C-rates (own representation based on [50]).

of the capacity over the withdrawn charge for several temperatures is shown for cylindrical cells with NCA cathode and graphite anode [51]. The cell capacity is checked by regular full charge- and discharge cycles to see the progress of the fade in total performance. In between also shallow cycles with less DOD can be conducted to evaluate different influences as ageing is not uniform over the full SOC (sec. 2.3). It can be seen that the loss in capacity first takes place rapidly and then slows down. This is due to electrochemical processes slowing down with time as they are approaching a more stable state [8, 39]. Fig. 2.8 also indicates the calendaric part of the overall ageing. This part of the ageing mainly is electrochemically induced, so it is lowest for lower temperatures, where the decomposition processes are slowest. However, it can be seen that the overall ageing is highest for the lowest temperature which is due to lithium plating at lower temperatures, leading to faster degradation

by cycling [51]. The impedance of the cell is not shown here, but it is to be assumed that it increases during cycling [8, 39].

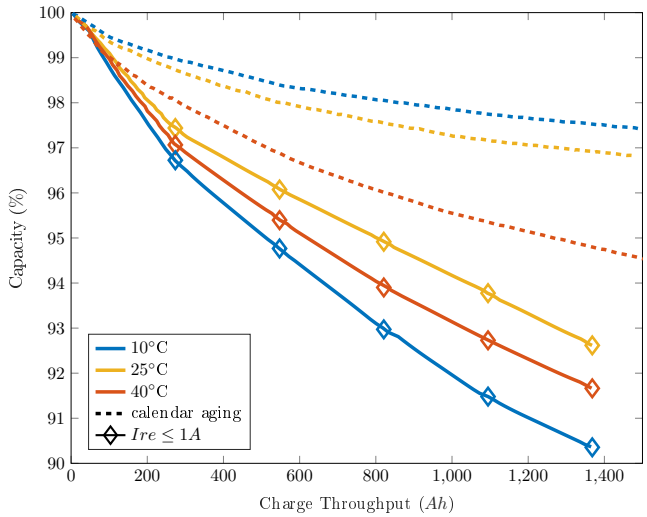

Figure 2.8 Development of LIB cell capacity over transferred charge (own representation based on [51]).

2.4.2 Impedance

As already mentioned above, the impedance has a significant impact on the overall cell performance. By measuring and analysing the impedance, valuable knowledge about cell-internal processes can be gained. There are two main methods to measure the impedance. They are i) current step or current pulse, and ii) electrochemical impedance spectroscopy (EIS),which are explained further in this section. In both cases the voltage response to an excitation with a current is measured. For EIS, an excitation with a voltage signal and measurement of the current response is also common. Determination of the impedance can be conducted at different SOC levels, so the changes occurring e.g. through lithiation states or electrode potentials can be observed.

In fig. 2.9 the response of a LIB to a rectangular current step is shown. The cell is in a relaxed state initially, so the cell voltage equals the OCV and the current is zero. When the current is applied, the cell immediately responds with an ohmic drop, which is caused by the electrical resistance of the current-conducting components (e.g. conductive parts in the electrodes, current collectors and cell terminals). The ohmic drop is followed by a drop caused by charge transfer and double-layer effects. In the longer term the diffusion also plays a major role. The impedance $Z(t) = OCV - V(t)/I$ increases with ongoing load. When the current goes to zero again, the cell shows a similar behaviour as a relaxation state is approached. After a rest time, a new OCV corresponding to the new SOC is reached. Thus, such current pulse methods alter the SOC of the cell. Often the pulses are followed by a rest phase and then a pulse with the same amplitude but different sign is applied. Then the next higher current value is set and the procedure is repeated [50, 52, 53].

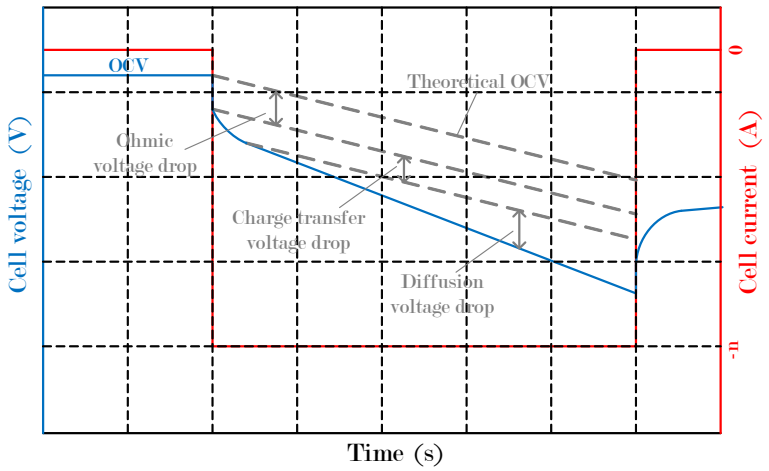

Figure 2.9 Voltage response to current step of LIB (own representation based on [8]).

Fig. 2.10 shows the impedance of a LIB in a Nyquist plot. The impedance is measured by EIS where the cell is excited with a sinusoidal current or voltage and the corresponding response is measured. Usually the impedance is measured for different frequencies and calculated by $Z(j\omega) = V(j\omega)/I(j\omega)$ with j being the complex number and ω the angular frequency in Hz. As shown in the graph, the region of interest for LIB is in the negative imaginary part, as diffusion and charge transfer are capacitive phenomena. The frequency increases towards the origin of the real axis. For low frequencies (ω < 1 Hz) diffusion processes are visible, for middle frequencies (1 Hz < ω < 700 Hz - 1 kHz) double-layer and charge-transfer effects can be observed, while the pure ohmic part is at the intersection of the curve with the real axis (ω = 700 Hz - 1 kHz). For higher frequencies (ω > 700 Hz - 1 kHz) the inductive behaviour of the cell determines the response. Changes in the slope indicate phenomena such as increasing charge-transfer resistance due to changes in SOC or SOH [8, 50]. EIS

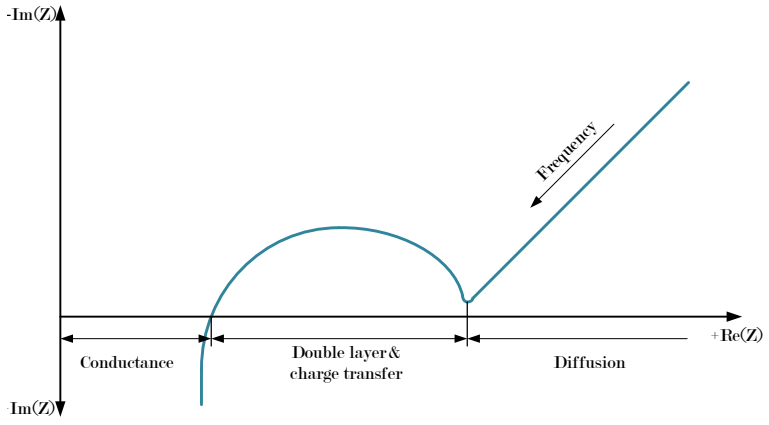

Figure 2.10 Impedance of LIB in Nyquist plot measured by EIS (own representation based on [49]).

is performed with sinusoidal signals, so after one period the SOC is again at its initial value.

Chapter 3

Non-Destructive Testing

NDT is widely used in multiple engineering and science fields, and also in medicine (a field where the non-destructive aspect is appreciated by all of us). Methods that are considered NTD must not alter the structure of the DUT permanently. Therefore, these methods are also suited for quality control, regular inspection and delicate DUT [54, 55]. The fields of application are very diverse. It can be acoustic inspection of bridges, radiographic examination of old paintings or the magnetic resonance imaging of a brain. While NDT covers more test methods and sub-groups of methods, classical NDT is divided in six main methods which are,

1. visual,
2. radiographic,
3. acoustic,
4. magnetic particle,
5. electrical (eddy current), and
6. liquid penetration.

These methods can be divided further into many techniques which may be very specific to some applications [54, 55].

NDT methods are suited to generate information throughout the whole product life of a DUT from its design / development phase until its replacement / disposal [55]. There is i) information on the structural properties of the DUT such as strength, stiffness, dimensions, and characterization of micro and macro features of materials, isotropy and residual stresses; ii) information on material quality of the DUT such as homogeneity, presence of defects and their location, size and volume related information; iii) information on and process quality for the DUT such as dispersion of defects over samples and soundness of manufacturing processes; iv) information on service of the DUT such as extent of deterioration due to environmental effects and wearing through use, for example changes

related to information in material homogeneity and dimension, corrosion, erosion, damage due to fatigue, creep and impact damage due to lightning; and v) information on maintenance of the DUT such as adequacy of repair and replacement of materials and structures [55].

Four of the methods listed above were applied to LIB in various forms [10]. Liquid penetration and magnetic particle inspection were not applied. The liquid penetration method is designed for inspection of non-porous surfaces for damages such as cracks [54–56]. This is usually irrelevant for full cell LIB investigation. As LIB components such as separators and electrodes are highly porous, there is also no use for liquid penetration methods during research and development or post mortem analysis of components.

The magnetic particle method is mainly for ferromagnetic materials. Such materials can be magnetized with an external magnetic field induced by permanent or electrical magnets. Small ferromagnetic particles are then given on the surface. Areas with defects, inclusions or other inhomogeneities show different particle density per surface area as the magnetization is different compared to the pure material of the DUT. After the inspection demagnetization and cleaning of the DUT is required [54, 55]. Also here no publications concerning LIB were found. Even with LIB containing ferromagnetic materials, the changes in structure are most likely to small to be visualized by commonly used magnetic particles.

Visual inspection mostly refers to the analysis of certain properties of a DUT by human eye, but it can also be performed by e.g. a camera with special software for post-processing the image. As the method is dependent on an external source of light and its interaction with the DUT surface, it is a method to determine external properties of the DUT. These properties can be of different nature, such as surface structure, or colour, or form and dimension of the DUT [57]. Visual inspection is also applied to LIB in various forms. Critical states of e.g. LIB pouch cells can be seen by bloating of the cell [58, 59]. Post mortem studies are often supported by visual inspection e.g. to identify areas with lithium plating on electrodes [60, 61]. These areas then can be examined using other specialized visual inspection modes such as inspection of the regions by microscope or applying other test methods. Further the dimension can be monitored by different optical techniques for quality control or also during operation to identify a change in thickness of the cell with changing SOC [10, 62, 61].

Radiographic methods have been widely applied for LIB since decades. In classical NDT they are based on X- or gamma- rays [54, 55], while for LIB also neutron imaging is applied. By measuring the attenuation of the ray through the DUT, information about internal properties can be obtained. They are also referred to as imaging methods [10, 54, 55]. Since imaging methods are not in the focus of this thesis, the reader is referred to existing literature [63, 64] for further information.

Electrical or eddy current methods measure the deviation of electrical conductivity and magnetic permeability of electrically conducting DUTs by induction of eddy currents. They are mainly used for inspection of surfaces and tubes. Defects, inclusions, or other inhomogeneities lead to a change in phase of amplitude from the received signal and thus can be detected [54, 55]. For LIB, so far they have been applied to monitor changes in thickness of the cell by eddy current based dilatometry [10, 65, 66]. For investigation on material properties themselves no publications were found.

As this work mainly focuses on acoustic methods for LIB investigation and these methods became increasingly popular for inspection and monitoring of LIB in the last years [10], the acoustic based methods are described in more detail in the following sections.

3.1 Experimental Modal Analysis

This section is complementary to the theory of EMA given in paper 1 [19] and paper 3 [10]. The reader is also referred to those sections e.g. for the practical mechanical setup of such measurements.

The EMA or modal analysis in general is the study of the dynamic character of a system that is defined by its frequencies, damping and mode shapes. Modes are resonances of a DUT and are determined by its material properties (mass, stiffness, and damping), and its boundary conditions. If either the material properties or the boundary conditions change, the mode will change [67, 68]. This makes EMA not only a suitable tool for initial investigation but also for monitoring changes of a DUT. Thus, it became a NDT method of choice in the fields of mechanical engineering, civil engineering, and structural dynamics, among others [19].

EMA measurement needs an excitation signal at a certain point of the DUT and at least one point on the DUT where the response is measured. There are several forms of mechanical excitation namely [67]:

- impact
- transient,
- true-, pseudo-, burst- random,
- fast sine sweep (chirp), and
- burst chirp.

The first one is usually done with an impact hammer or other equipment like a falling mass, the latter ones are executed with a dynamic shaker. There is also the possibility to measure the response to excitations occurring during normal operation of a system. As impact testing and fast sine sweep (chirp) are relevant for LIB they are explained in more detail below. The other excitations are briefly explained here for better understanding. Transient signals provide a leakage free measurement and are comparable to impact testing but using a shaker the controllability and the repeatability is increased. True random signals are synthesized with a random number generator. They are always non-periodic in the sampling window, so windowing e.g. with Hanning window of the time signal is obligatory for transformation. True random signals excite the non-linearities in the structure differently and thus can be removed by spectrum averaging. Pseudo-random signals are synthesized in the frequency region to coincide with the measurement window parameters of the equipment. The signal is then transferred to time domain, the measurement taken and transferred back to frequency domain. Since the excitation signal is completely contained in the measurement window, a leakage free measurement is possible.

A disadvantage is that the pseudo random signal excites non-linearities equally, so they will remain (partially) also after spectrum averaging. Burst random excitation consists of either a true- or or time varying pseudo- random signal, which is then followed by a downtime to allow the structural response to decay. Hence, the excitation and the response signal are fully included in the sampling window which allows for a leakage free measurement.

Shaker- based methods are referred to as broad band excitation. The relationship between input and output is usually represented by the frequency response function (FRF). For FRF the excitation signal e.g. a force f(t) and the measurement signal x(t) are transferred in the frequency region using fast Fourier transformation (FFT). The FRF of a system (H(ω)) is then calculated as the ratio of its output response (X(ω)) to the input force (F(ω)) in eq. 3.1 [67, 68].

$$H(\omega) = \frac{X(\omega)}{F(\omega)} \tag{3.1}$$

X(ω) corresponds e.g. to a displacement, acceleration or speed in frequency domain. As already stated, modes are resonances of a DUT. In the FRF these resonances are represented by a peak amplitude in the spectra. Normally there is a multitude of peaks distributed over the spectra though. The modes differ over the structure of the DUT. An excitation or measurement on a different point will lead to a different output. In fig. 3.1 a plate is shown with six different points for input and output, which gives 36 possible transfer relations ($h_{out,in}$). Fig. 3.1 on the left shows the case of an excitation at point 1 and measurement at point 6 ($h_{6,1}$). Fig. 3.1 on the right shows the FRF of each point (n=1,2,...,6) to the excitation at point 1 ($h_{n,1}$), whereas each has its own response. From the shape of each FRF it can be derived that the plate shows a first bending mode. All structures can have up to six rigid body modes, three translational- and three rotational- modes [67, 68]. So to characterize a DUT over its dimension, several distributed points of excitation or measurement are required. For reasons of practicability, impact tests normally are performed for multiple inputs and single outputs and shaker tests for a single input with multiple outputs. When the point of excitation and measurement are the same, it is called a driving point measurement, when they differ it is called a transfer measurement [67, 68]. LIBs often are represented by a 2nd order mechanical mass-spring-damper system. For such systems stiffness of the tested object can be calculated according eq. 3.2 [10, 19, 69].

$$k = \omega^2 m, \tag{3.2}$$

where k is the stiffness and m is the mass. The damping ξ of the test object is given by eq. 3.3 [10, 19, 69], with

$$\xi = \frac{1}{2Q}, \tag{3.3}$$

where Q is defined as the Quality-Factor in eq. 3.4 [10, 19, 69],

$$Q = \frac{\omega}{\Delta\omega}. \tag{3.4}$$

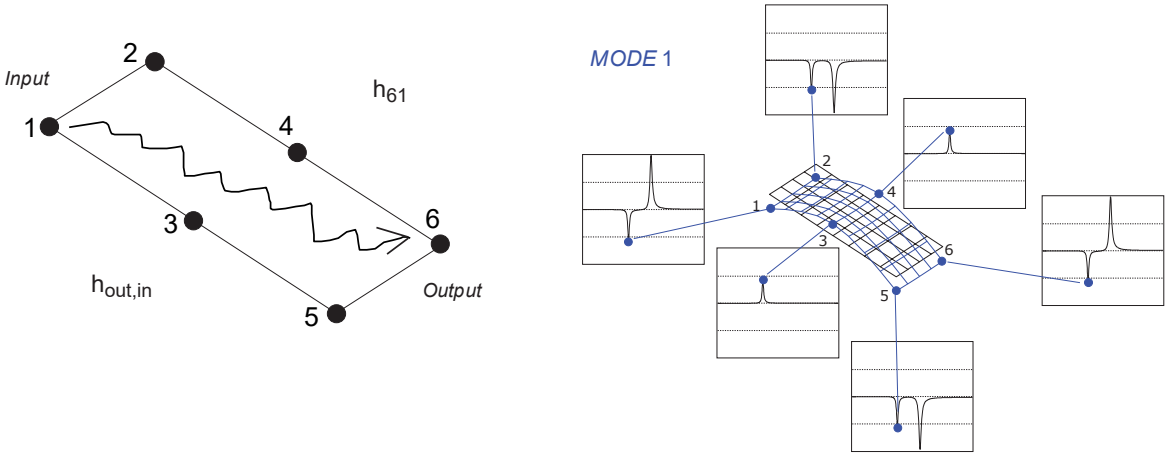

Figure 3.1 Points of excitation and measurement on a plate and FRF mode shapes for mode 1 of the plate (modified from [68]).

with $\Delta\omega$ as the width between the frequencies at half the maximum amplitude of its peak value (full width at half maximum).

For LIB, so far mainly impact testing with a hammer has been carried out, but also shaker testing using sine sweep, and in two cases pseudo random excitation using a shaker was applied. Both driving point and transfer measurements were conducted. Until today mostly pouch cells have been tested, in some cases also prismatic cells, and in one case on cylindrical cells [10].

As already stated, impact testing mostly is performed with a hammer using multiple inputs and a single output. Fig. 3.2 shows a typical excitation pulse with an impact hammer in time domain. The output is a voltage (V) which is generated by an internal force sensor and has to be translated to a force by post-processing (see also power input spectrum below and in fig. 3.3). The excitation with an

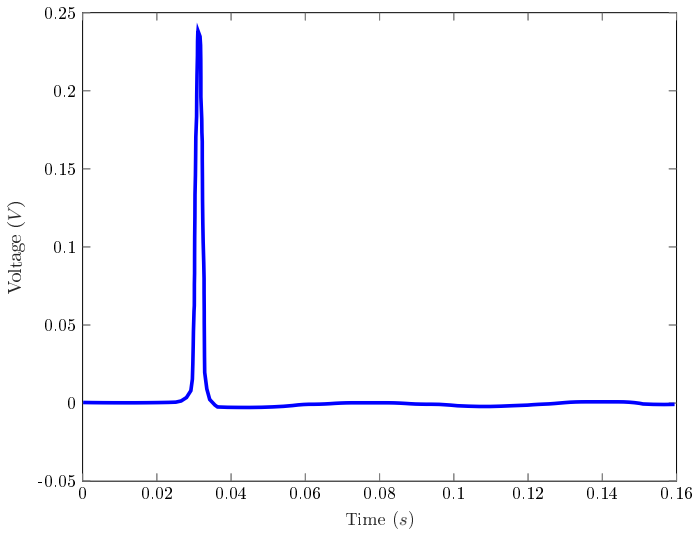

Figure 3.2 Pulse excitation with an impact hammer in time domain (own representation based on [70]).

impact hammer can show significant variation though. Therefore, also the real excitation signal has to be measured, recorded and used for calculation of the FRF. The excitation signal depends on the tip of the hammer (shape and hardness), the angle, the exact point of impact and the properties of the DUT. In fig. 3.3 the power input spectrum of an impact hammer with different tips on a reference mass is shown. The tips vary from hard to soft. Hard tips generate a broader spectrum with a homogeneous amplitude over a wide range, while softer tips have higher amplitudes for lower frequency regions with a declining trend towards higher frequency regions [70]. This behaviour can be transferred to the surface of the DUT, meaning the soft surface of a pouch cell will lead to different pulse excitation than the more stiff aluminium casing of a prismatic cell.

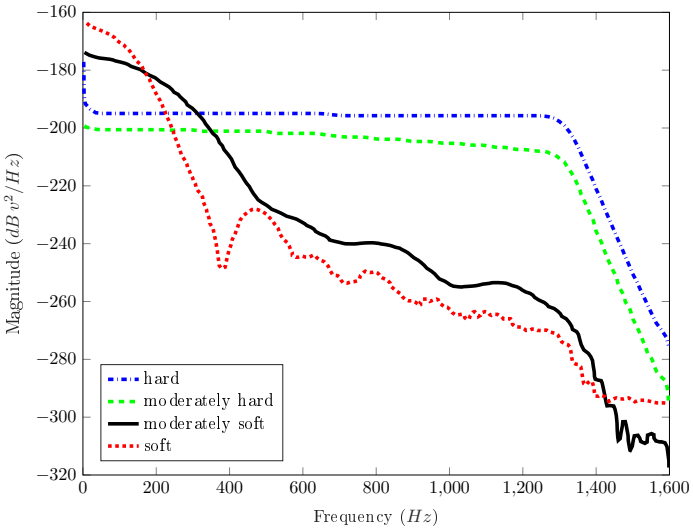

Figure 3.3 Power input spectrum of an impact hammer with different tip hardness on a reference mass (own representation based on [70]).

A sine sweep signal, similar to the pseudo random signal, can also be synthesized in frequency region space to fit the parameters of the equipment. Burst sine sweeps signals, similar to the burst random signal, contain a downtime for the response signal to decay. A disadvantage of sine excitation is, similar to the pseudo random excitation, that it excites non-linearities equally, so they will remain (partially) also after spectrum averaging [67, 71]. In fig. 3.4 the calculated power spectrum of a linear sine sweep (chirp) is shown. The sweep starts from 20 Hz and goes up to 3000 Hz. It can be seen that the spectrum is very homogeneous for the region of interest. In reality there will be transient effects at the beginning and ending of the range due to inertia of the system. This will blur the edges of the spectra, but for the working region the shakers do provide almost a constant amplitude.

Not all types of excitations are equally suited. If e.g. a soft tip is used for impact testing, the power spectrum for higher frequency regions can be too low to excite the modes properly. An indication for this is the coherence function that is used as a data quality assessment tool. It determines how much of the output signal is related to the measured input signal. As such it can also serve as an indicator for influences of noise on the signal. In fig. 3.5 the relationship between input (x(t),X(ω)),

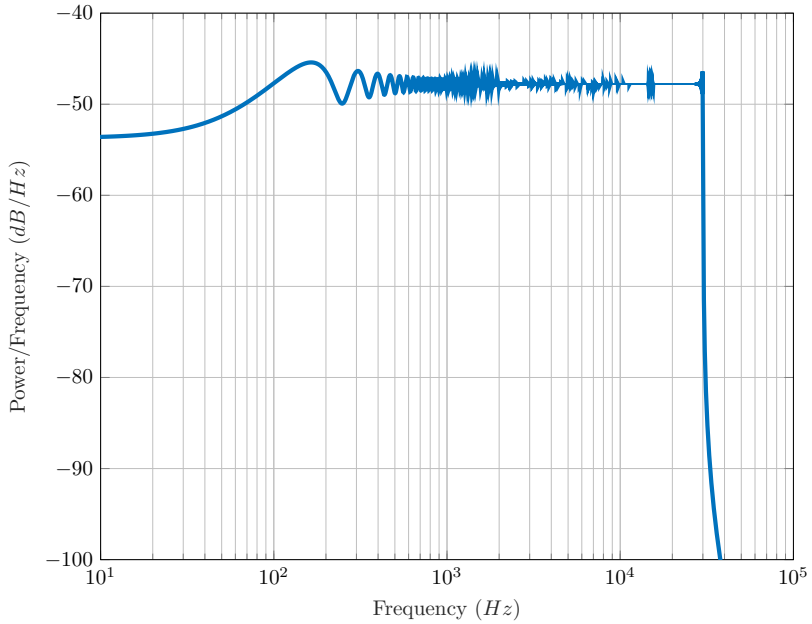

Figure 3.4 Power input spectrum of an ideal excitation (simulated) with a linear sine sweep.

the system investigated (h(t),H(ω)) and the according output (y(t),Y(ω)) is depicted for the time- and frequency- domain. While in the time domain y(t) is a convoluted signal of the input and the system, in frequency domain Y(ω) is a multiplication of those two values (eq. 3.5) [72]. As anticipated in

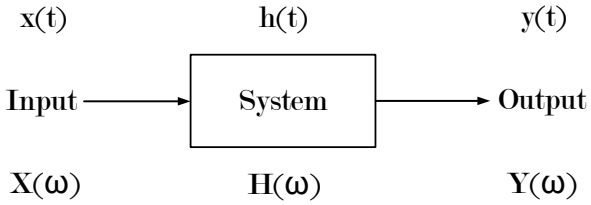

Figure 3.5 Input-output model of a system (own representation based on [68]).

eq. 3.1 the frequency domains are related to the FRF by [68]:

$$Y(\omega) = H(\omega)X(\omega). \tag{3.5}$$

Most analysers and post-processing tools use an averaged power spectrum [68, 72]. This correlates to the linear spectra as shown in tab. 3.1. The asterisk ($*$) indicates the complex conjugate of the signal.

Table 3.1 Relationship of averaged power spectra to linear spectra [68].

Input power spectrum	$G_{xx}(\omega)$	=	$X(\omega)X^*(\omega)$
Output power spectrum	$G_{yy}(\omega)$	=	$Y(\omega)Y^*(\omega)$
Cross power spectrum	$G_{yx}(\omega)$	=	$Y(\omega)X^*(\omega)$
Cross power spectrum	$G_{xy}(\omega)$	=	$X(\omega)Y^*(\omega)$

Multiplication of the input-output relationship (eq. 3.5) with the cross-power-spectrum (tab. 3.1) X^* for one case and Y^* for the other case results delivers eq. 3.6 and eq. 3.7 [68].

$$Y(\omega)X^*(\omega) = H(\omega)X(\omega)X^*(\omega) \Longrightarrow H_{yx}(\omega) = \frac{G_{yx}(\omega)}{G_{xx}(\omega)} = H_1(\omega) \tag{3.6}$$

and

$$Y(\omega)Y^*(\omega) = H(\omega)X(\omega)Y^*(\omega) \Longrightarrow H_{yy}(\omega) = \frac{G_{yy}(\omega)}{G_{xy}(\omega)} = H_2(\omega). \tag{3.7}$$

H_1 is the estimate of the random noise and distortion summing up on the output, but not on the input of the structure and measurement system. It is given by the relation of the cross power spectrum estimate between the input and the output to the auto power spectrum of the input signal [68, 67]. H_2 is the estimate of the random noise and distortion summing up on the input, but not the output of the structure and measurement system. It is given by the relation of the the auto power spectrum of the output signal to cross power spectrum estimate between the input and the output [68, 67]. With H_1 and H_2 the coherence γ^2 can be calculated as follows:

$$\gamma^2(\omega) = \frac{H_1(\omega)}{H_2(\omega)} = \frac{G_{yx}(\omega)G_{xy}(\omega)}{G_{xx}(\omega)G_{yy}(\omega)} \tag{3.8}$$

The coherence is a real-valued spectrum. It is a dimensionless scalar between 0 and 1. 0 means no coherent relation, so the output has no causal relationship to the input and 1 means full coherent relation, so all of the output signal is related to the input [68].

EMA for LIB is not only conducted on single cells but also on LIB modules. Further information can be found in paper 3 [10].

3.2 Ultrasonics

This section is complementary to the theory of ultrasonic probing given in paper 2 [20] and paper 3 [10]. The reader is also referred to those sections.

US NDT methods analyse the spatial propagation of oscillations in the form of waves in matter. A prerequisite for this is the elastic coupling of molecules / particles. The oscillation is distributed from one particle to another. Thus, wave propagation involves the transport of mechanical energy but not from mass. Particles vibrate (or oscillate in the case of Rayleigh- and Lamb waves, details see below) and return to their initial position when the movement has subsided [73, 55].

3.2.1 Types of Waves

In an unbound elastic medium, two types of waves can be found: The first type are i) longitudinal waves, also called pressure (P-) or compressional waves (fig. 3.6 (top)). The displacement of the medium occurs in the same direction as the propagation of the wave. The latter can travel through both solids and liquids. The waves generate a compression and an expansion of the material they are

travelling through. The second type are ii) transverse waves, also called shear (S-) waves (fig. 3.6 (bottom)). The displacement of the medium is perpendicular to the direction of the wave propagation. The wave can only travel through solids [10, 55, 73]. These two wave types are mainly of interest

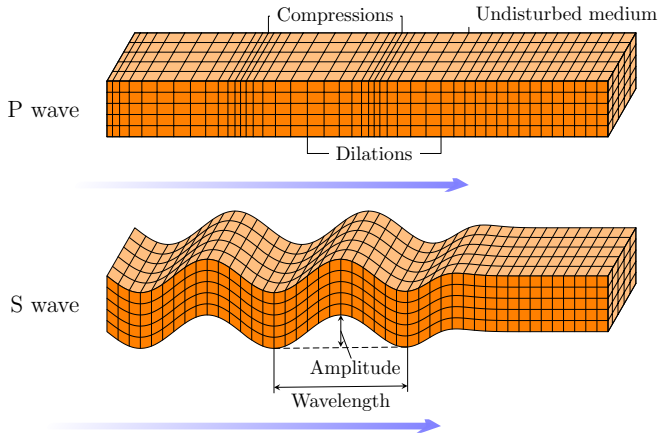

Figure 3.6 P- (top) and S- wave (bottom) propagation (modified from [74], CC BY 4).

for through-body or reflection measurements. When reaching an interface, the waves are partially reflected, and the ongoing wave is attenuated. If the waves reach an interface at an angle, S-waves will arise. The larger the difference in mechanical impedance between the interfaces, the higher the magnitude of the reflection [10, 55, 73].

In addition to these waves, in a medium, under certain circumstances, two other types of waves can be found: iii) Rayleigh waves: starting from a certain angle of the emitter to the surface (intromission angle) the S-waves transform to surface waves, so-called Rayleigh waves. These waves show a penetration depth of the DUT of approximately the wavelength of the signal and the movement of the particles is in an elliptical way. Rayleigh waves can also travel through curved surfaces as long as the radius is higher than the wavelength of the signal [55, 73]; iv) Lamb waves: Are waves that are generated in thin semi-infinite layers like e.g. plates. They are excited best when the thickness of the plate equals or is close to the wavelength of the excitation signal. There are two forms of Lamb-waves, symmetric waves (fig. 3.7, top), also extensional waves, and anti-symmetric waves (fig. 3.7, bottom), also flexural waves. Both sides of the surface show this movement, as Lamb- waves always affect the full thickness of the plate. The particle movement of Lamb- waves is an elliptical motion [55, 73].

For LIB cells mainly P-, S- and Lamb- waves are relevant and further elaborated below in this section. Tab. 3.2 summarizes these wave types and their main properties.

3.2.2 Wave Propagation

The speed of propagation in a medium is dependent on the type of wave itself and on the elastic properties and the density of the medium. These values are represented as the acoustic impedance in

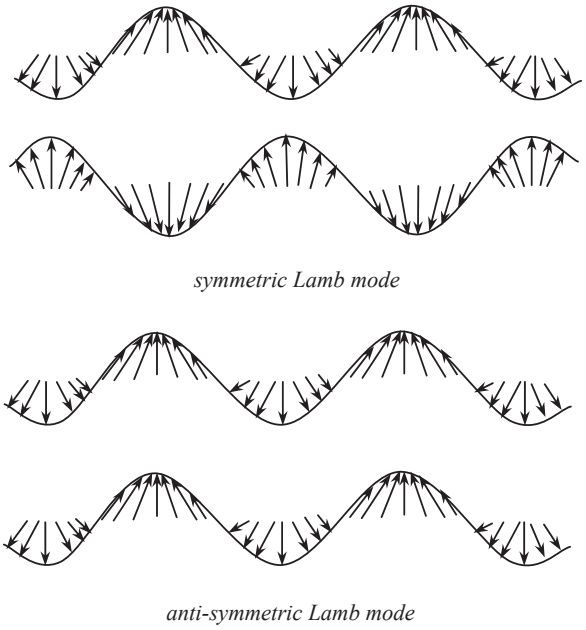

Figure 3.7 Symmetric- (top) and anti-symmetric Lamb wave (bottom) (with permission [75]).

Table 3.2 Classification and properties of wave types [55].

Type	Direction of disturbance	Direction of particle motion
Longitunal waves particle		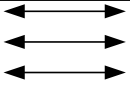
Transverse waves particle		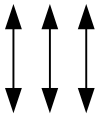
Compressional and flexural waves (Rayleigh- and Lamb- waves)	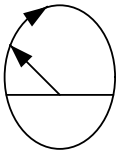	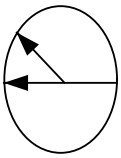

eq. 3.9 [10, 73].

$$Z = \rho \cdot c \tag{3.9}$$

Here ρ is the material density in kg/m^3 of the DUT and c is the speed of propagation in m/s and Z the acoustic impedance in kg/(m^{2}s) [73]. The higher the density, the faster the propagation of the wave. For an unbound medium the wavelengths can be calculated as follows [55, 73]:

$$\lambda = \frac{c}{f}. \tag{3.10}$$

With f being the frequency in Hz and λ in m. The propagation velocity of the wave is given by

$$c = \sqrt{\frac{K + \frac{4}{3}G}{\rho}}. \tag{3.11}$$

With K being the bulk- and G the shear-modulus given in (3.12) and (3.13).

$$K = \frac{E}{3(1-2v)} \tag{3.12}$$

$$G = \frac{E}{2(1+v)} \tag{3.13}$$

Where E is the elastic modulus in Pa and v is the dimensionless Poisson's ratio. For Rayleigh- and Lamb- waves the speed of propagation is different. Rayleigh waves travel with 0.9 times the speed of S-waves in the same medium [73]. For Lamb-waves additional parameters are involved, because their propagation characteristics vary with entry angle, excitation and structural geometry [75]. Lamb modes can be defined as

$$\frac{tan(qd)}{tan(pd)} = \left[\frac{-4k^2pq}{(q^2-k^2)^2}\right]^{\pm 1} \tag{3.14}$$

with the power over the full term being +1 for symmetric modes and -1 for asymmetric modes [55, 75]. Given parameters are the plate thickness d in m, phase velocity c_p in m/s and the wave circular frequency ω in Hz. The other parameters are calculated as follows. The factors q and p are given in eq. 3.15 and eq. 3.16 respectively.

$$q^2 = \frac{\omega^2}{c_t^2 - k^2} \tag{3.15}$$

$$p^2 = \frac{\omega^2}{c_l^2 - k^2} \tag{3.16}$$

The wave-number k is calculated in eq. 3.17.

$$k = \frac{\omega}{c_p} \tag{3.17}$$

The velocities of the transversal- and the longitudinal- waves c_t and c_l in m/s are given in eq. 3.18 and eq. 3.19 respectively.

$$c_t^2 = \sqrt{\frac{\mu}{\rho}} \tag{3.18}$$

$$c_l^2 = \sqrt{\frac{\lambda + 2\mu}{\rho}} \tag{3.19}$$

Here λ and μ are Lamé constants (two material-dependent quantities defining strain-stress relationships) given in eq. 3.20 and eq. 3.21 respectively.

$$\lambda = \frac{v}{1-2v} \cdot \frac{1}{1+v} \cdot E \tag{3.20}$$

$$\mu = \frac{1}{2} \cdot \frac{1}{1+v} \cdot E \tag{3.21}$$

As the speed of propagation is dependent on the angular frequency (eq. 3.17) Lamb waves show a dispersive character. In fig. 3.8 the first two symmetric and asymmetric calculated modes of an aluminium plate are shown. In theory there are an infinite number of curves in reality there are two families of symmetric and asymmetric modes [55, 75]. When waves strike an interface between two

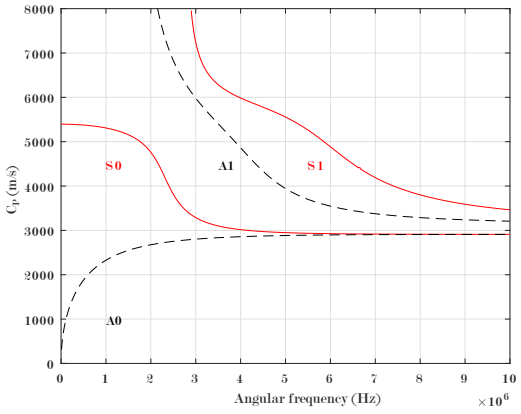

Figure 3.8 Dispersion curve of aluminium plate (modified, courtesy by S. Keller).

media at a certain angle the wave can be reflected, diffracted, transmitted, scattered or converted in its mode. Most of the time a combination of all these options takes place. Part of the energy of the wave gets adsorbed [55, 73]. US energy loss due to scattering and absorption is referred to as attenuation. The higher the difference in acoustic impedance of the media the higher the part of the reflection at their interface. LIB consist of a multitude of layers made of different materials (see also fig. 2.2) with varying acoustic impedance. The above-stated phenomena manifest on each interface. In fig. 3.9 a three-layered plate (similar to the laminated structure of LIB) with an assumption of wave propagation between plates and interfaces is shown. On each interface there are eight waves, each P-

and S- wave striking (P^+,S^+) and leaving (P^-,S^-) each interface. The total behaviour of the system is then a superposition of those parts [76].

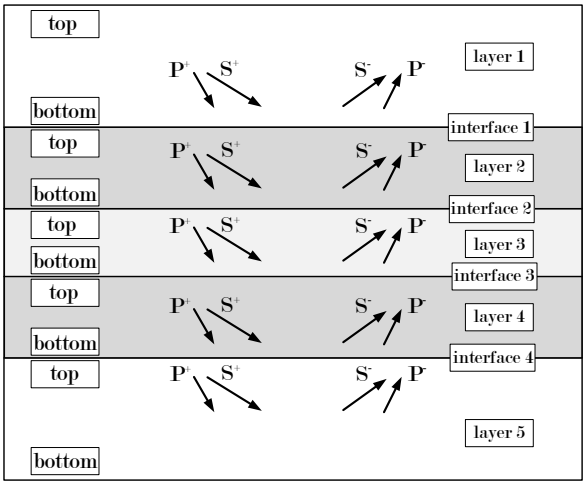

Figure 3.9 Waves in a multilayer plate (modified from [76]).

3.2.3 Ultrasonic Measurements on LIB

Waves in structures need to be excited and measured to calculate the response of the system. In fig. 3.10 a LIB pouch cell with possible combinations of piezo disc transducers as emitters and receivers for measurement are shown and the paths for wave propagation are indicated. For through body reflection measurement, any of the actuators (1 to 3) sends a wave and is then put into receiving mode as a sensor measuring the reflection of the signal from the opposite side and from the interfaces in between the layers. In the through-body measurement, emitter 1 sends a signal which then is received by sensor 3. Surface waves (Lamb waves in case of LIB) are measured when emitter 1 sends a signal which then is received by sensor 2 [10]. Excitation with measurement of US waves

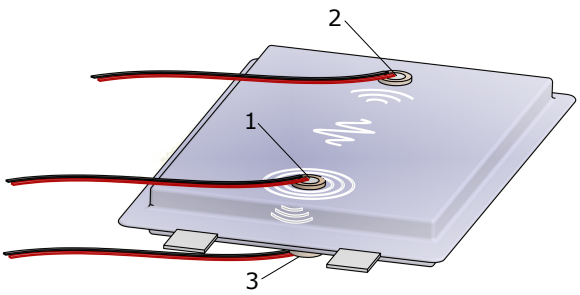

Figure 3.10 Pouch cell with attached piezo disc transducers and paths of measurements [10] (CC BY 4).

with piezo discs is an often-chosen concept as the latter have a comparably high-frequency response, low driving force, and are cheap. It is also beneficial that one type of sensor can serve as both

emitter and receiver [75]. Other possibilities, which have not been applied to LIB so far [10], and in some cases only can act as emitter or receiver, are ultrasonic probes, laser, interdigital transducers, electromagnetic transducers, and optical fibres [75]. As this thesis focuses on piezo transducers, those are explained in more detail.

Piezo transducer work based on the principle of the piezo-electric effect. The effect describes the behaviour of some crystals, such as quartz and tourmaline, to produce an electric charge on their surface when they are subjected to compressional- or tensile mechanical forces. There is also the inverse piezo-electric effect, where the crystal expands or contracts when subjected to an electric charge [55, 73]. In the case of piezo transducer measurement, the emitter is operated with the inverse piezo-electric effect, so mechanical energy is created by electrical excitation, while the receiver is operated with the piezo-electric effect, so mechanical energy is converted to electrical one.

The resonance frequency of piezo-electric transducers is given by [73]:

$$f_0 = \frac{c}{2d}, \tag{3.22}$$

with c being the propagation velocity of sound in m/s in the transducer material and d being the thickness of the transducer in mm. This means that the thinner a transducer, the higher its resonance frequency. Piezo-electric transducers work most efficiently when they are operated at their resonance point, even when in theory they should work at all frequencies they are subjected to. In reality the attenuation is too high when they are operated too far from their resonance point [55, 73]. In fig. 3.11 the resulting mechanical amplitude over the excitation frequency is shown for an excitation with constant electrical amplitude. At f_0 the resulting amplitude is the highest. The electro-mechanical coefficient, which is the ratio between mechanical output energy to electrical input energy, is determined at this point [55]. Thus, the resonance frequency is a parameter that is important to know as at this point an efficient measurement with high amplitudes is possible. The mechanical quality factor of the piezo transducer is given by [55]:

$$Q = \frac{f_0}{f_2 - f_1} = \frac{f_0}{\Delta f}, \tag{3.23}$$

with f_1 and f_2 being the frequency where the sonic amplitude is 70 % of that at f_0 (fig. 3.11). A wide-band transducer has sharp and well-defined pressure changes within the near zone, resulting in sufficient sensitivity to small mechanical amplitudes and resolution to small changes in frequency [55].

When the piezo transducer is fixed to the device under test or encapsulated in any way, the thickness of the active part does not change, so resonance frequency stays the same. Due to the increased mass, the shape usually is flattened. There can be further resonances of the sensor-device structure; these are then indicated as additional peaks.

For excitation often a single (rectangular) pulse signal is sent followed by enough dead time to allow the corresponding system response to be received and unwanted reflections and echoes to decay. Then the signal and measurement can be repeated and e.g. the results averaged to reduce the

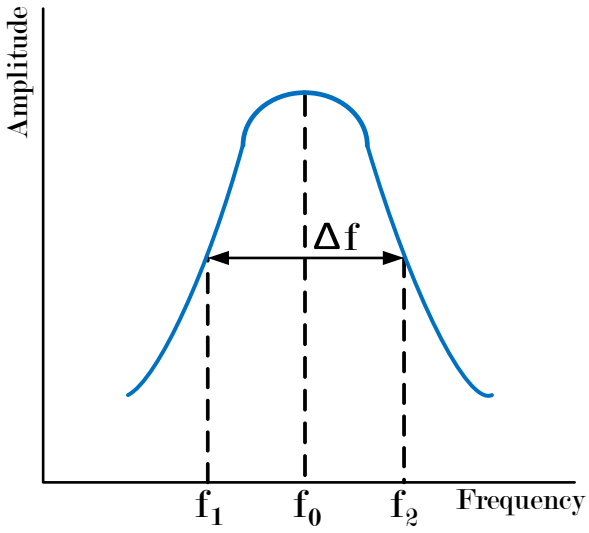

Figure 3.11 Quality factor of piezo-electric transducers (own representation based on [55]).

influence of noise. This is a very common method [55, 73], however, for LIB it is seldom used (during this thesis in paper 2 [20]). More commonly, the piezo-elements are driven by a sine signal that is windowed by another lower frequency function such as a triangle or sine signal, or a special window function [10]. Pulse signals have the benefit that the electronics for excitation are reduced significantly in complexity. Instead of sine signal generation e.g. through pulse width modulation with filters or oscillator circuits, both with downstream output stage (operational) amplifiers, for a rectangular pulse a semi-conductor switch is sufficient [20]. A possible drawback of the rectangular pulse excitation is that such a signal not only consists of its base frequency but also shows harmonics at a sequence of odd- number multiples of the base frequency. This is shown in fig. 3.12 for a simulated pulse with 25 µs. The power of the spectrum declines with increasing frequency even for such ideal signals. When the piezo transducer is driven outside of this resonance frequency the influences in reality are even lower.

The propagation of the sound wave through the DUT leads to an attenuation of the signal amplitude and needs a certain time to travel from the emitter to the receiver. This time delay is called time of flight (TOF). Measurement of the TOF is the most popular for LIB [10] (and also in general [55, 73]. Equal to the behaviour in the audible region (sec. 4.1) the output signal is the input cross-correlated with the system behaviour (eq. 3.24).

$$[f * g](\tau) = \int_{-\infty}^{\infty} f(t)g(t+\tau)dt \tag{3.24}$$

Where f is the emitted signal, g is the received signal, t is the time and τ is the delay of the signal. For simpler processing of the data (similar to audible region in sec. 4.1) the time-based signal is transferred into the frequency domain. Most commonly this is done using cross-correlation [10],

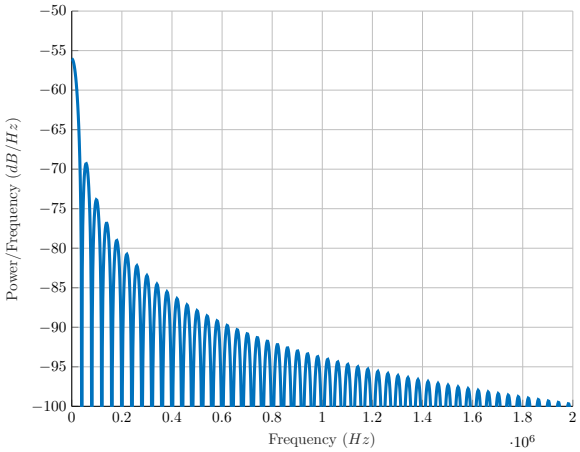

Figure 3.12 Spectrum of a single rectangle pulse with pulse width of 25 µs.

which is the inverse Fourier transformation of the cross-power spectrum G_{xy} given in eq. 3.25 [77]:

$$R_{xy}(\tau) = \int_{-\infty}^{\infty} G_{xy}(\omega) e^{i2\pi f \tau} df. \tag{3.25}$$

A second method for analysing the US signal is the measurement of the total transferred energy given as [10]

$$A = \int_{t_i}^{t_f} |f(t)| dt. \tag{3.26}$$

In summary, US analysis with piezo transducers can be achieved at comparably low cost and thus has been used more and more over the last year. Still there are many constraints to be considered and the setup should be optimized for the transducer - DUT combination.

Chapter 4

Results and Discussion

In this cumulative thesis the detailed findings, results and corresponding discussions can be found in the papers in the annexes B, C and D. The following sections provide an outline of the corresponding results and discussion section rather than a full replication. The supplementary information and results presented in the appendix are discussed in the respective appendix chapters and are not elaborated further.

4.1 Mechanical FRF of LIB

In this paper [78] (see appendix B) mechanical FRF was used to reveal changes in SOC and SOH of LIB. An electro-dynamic shaker and an impedance head were placed upside down on pouch cells to perform a driving point measurement. A sinusoidal sweep was performed from 20 Hz to 3 kHz (operational boundaries of the shaker). To decouple the cell mechanically from the test environment and for an unrestrained driving point measurement, a special test bench was designed with foam paddings for the cell and strain relieves for the wiring of the shaker and impedance head unit. The functionality was evaluated and the limiting frequencies were determined to ensure measurements with minimum distortion. In [62] and during a co-supervised master thesis [79] the test bed was additionally equipped with contact-less 1-D dilation measurement to allow for comparison of the shape of FRF with the dilation of the cell. The cell was operated in a climatic chamber to ensure constant environmental conditions and to test the method at several temperatures. As continuous measurement with this method generated too much data for the test bench, the SOC of the cell was altered by an electrical test bench to levels of 0, 25, 50, 75, and 100 % and the measurements were performed at these points all for a temperature of 5, 25 and 45°C. An off-the-shelf cell with SOH level of 100 % and an aged one with SOH of 75 %, both same type and batch, were tested.

It was observed that the stiffness of the cell increases with the SOC. These finding are supported by literature values and calculations. This is also true for the aged cell, but the effects are less pronounced. In general the aged cell appears to be softer than the new one, but the observed changes lie within the inaccuracies when a new measurement setup is established. Changes in temperature have the

highest influence on the FRF shape and modal frequencies. With increasing temperature, the cell softens and the effect is dominant over the other influencing factors. In conclusion, it was found that the FRF's method is only of limited use in increasing the accuracy of BMS. However, it can provide useful values about the mechanical properties of the cell for the design of battery systems.

4.2 SOC Estimation of LIB by US based TOF Measurement

In this paper [20] (see appendix C) US sensing was applied to pouch cells for SOC estimation. The focus was to reduce the complexity of the methods evaluated successfully in [16–18] with laboratory equipment, so that it can be implemented for BMS systems. The approach was to lower the excitation frequency and use a single semi-conductor switch instead of a complex windowed sine wave package. For measurement of the response, TOF was chosen as the value of interest, and for the determination of the changes in TOF, a tracing algorithm for significant peaks in the received signal was developed. Using standard piezo actuator disks as emitter and receiver, a low-cost BMS add-on was developed and further evaluated for real-world operating conditions using a SOC estimator with C-rate and temperature compensation based on TOF.

The developed simplified TOF measurement approach worked continuously over the full SOC of the cell and also for the full temperature range of 5 to 45°C. The TOF was found to be dependent on the SOC and on the cell temperature. TOF becomes shorter with falling temperature and increasing SOC, indicating that the cell becomes stiffer. The cell temperature was the variable with the greatest effect on the TOF. Depending on the C-rate there is a hysteresis in the TOF. The SOC estimator based on TOF produced a maximum error of 2.06 µs which is an error of 1.29 % of the measured value or 16.85 % of the total change in TOF, which corresponds to the SOC in the test case of a downscaled real-world driving cycle power profile. With a memory function the error could be reduced significantly.

4.3 Review of NDT on LIB

In this paper [10] (see appendix D) an extensive literature review on NDT methods for LIB is performed. The manuscript is focused on methods with the potential for integration in applications, so imaging methods are not included. The review aims to present the current state of this promising topic for both laboratory use and applications on non-destructive in-situ and in-operando methods for measurement of mechanical battery parameters like expansion, strain and force, EMA, US probing and acoustic emission (AE) technologies in order to provide insights in this emerging topic by showing and comparing benefits, drawbacks, possibilities and applications of each technique. The introduction of the paper additionally covers the internal processes in the cell that are the source of the subsequent changes in mechanical properties.

In this work 177 references were analysed. It was found that measurement of dilation is widely used to reveal electro-chemical phenomena like Li^+ staging in graphite, plating and SEI formation in

laboratory application. This is also true for force and strain measurements, but abusive conditions are also covered and the trend additionally is on implementation in battery systems or BMS respectively, covering practical SOC and SOH estimation approaches. EMA and FRF are suited to derive mechanical parameters for construction of battery systems. Current literature is inconclusive about the impacts of SOC and SOH on the EMA and FRF and in general does not point to a future use in laboratory to reveal internal phenomena nor for estimation of SOX within an application. US probing is an emerging topic, mainly used for SOX determination and for detecting abusive conditions. The AE approach mainly is employed for analysis of forming processes during the first cycles and also for monitoring material decay due to cracking or gassing. It could be used to monitor SOH and abusive conditions. It was concluded that strain / force and US sensing have the most promising prospects for implementation within battery systems.

Chapter 5

Scientific Contribution, Conclusion and Outlook

This chapter lists the scientific contributions of the work performed during this thesis and provides an overall conclusion and an outlook.

5.1 Scientific Contribution Achieved With this Thesis

This thesis is mainly focuses on acoustic testing of LIB for SOX measurement. The journal articles, but also the other contributions like presentations and supervised master thesis, significant progress was made to further advance the topic of NDT testing of LIB. Below a list stating the most relevant contributions to the best of the author's knowledge is given:

- First journal publication for FRF on LIB with automated test setup and sweep excitation in paper 1 [19].
- First publication on the dependency of LIB's FRF on cell temperature in paper 1 [19].
- First comparison of FRF for new and aged cells in paper 1 [19].
- First comparison of cell dilation, differential voltage and FRF over SOC in a conference contribution [78] and in co-supervised masters thesis [79] (see appendix E).
- Novel low-cost concept for measuring TOF suited for BMS implementation with automated pulse generation and tracking in paper 2 [20].
- First continuous measurement for TOF dependency on temperature for LIB cells in paper 2 [20].
- First evaluation of TOF measurement SOC estimators with real world driving cycle and temperature compensation in paper 2 [20].

- First review article on NDT (without imaging methods) of LIB in paper 3 [10].
- First evaluation of NDT methods for application in laboratory and in real world settings in paper 3 [10].

In addition to these points and the published research, two collaborative research projects were organized, written, granted and executed or started in the course of this thesis; these projects are VALERIE (FFG Grant 865148) and MOGLI (FFG Grant 879610). Especially, the second project will lead to further significant advances in this field, as it hosts at least 3 PhD students and brings together research and industry.

5.2 Conclusion

The main goal of this thesis was to explore the acoustic-based methods for LIB inspection (sec. 1.2), as they are promising and yet neither investigated in detail nor fully understood. Thus, in sec. 4.1 FRF was chosen and explored as a method using audible sound. A correlation between the shifts in the modes of the FRF spectra and both the SOC and the SOH was measured. It was found that the cell becomes stiffer with increasing SOC and softer with decreasing SOH. The increase in stiffness is almost monotonic until a SOC of 75 % while a decline was found for higher SOC levels; for SOH the stiffness decreases monotonically for decreasing SOH with a lower gradient at lower SOH. For the SOC values this is in agreement with most of the former studies, whereas for SOH the literature is inconclusive (for details see EMA section in paper 3 [10]). The strongest dependency of the FRF was found to be on cell temperature with the effects superimposed on SOC and SOH influences. This demands for an exact monitoring of the cell temperature during FRF measurement. A disadvantage of this method is the high level of error that occurs when disassembling and reassembling the test setup. Especially the amplitude in the FRF spectra is impacted with standard deviations of more than 10 % in the region of interest even when defined torques for bolt connections and strain reliefs at defined cable lengths were used. Without changes in the mechanical setup, repeatability was high with errors within the general measurement inaccuracy of the equipment. In total it can be concluded that the FRF is suited to detect SOX and temperature-dependent mechanical properties of LIB which is important for the mechanical design of battery systems [69, 80, 81]. Due to the accuracy and repeatability it is not (yet) suited for SOX determination in general and, due to its size, nor for applications (for details see Implementation section in paper 3 [10]). For excitation, audio amplifiers can be used, but for signal measurement precision, amplifiers with high linearity and gain and advanced signal processing with FFT are required.

In former studies [16–18] US sensing was successfully applied, but like the FRF method it required costly and complex laboratory equipment. To overcome those issues and investigate possibilities for future use in applications, the US approach presented in sec. 4.2 was successfully trimmed for simplicity and applicability. As it uses standard piezo transducer discs for both excitation and measurement, and complexity-reduced electronics, a BMS add-on for US TOF diagnostic was realised

for a total cost of less than 10 € for a single unit, without considering economies of scale. A concept with excitation using a semiconductor switch and post processing of the signal with a Schmitt trigger and a capture input of the micro-controller of the BMS was developed and positively evaluated. This concept allows for tracing the TOF without measuring the full response of the system and without the need for cross-correlation of the signal. Thus it has low demands on the micro-controller compared to previous approaches and could be implemented in state-of-the-art BMS. An estimator with temperature compensation and average C-rate strategy was implemented and validated with a real world driving cycle with an accuracy of 1.29 % of the measured value. Further improvements are needed here (see also sec. 5.3. Similar to the FRF also here a strong influence of the temperature was found. This indicates that it is favourable to precisely monitor cell temperature when acoustic methods are used to monitor LIBs.

During the course of the work, a lack of literature dealing with non-imaging NDT methods for LIB estimation or inspection in general was found. Thus in sec. 4.3 a detailed review on those topics was performed. It was shown that the methods have been increasingly applied in the past decade and are able to contribute to the understanding of internal changes in LIB and also for SOX estimation. Initial publications are mostly on expansion measurement mainly to identify electrochemical phenomena like the formation of the SEI or Li^+ intercalation. Newer publications also facilitate measurements of strain / force and US sensing for application, SOX estimation, abusive conditions and other types of monitoring. Advanced algorithms like machine learning or filters are applied in combination with cell voltage and temperature to monitor LIBs' state in detail. Such algorithms outperform those solely based on electrical parameters by far.

In summary, the goal of investigating the possibilities and boundaries of NDT testing of LIB was achieved and the applicability was shown for several use cases. It can be concluded that NDT including acoustic methods, are able to reveal several phenomena and properties that cannot be revealed by measuring the electrical two-pole behaviour and the temperature of the DUT. An additional benefit is that the methods are in-situ and in-operando and can be realised with low cost. The methods are suitable for research, development and application starting from material level up to system level. As most of the methods still have potential for improvement, the next section gives an outlook on possible further work.

5.3 Outlook

The FRF method presented in paper 1 [62] is suited to reveal mechanical properties like eigenfrequencies of the DUT and their change over SOC and SOH. However, the findings in this work are not in agreement with work published later on e.g. by Berg et al. [71]. In general, the literature is inconclusive on the impacts of SOC and especially SOH on the FRF [10, 71]. A higher number of samples for testing are needed and continuous monitoring of the impacts of ageing on the FRF must be performed to fully understand the processes involved and the impacts on the FRF. Current studies lack this information.

For monitoring the SOC of LIB by measuring the TOF in paper 2 [20] the proof of the concept was done, but the accuracy is not suited yet for application. This could be solved by using a combination of TOF with other values and / or using machine learning to increase SOC and SOH prediction accuracy significantly such as shown in the work of Davies et al. [15]. The method also has to be extended to cells within a module where mechanical constraints are present.

Looking at the review of paper 3 [10] it becomes obvious that the NDT methods mainly are used to investigate state-of-the-art cells. As those methods add valuable insights on the processes within those cells, the methods should be transferred to cell chemistries that are currently under development like cells with anodes with high silicon content or solid-state batteries. In-operando information of forces and expansion of those cells would support the development of such components.

In general the methods also bear the potential for classification of used cells for second-life applications (see [15, 82] for SOH estimation without cycling), for quality inspection after manufacturing (as demonstrated in [83]) and for monitoring cells during storage without cycling. Here only a beginning has been made and future research is required.

Bibliography

[1] International Energy Agency, Data & Statistics.
URL https://www.iea.org/data-and-statistics

[2] European Environment Agency, Primary energy consumption by fuel in Europe.
URL https://www.eea.europa.eu/data-and-maps/indicators/primary-energy-consumption-by-fuel-7/assessment

[3] International Energy Agency, Global CO2 emissions in 2019 Analysis.
URL https://www.iea.org/articles/global-co2-emissions-in-2019

[4] European Environment Agency, Tackling pollution and climate change in Europe will improve health and well-being, especially for the most vulnerable.
URL https://www.eea.europa.eu/highlights/tackling-pollution-and-climate-change

[5] E. Commission, 2030 climate & energy framework (Nov. 2016).
URL https://ec.europa.eu/clima/policies/strategies/2030_en

[6] C. Pillot, Impact of the EV Market Growth on Lithium-ion Batteries and Raw Materials Supply 2019-2030 (2020).
URL https://www.advancedautobat.com/europe

[7] P. Raion, M. Taylor, A. Ilas, H. Diaz-Bone, K.-P. Kairies, Electricity Storage and Renewables: Costs and Markets to 2030, IRENA - International Renewable Energy Agency, Abu Dhabi, 2017.
URL https://www.irena.org

[8] A. Jossen, W. Weydanz, E. Cuvillier, Moderne Akkumulatoren richtig einsetzen, 2019, oCLC: 1090779267.

[9] T. B. Reddy, D. Linden (Eds.), Linden's handbook of batteries, 4th Edition, McGraw-Hill, New York, 2011.

[10] H. Popp, M. Koller, M. Jahn, A. Bergmann, Mechanical methods for state determination of Lithium-Ion secondary batteries: A review, Journal of Energy Storage 32 (2020) 101859.
URL https://linkinghub.elsevier.com/retrieve/pii/S2352152X20316960

[11] S. Bhadra, B. J. Hertzberg, A. G. Hsieh, M. Croft, J. W. Gallaway, B. J. Van Tassell, M. Chamoun, C. Erdonmez, Z. Zhong, T. Sholklapper, D. A. Steingart, The relationship between coefficient of restitution and state of charge of zinc alkaline primary LR6 batteries, Journal of Materials Chemistry A 3 (18) (2015) 9395–9400.
URL http://xlink.rsc.org/?DOI=C5TA01576F

[12] V. A. Sethuraman, L. J. Hardwick, V. Srinivasan, R. Kostecki, Surface structural disordering in graphite upon lithium intercalation/deintercalation, Journal of Power Sources 195 (11) (2010)

3655–3660.
URL https://linkinghub.elsevier.com/retrieve/pii/S0378775309022964

[13] J. H. Lee, H. M. Lee, S. Ahn, Battery dimensional changes occurring during charge/discharge cycles—thin rectangular lithium ion and polymer cells, Journal of Power Sources 119-121 (2003) 833–837.
URL https://linkinghub.elsevier.com/retrieve/pii/S0378775303002817

[14] A. G. Hsieh, S. Bhadra, B. J. Hertzberg, P. J. Gjeltema, A. Goy, J. W. Fleischer, D. A. Steingart, Electrochemical-acoustic time of flight: in operando correlation of physical dynamics with battery charge and health, Energy & Environmental Science 8 (5) (2015) 1569–1577.
URL http://xlink.rsc.org/?DOI=C5EE00111K

[15] G. Davies, K. W. Knehr, B. Van Tassell, T. Hodson, S. Biswas, A. G. Hsieh, D. A. Steingart, State of Charge and State of Health Estimation Using Electrochemical Acoustic Time of Flight Analysis, Journal of The Electrochemical Society 164 (12) (2017) A2746–A2755.
URL https://iopscience.iop.org/article/10.1149/2.1411712jes

[16] L. Gold, T. Bach, W. Virsik, A. Schmitt, J. Müller, T. E. Staab, G. Sextl, Probing lithium-ion batteries' state-of-charge using ultrasonic transmission – Concept and laboratory testing, Journal of Power Sources 343 (2017) 536–544.
URL https://linkinghub.elsevier.com/retrieve/pii/S0378775317301003

[17] P. Ladpli, F. Kopsaftopoulos, F.-K. Chang, Estimating state of charge and health of lithium-ion batteries with guided waves using built-in piezoelectric sensors/actuators, Journal of Power Sources 384 (2018) 342–354.
URL https://linkinghub.elsevier.com/retrieve/pii/S0378775318301770

[18] P. Ladpli, C. Liu, F. Kopsaftopoulos, F.-K. Chang, Estimating Lithium-ion Battery State of Charge and Health with Ultrasonic Guided Waves Using an Efficient Matching Pursuit Technique, in: 2018 IEEE Transportation Electrification Conference and Expo, Asia-Pacific (ITEC Asia-Pacific), IEEE, Bangkok, Thailand, 2018, pp. 1–5.
URL https://ieeexplore.ieee.org/document/8433297/

[19] H. Popp, G. Glanz, K. Alten, I. Gocheva, W. Berghold, A. Bergmann, Mechanical Frequency Response Analysis of Lithium-Ion Batteries to Disclose Operational Parameters, Energies 11 (3) (2018) 541.
URL http://www.mdpi.com/1996-1073/11/3/541

[20] H. Popp, M. Koller, S. Keller, G. Glanz, R. Klambauer, A. Bergmann, State Estimation Approach of Lithium-Ion Batteries by Simplified Ultrasonic Time-of-Flight Measurement, IEEE Access 7 (2019) 170992–171000.
URL https://ieeexplore.ieee.org/document/8911334/

[21] K. Fröhlich, Next generation HE-NMC cathodes for advanced lithium-ion batteries, Ph.D. thesis, Vienna University of Technology, Vienna, Austria (2018).
URL http://repositum.tuwien.ac.at/urn:nbn:at:at-ubtuw:1-110823

[22] H. Popp, N. Zhang, M. Jahn, M. Arrinda, S. Ritz, M. Faber, D. U. Sauer, P. Azais, I. Cendoya, Ante-mortem analysis, electrical, thermal, and ageing testing of state-of-the-art cylindrical lithium-ion cells, e & i Elektrotechnik und Informationstechnik.
URL http://link.springer.com/10.1007/s00502-020-00814-9

[23] M. Lewerenz, D. U. Sauer, Evaluation of cyclic aging tests of prismatic automotive LiNiMnCoO2-Graphite cells considering influence of homogeneity and anode overhang, Journal of Energy Storage 18 (2018) 421–434.
URL https://linkinghub.elsevier.com/retrieve/pii/S2352152X18301579

[24] J. Smekens, R. Gopalakrishnan, N. Steen, N. Omar, O. Hegazy, A. Hubin, J. Van Mierlo, Influence of Electrode Density on the Performance of Li-Ion Batteries: Experimental and Simulation Results, Energies 9 (2) (2016) 104.
URL http://www.mdpi.com/1996-1073/9/2/104

[25] J. Xie, Y.-C. Lu, A retrospective on lithium-ion batteries, Nature Communications 11 (1) (2020) 2499.
URL http://www.nature.com/articles/s41467-020-16259-9

[26] N. Nitta, F. Wu, J. T. Lee, G. Yushin, Li-ion battery materials: present and future, Materials Today 18 (5) (2015) 252–264.
URL https://linkinghub.elsevier.com/retrieve/pii/S1369702114004118

[27] V. A. Nguyen, C. Kuss, Review—Conducting Polymer-Based Binders for Lithium-Ion Batteries and Beyond, Journal of The Electrochemical Society 167 (6) (2020) 065501.
URL https://iopscience.iop.org/article/10.1149/1945-7111/ab856b

[28] R. Wang, L. Feng, W. Yang, Y. Zhang, Y. Zhang, W. Bai, B. Liu, W. Zhang, Y. Chuan, Z. Zheng, H. Guan, Effect of Different Binders on the Electrochemical Performance of Metal Oxide Anode for Lithium-Ion Batteries, Nanoscale Research Letters 12 (1) (2017) 575.
URL http://nanoscalereslett.springeropen.com/articles/10.1186/s11671-017-2348-6

[29] P. Shi, X. Zhang, X. Shen, R. Zhang, H. Liu, Q. Zhang, A Review of Composite Lithium Metal Anode for Practical Applications, Advanced Materials Technologies 5 (1) (2020) 1900806.
URL https://onlinelibrary.wiley.com/doi/abs/10.1002/admt.201900806

[30] R. Wang, W. Cui, F. Chu, F. Wu, Lithium metal anodes: Present and future, Journal of Energy Chemistry 48 (2020) 145–159.
URL https://linkinghub.elsevier.com/retrieve/pii/S2095495620300012

[31] T. Placke, R. Kloepsch, S. Dühnen, M. Winter, Lithium ion, lithium metal, and alternative rechargeable battery technologies: the odyssey for high energy density, Journal of Solid State Electrochemistry 21 (7) (2017) 1939–1964.
URL http://link.springer.com/10.1007/s10008-017-3610-7

[32] G. E. Blomgren, The Development and Future of Lithium Ion Batteries, Journal of The Electrochemical Society 164 (1) (2017) A5019–A5025.
URL https://iopscience.iop.org/article/10.1149/2.0251701jes

[33] J. Asenbauer, T. Eisenmann, M. Kuenzel, A. Kazzazi, Z. Chen, D. Bresser, The success story of graphite as a lithium-ion anode material – fundamentals, remaining challenges, and recent developments including silicon (oxide) composites, Sustainable Energy & Fuels (2020) 10.1039.D0SE00175A.
URL http://xlink.rsc.org/?DOI=D0SE00175A

[34] M. Krajewski, B. Hamankiewicz, M. Michalska, M. Andrzejczuk, L. Lipinska, A. Czerwinski, Electrochemical properties of lithium–titanium oxide, modified with Ag–Cu particles, as a negative electrode for lithium-ion batteries, RSC Advances 7 (82) (2017) 52151–52164.
URL http://xlink.rsc.org/?DOI=C7RA10608D

[35] Altairnano, 70 Amp Hour Cell (2020).
URL https://altairnano.com/products/70-amp-hour-cell/

[36] A. Rezqita, A.-R. Kathribail, J. Kahr, M. Jahn, Analysis of Degradation of Si/Carbon||LiNi $_{0.5}$ Mn $_{0.3}$ Co $_{0.2}$ O $_{2}$ Full Cells: Effect of Prelithiation, Journal of The Electrochemical Society 166 (3) (2019) A5483–A5488.
URL https://iopscience.iop.org/article/10.1149/2.0671903jes

[37] A. Manthiram, A reflection on lithium-ion battery cathode chemistry, Nature Communications 11 (1) (2020) 1550.
URL http://www.nature.com/articles/s41467-020-15355-0

[38] C. Lin, A. Tang, H. Mu, W. Wang, C. Wang, Aging Mechanisms of Electrode Materials in Lithium-Ion Batteries for Electric Vehicles, Journal of Chemistry 2015 (2015) 1–11.
URL http://www.hindawi.com/journals/jchem/2015/104673/

[39] A. Barré, B. Deguilhem, S. Grolleau, M. Gérard, F. Suard, D. Riu, A review on lithium-ion battery ageing mechanisms and estimations for automotive applications, Journal of Power Sources 241 (2013) 680–689.
URL https://linkinghub.elsevier.com/retrieve/pii/S0378775313008185

[40] M. R. Palacín, Understanding ageing in Li-ion batteries: a chemical issue, Chemical Society Reviews 47 (13) (2018) 4924–4933.
URL http://xlink.rsc.org/?DOI=C7CS00889A

[41] D. P. Finegan, S. J. Cooper, B. Tjaden, O. O. Taiwo, J. Gelb, G. Hinds, D. J. Brett, P. R. Shearing, Characterising the structural properties of polymer separators for lithium-ion batteries in 3D using phase contrast X-ray microscopy, Journal of Power Sources 333 (2016) 184–192.
URL https://linkinghub.elsevier.com/retrieve/pii/S0378775316313222

[42] R. Schröder, M. Aydemir, G. Seliger, Comparatively Assessing different Shapes of Lithium-ion Battery Cells, Procedia Manufacturing 8 (2017) 104–111.
URL https://linkinghub.elsevier.com/retrieve/pii/S2351978917300173

[43] DNP, DNP Battery Pouch Film for Li-Ion battery (2018).
URL https://www.dnp.co.jp

[44] L. Lao, Y. Su, Q. Zhang, S. Wu, Thermal Runaway Induced Casing Rupture: Formation Mechanism and Effect on Propagation in Cylindrical Lithium Ion Battery Module, Journal of The Electrochemical Society 167 (9) (2020) 090519.
URL https://iopscience.iop.org/article/10.1149/1945-7111/ab8807

[45] J. Deng, I. Smith, C. Bae, P. Rairigh, T. Miller, B. Surampudi, P. L'Eplattenier, I. Caldichoury, Impact Modeling and Testing of Pouch and Prismatic Cells, Journal of The Electrochemical Society 167 (9) (2020) 090550.
URL https://iopscience.iop.org/article/10.1149/1945-7111/ab9962

[46] J. Vetter, P. Novák, M. Wagner, C. Veit, K.-C. Möller, J. Besenhard, M. Winter, M. Wohlfahrt-Mehrens, C. Vogler, A. Hammouche, Ageing mechanisms in lithium-ion batteries, Journal of Power Sources 147 (1-2) (2005) 269–281.
URL https://linkinghub.elsevier.com/retrieve/pii/S0378775305000832

[47] M. Lewerenz, Dissection and quantitative description of aging of lithium-ion batteries using non-destructive methods validated by post-mortem-analyses, Vol. RWTH Aachen University, RWTH Aachen University, 2018.
URL http://publications.rwth-aachen.de/record/741889

[48] K. Edström, T. Gustafsson, J. Thomas, The cathode–electrolyte interface in the Li-ion battery, Electrochimica Acta 50 (2-3) (2004) 397–403.
URL https://linkinghub.elsevier.com/retrieve/pii/S0013468604006486

[49] H. Popp, Analysis of Lithium Ion System with Electrochemical Impedance Spectroscopy Methods (EIS) for Addressing the Modelling of Ageing Phenomena, Master's thesis, FH Technikum Wien, Wien, publisher: Unpublished (2010).
URL http://rgdoi.net/10.13140/2.1.4167.5842

[50] Energy Ville, BatteryStandards.Info (2020).
URL https://www.batterystandards.info/

[51] P. Keil, A. Jossen, Aging of Lithium-Ion Batteries in Electric Vehicles: Impact of Regenerative Braking, 2015, publisher: Unpublished.
URL http://rgdoi.net/10.13140/RG.2.1.3485.2320

[52] I. E. Commission, IEC 62660-1:2018 Secondary lithium-ion cells for the propulsion of electric road vehicles - Part 1: Performance testing, Tech. rep. (2018).
URL https://webstore.iec.ch/publication/28965

[53] International Standardization Organization, ISO 12405-1:2011 Electrically propelled road vehicles — Test specification for lithium-ion traction battery packs and systems — Part 1: High-power applications, Tech. rep.
URL https://www.iso.org/cms/render/live/en/sites/isoorg/contents/data/standard/05/14/51414.html

[54] B. Hull, V. John, Non destructive testing, Macmillan Education, Basingstoke, 1988, oCLC: 246786072.

[55] J. Prasad, C. G. Krishnadas Nair, Non-destructive test and evaluation of materials, McGraw-Hill Education LLC., New York, N.Y., 2011, oCLC: 897451326.
URL https://www.accessengineeringlibrary.com/content/book/9780070707030

[56] K. Schiebold, Zerstörungsfreie Werkstoffprüfung - Eindringprüfung, Springer Berlin Heidelberg, Berlin, Heidelberg, 2014.
URL http://link.springer.com/10.1007/978-3-662-43809-1

[57] K. Schiebold, Zerstörungsfreie Werkstoffprüfung - Sichtprüfung, Springer Berlin Heidelberg, Berlin, Heidelberg, 2015.
URL http://link.springer.com/10.1007/978-3-662-44667-6

[58] H. Zappen, G. Fuchs, A. Gitis, D. U. Sauer, In-Operando Impedance Spectroscopy and Ultrasonic Measurements during High-Temperature Abuse Experiments on Lithium-Ion Batteries, Batteries 6 (2) (2020) 25.
URL https://www.mdpi.com/2313-0105/6/2/25

[59] L. Oca, N. Guillet, R. Tessard, U. Iraola, Lithium-ion capacitor safety assessment under electrical abuse tests based on ultrasound characterization and cell opening, Journal of Energy Storage 23 (2019) 29–36.
URL https://linkinghub.elsevier.com/retrieve/pii/S2352152X19300210

[60] C. Bommier, W. Chang, Y. Lu, J. Yeung, G. Davies, R. Mohr, M. Williams, D. Steingart, In Operando Acoustic Detection of Lithium Metal Plating in Commercial LiCoO2/Graphite Pouch Cells, Cell Reports Physical Science 1 (4) (2020) 100035.
URL https://linkinghub.elsevier.com/retrieve/pii/S2666386420300254

[61] F. B. Spingler, W. Wittmann, J. Sturm, B. Rieger, A. Jossen, Optimum fast charging of lithium-ion pouch cells based on local volume expansion criteria, Journal of Power Sources 393 (2018) 152–160.
URL https://linkinghub.elsevier.com/retrieve/pii/S0378775318304440

[62] H. Popp, M. Luthfi, J.-H. Han, R. Klambauer, A. Bergmann, In-Situ Investigation of Lithium-Ion Batteries by Combined Mechanical FRF and Dilatometer Measurements, 2018, publisher: Unpublished.
URL http://rgdoi.net/10.13140/RG.2.2.35056.10240

[63] D. Liu, Z. Shadike, R. Lin, K. Qian, H. Li, K. Li, S. Wang, Q. Yu, M. Liu, S. Ganapathy, X. Qin, Q. Yang, M. Wagemaker, F. Kang, X. Yang, B. Li, Review of Recent Development of In Situ/Operando Characterization Techniques for Lithium Battery Research, Advanced Materials 31 (28) (2019) 1806620.
URL https://onlinelibrary.wiley.com/doi/abs/10.1002/adma.201806620

[64] J. Conder, C. Marino, P. Novák, C. Villevieille, Do imaging techniques add real value to the development of better post-Li-ion batteries?, Journal of Materials Chemistry A 6 (8) (2018) 3304–3327.
URL http://xlink.rsc.org/?DOI=C7TA10622J

[65] Y. Plotnikov, J. Karp, A. Knobloch, C. Kapusta, D. Lin, Eddy current sensor for in-situ monitoring of swelling of Li-ion prismatic cells, Boise, Idaho, 2015, pp. 434–442.
URL http://aip.scitation.org/doi/abs/10.1063/1.4914639

[66] A. Knobloch, J. Karp, Y. Plotnikov, C. Kapusta, J. Siegel, N. Samad, A. Stefanopoulou, Novel thin temperature and expansion sensors for li-ion battery monitoring, in: 2017 IEEE SENSORS, IEEE, Glasgow, 2017, pp. 1–3.
URL http://ieeexplore.ieee.org/document/8234066/

[67] B. J. Schwarz, M. H. Richardson, Experimental Modal Analysis, Orlando, FL, 1999, p. 12.

[68] P. Avitabile, Modal testing: a practitioner's guide, first edition Edition, Wiley, Hoboken, NJ, 2017, oCLC: 1006745701.

[69] J. M. Hooper, J. Marco, Experimental modal analysis of lithium-ion pouch cells, Journal of Power Sources 285 (2015) 247–259.
URL https://linkinghub.elsevier.com/retrieve/pii/S0378775315005145

[70] T. Wang, O. Celik, F. N. Catbas, L. Zhang, Practical Calibration Techniques for the Modal Impact Hammer, in: E. Wee Sit (Ed.), Sensors and Instrumentation, Volume 5, Springer International Publishing, Cham, 2015, pp. 23–29, series Title: Conference Proceedings of the Society for Experimental Mechanics Series.
URL http://link.springer.com/10.1007/978-3-319-15212-7_3

[71] P. Berg, J. Soellner, A. Jossen, Structural dynamics of lithium-ion cells – Part I: Method, test bench validation and investigation of lithium-ion pouch cells, Journal of Energy Storage 26 (2019) 100916.
URL https://linkinghub.elsevier.com/retrieve/pii/S2352152X19304001

[72] G. F. Lang, The Coherence Function - A Brief Review (Jan. 2015).
URL https://www.crystalinstruments.com/blog/2015/1/12/the-coherence-function-a-brief-review

[73] K. Schiebold, Zerstörungsfreie Werkstoffprüfung - Ultraschallprüfung, Springer Berlin Heidelberg, Berlin, Heidelberg, 2015.
URL http://link.springer.com/10.1007/978-3-662-44700-0

[74] Draw P and S waves illustration (Feb. 2020).
URL https://tex.stackexchange.com/a/528583

[75] Z. Su, L. Ye, Y. Lu, Guided Lamb waves for identification of damage in composite structures: A review, Journal of Sound and Vibration 295 (3-5) (2006) 753–780.
URL https://linkinghub.elsevier.com/retrieve/pii/S0022460X0600109X

[76] M. Lowe, Matrix techniques for modeling ultrasonic waves in multilayered media, IEEE Transactions on Ultrasonics, Ferroelectrics and Frequency Control 42 (4) (1995) 525–542.
URL http://ieeexplore.ieee.org/document/393096/

[77] J. Larsen, Correlation Functions and Power Spectra (2009).
URL https://www2.imm.dtu.dk/pubdb/edoc/imm4932.pdf

[78] H. Popp, M. Luthfi, J.-H. Han, R. Klambauer, A. Bergmann, In-Situ Investigation of Lithium-Ion Batteries by Combined Mechanical FRF and Dilatometer MeasurementsPublisher: Unpublished.
URL http://rgdoi.net/10.13140/RG.2.2.35056.10240

[79] M. Luthfi, State Estimation of Lithium Ion Battery Using Non-Invasive Method, Master's thesis, Cartinthia University of Applied Science, Austria, publisher: Unpublished (2018).
URL http://rgdoi.net/10.13140/RG.2.2.10223.28323

[80] H. Y. Choi, I. Lee, J. S. Lee, Y. M. Kim, H. Kim, A study on mechanical characteristics of lithium-polymer pouch cell battery for electric vehicle, Seoul, Republic of Korea, 2013, pp. 13–0115.

[81] B. Xia, F. Liu, C. Xu, Y. Liu, Y. Lai, W. Zheng, W. Wang, Experimental and Simulation Modal Analysis of a Prismatic Battery Module, Energies 13 (8) (2020) 2046.
URL https://www.mdpi.com/1996-1073/13/8/2046

[82] P. Ladpli, C. Liu, F. Kopsaftopoulos, F.-K. Chang, Health Prognostics of Lithium-ion Batteries and Battery-Integrated Structures, in: Structural Health Monitoring 2019, DEStech Publications, Inc., 2019.
URL http://www.dpi-proceedings.com/index.php/shm2019/article/view/32215

[83] J. B. Robinson, R. E. Owen, M. D. R. Kok, M. Maier, J. Majasan, M. Braglia, R. Stocker, T. Amietszajew, A. J. Roberts, R. Bhagat, D. Billsson, J. Z. Olson, J. Park, G. Hinds, A. Ahlberg Tidblad, D. J. L. Brett, P. R. Shearing, Identifying Defects in Li-Ion Cells Using Ultrasound Acoustic Measurements, Journal of The Electrochemical Society 167 (12) (2020) 120530.
URL https://iopscience.iop.org/article/10.1149/1945-7111/abb174

[84] B. Rieger, S. Schlueter, S. Erhard, J. Schmalz, G. Reinhart, A. Jossen, Multi-scale investigation of thickness changes in a commercial pouch type lithium-ion battery, Journal of Energy Storage 6 (2016) 213–221.
URL https://linkinghub.elsevier.com/retrieve/pii/S2352152X16300068

Appendix A

Publications

In the course of this thesis following work has been published and presented.

A.1 Journal Publications

1. Hartmut Popp, Gregor Glanz, Karoline Alten, Irina Gocheva, Wernfried Berghold, Alexander Bergmann;
   "Mechanical Frequency Response Analysis of Lithium-Ion Batteries to Disclose Operational Parameters";
   Energies, 11(3) (2018), Paper Number 541;
   https://doi.org/10.3390/en11030541

2. Hartmut Popp, Markus Koller, Severin Keller, Gregor Glanz, Reinhard Klambauer, Alexander Bergmann;
   "State Estimation Approach of Lithium-Ion Batteries by Simplified Ultrasonic Time-of-Flight Measurement";
   IEEE Access, 7 (2019), Pages 170992 - 171000;
   https://doi.org/10.1109/ACCESS.2019.2955556

3. Hartmut Popp, Markus Koller, Marcus Jahn, Alexander Bergmann;
   "Mechanical Methods for State Determination of Lithium-Ion Secondary Batteries: A Review";
   Journal of Energy Storage, 32, (2020), Paper Number 101859;
   https://doi.org/10.1016/j.est.2020.101859

A.2 Presentations at Conferences

1. Hartmut Popp;
   "Mechanical Frequency Response Analysis of Li-Ion Batteries";
   Invited Talk, TRA 2018, 16 - 19.04.2018, Vienna (Austria)

2. Hartmut Popp;
   "Mechanical Frequency Response Analysis of Li-Ion Batteries";
   Invited Talk, 5VB Workshop on "The Effect of Mechanical Aspects on Battery Performance over Lifetime", 26.04.2018, Graz (Austria)

3. Hartmut Popp, Muhammad Luthfi, Jong-Hee Han, Reinhard Klambauer, Alexander Bergmann;
   "In-Situ Investigation of Lithium-Ion Batteries by Combined Mechanical FRF and Dilatometer Measurements";
   Invited Talk, E-MRS Fall Meeting 2018, 17 - 20.09.2018, Warsaw (Poland)

4. Reinhard Klambauer, Severin Keller, Hartmut Popp, Alexander Bergmann;
   "Multiphysical Simulation of the Mechanical Frequency Response of a Li-Ion Battery Cell in respect of the Intercalation and De-intercalation of Ions";
   Talk, Batteries Conference, 02 - 05.10.2018, Nice (France)

A.3 Co-Supervision of Masters Thesis

1. Muhammad Luthfi;
   "State Estimation of Lithium Ion Battery Using Non-Invasive Method";
   Supervision: Markus Heinrici, Hartmut Popp;
   FH Kärnten Campus Villach, Master Electrical Energy and Mobility Systems, 2018;
   https://doi.org/10.13140/RG.2.2.10223.28323

Appendix B

Paper 1: ’Mechanical Frequency Response Analysis of Lithium-Ion Batteries to Disclose Operational Parameters’

energies

MDPI

Article

Mechanical Frequency Response Analysis of Lithium-Ion Batteries to Disclose Operational Parameters

Hartmut Popp [1,2,*], Gregor Glanz [1], Karoline Alten [3], Irina Gocheva [1], Wernfried Berghold [1] and Alexander Bergmann [2]

1 Center for Low-Emission Transport, AIT Austrian Institute of Technology, 1210 Vienna, Austria; gregor.glanz@ait.ac.at (G.G.); ir.gocheva@gmail.com (I.G.); wernfried.berghold@ait.ac.at (W.B.)
2 Institute of Electronic Sensor Systems, Graz University of Technology, 8010 Graz, Austria; alexander.bergmann@tugraz.at
3 Center for Mobility Systems, AIT Austrian Institute of Technology, 1210 Vienna, Austria; karoline.alten@ait.ac.at
* Correspondence: hartmut.popp@ait.ac.at

Received: 7 February 2018; Accepted: 27 February 2018; Published: 2 March 2018

Abstract: During the charge and discharge process, lithium-ion batteries change their mechanical properties due to internal structural changes caused by intercalation and de-intercalation of the ions in the anode and cathode. Furthermore, the behavior changes over the lifetime of the battery due to several degradation mechanisms. The mechanical properties of the cell hold valuable information for monitoring these changes and additionally provide data for mechanical construction and further optimization of battery systems. Hence, in this manuscript, the mechanical frequency response function is investigated as a non-destructive method to determine parameters such as stiffness and damping of pouch cells and their correlation with the state of charge (SOC), the state of health (SOH), and the temperature of the cell. Using a mechanical shaker and an impedance head, it is shown that low amplitude forces of only a few Newton and a low frequency region of several hundred Hertz already suffice to show differences in the state of charge and state of health as well as in mechanical properties and the dependencies on temperature. Also the limitations of the method are shown, as the frequency response is not distinct for each parameter and thus, at the moment, does not allow absolute determination of a single value without prior system knowledge.

Keywords: lithium-ion battery; modal analysis; mechanical excitation; state of charge; state of health; temperature

1. Introduction

In the past few years, significant advances in lithium-ion batteries (LIBs), due to their successful implementation in many applications, have led to extensive investigations. More recently, the focus of the research also includes the mechanical properties of active materials and of the full cell. LIBs are based on a rocking chair principle. During operation, the ions stored in active materials move from anode to cathode and vice versa. This leads to structural changes in the active materials that can be measured by various methods.

Changes in LIBs caused by lithium intercalation during cycling have been investigated typically by using X-ray techniques [1,2] and dilatometry [3]. Because dilatometry on half cells proved to be very useful for revealing relevant phenomena during operation [4], this path was also followed for full cells [4,5], where the authors reveal changes in the state of charge (SOC), the state of health (SOH), as well as other phenomena such as lithium plating by using a dial indicator [4] or multi-directional

laser scanning [5]. The first approach is easier to implement but it only measures the expansion on one point, while the second approach requires advanced equipment but has the benefit of depicting the dilation over the whole surface of the cell, thus providing information about local phenomena. Another form of dilatometry is performed by mounting strain gauges on the surface of pouch cells, which allows one to determine the SOC of the cell indirectly [6,7]. This approach is also coupled with neutron imaging to gain further insights and correlations [8]. Two recent publications have used ultrasonic measurements to gain information about the material properties [9,10]; the frequencies used are higher than 100 kHz. In both papers, a correlation of the frequency response to the SOC is found. It has to be highlighted that prior information about the cell's material properties has an impact on the proper interpretation and understanding of processes and reaction mechanisms within LIBs. There are various methods of their determination and the most suitable one should be implemented.

Vibration-based tests already play a major role in the characterization of mechanical properties in many areas. These non-destructive methods are well established in the fields of mechanical engineering [11,12], civil engineering [13], and structural dynamics [13,14]. Structural response techniques determine a sample's mechanical impedance by applying a known excitation signal to the body and by measuring its response in the form of vibration velocity or vibration acceleration. The ratio between the complex Fourier spectra of force and response shows how a body behaves at different frequencies. Thus, resonances and anti-resonances as well as their damping can be assessed. When using several sensor or excitation points on the investigated structure, the body's mode shapes can be determined through modal analysis. The amplitude and phase of the spectral ratio form the so-called frequency response function (FRF). The FRF typically shows a multitude of peaks, where each of these peaks represents a natural frequency, or eigenfrequency. Henceforth, the structure could be considered as a multi-degree of freedom system with corresponding masses and springs. This technique has hitherto not been the state of the art for LIBs. Changes in the cells' FRF depend on the material parameters, in particular their stiffness. Hence, in this work, the FRF is used to monitor changes in the active materials of LIBs as a supplementary way to determine the properties of the cells. Hooper and Marco [15] examined the mechanical properties of LIB pouch cells using modal analysis. In their experiments, a pulse excitation created with an impact hammer was applied. Consequently, a correlation between SOC and the frequency response was detected as the stiffness of the cell increased with higher SOC levels. LePham [16], in his Master's thesis, repeated sinusoidal excitation at different frequencies within the audible region in an attempt to determine a correlation between the FRF and the SOC of an LIB pouch cell. However, the measurement was limited to one cell at a particular temperature at the same SOH. As the parameters of interest vary extensively during a cell's lifespan, understanding the interdependencies of temperature and SOH and their influences on cell behavior become of key interest.

The following goals were stated for this work: first, the approach used by LePham [16] to determine the FRF at different SOC levels is reproduced and validated on an off-the-shelf 20 Ah pouch cell. This is realized by using a small inertial shaker with a frequency range from 20 Hz to 3 kHz. Further, the method is extended to a pouch cell of the same type but pre-aged by cycling to investigate the suitability of the method for used cells in general. In the next step, the new cell is subjected to measurements at selected temperature values to understand their influence on the FRF. Finally, the results are compared and discussed. The mechanical method presented allows us to disclose important cell characteristics and material properties by applying a non-invasive and non-destructive short-term measurement on the cell that does not require extensive equipment.

2. Experiment

For this study, commercially available large scale pouch cells from EIG (Energy Innovation Group (Cheonan, South Korea)) type C020 [17] were used.Operational parameters can be seen in Table 1. Two cells of the same type were measured, one being new and the other one having gone through an extensive cycle life history ($\geq$1500 equivalent full cycles) and thus showing significant

deterioration in performance. The cycled cell had a measured capacity of $C_m = 14.9$ Ah, resulting in a capacity-based SOH of 74.5%. Both cells were from the same batch to minimize the influence of variations in manufacturing. A cell comprising a graphite anode was chosen because graphite is known to show significant changes in structure during cycling because of the lithium staging process [18] and hence is commonly subjected to expansion/shrinkage dilatometry measurements [4,15,16].

Table 1. Overview of cell characteristics and specification.

Quantity	Value
Nominal Capacity	20 Ah
Nominal Voltage	3.65 V
Dimension	216 × 129 × 7.2 mm
Weight	418.6 g
Anode Material	Graphite (G)
Cathode Material	Nickel-Manganese-Cobalt-Oxide (NMC)

The set-up of the measurement (Figure 1) consisted of a force generator type TMS 2002E miniature inertial shaker and an impedance head type 288D01, both from PCB Piezotronics, Inc. (Depew, NY, USA). The impedance head was screwed to the base of the shaker and mounted in the center of the cell with ultra-thin double-sided adhesive tape. To avoid external influences and to provide vibration isolation, the cell was placed on a foam padding with a natural frequency well below the first natural frequency of the cell (see also Section 3).

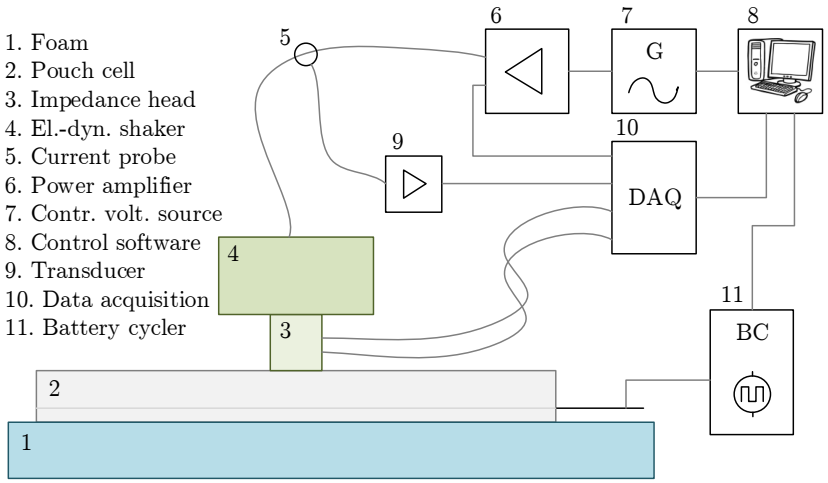

Figure 1. Functional diagram of the measurement set-up.

For excitation, the analogue output of a multifunction data acquisition board (DAQ) from National Instruments was used, and the signal was amplified with a power amplifier type 2706 from Brüel & Kjær (Nærum, Denmark). Data was acquired with the analogue inputs from the DAQ and signal conditioning amplifiers from Dewetron. Logged data includes the excitation voltage and current for the shaker as well as the force and the acceleration measured by the impedance head. The system was controlled with LabVIEW software (Version 2014, National Instruments, Austin, TX, USA), which generated the excitation signal and recorded the measured signals. The cycling and SOC adjustment was performed with self-developed battery cyclers. Each channel was calibrated, and the accuracy was 0.2% for the current and 0.1% for the voltage for measured value. During cycling and FRF measurement, the cells remained in the same position on the foam padding. The whole set-up was placed in a calibrated climatic chamber type VC4034 from Vötsch (Balingen, Germany) and remained unchanged during all tests on the same cell. The cell with the shaker, foam padding, and wiring placed in the climatic chamber can be seen in Figure 2.

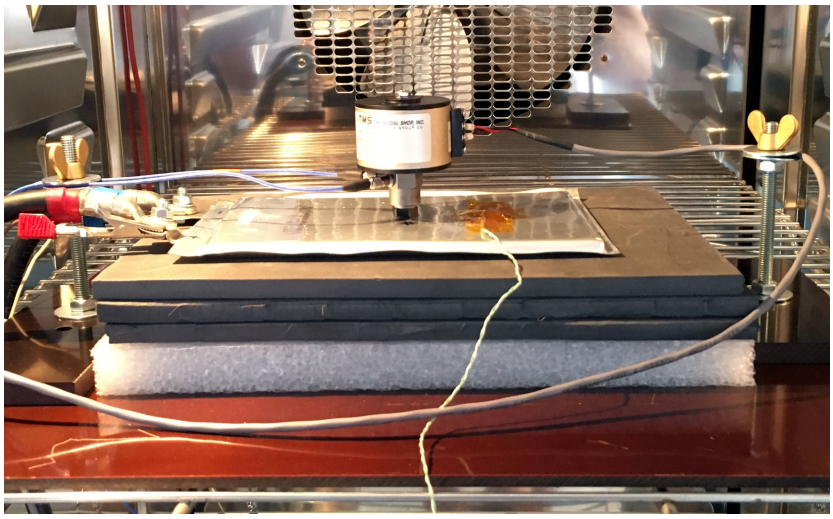

Figure 2. Image of test set-up within the climatic chamber.

To identify possible distortions of the signal that may be a result of mechanical vibrations of the environmental test chamber or human-induced vibration in the laboratory, initial measurements were performed under idle conditions (no thermal control, no activity in the laboratory) before being performed under real conditions (with thermal control and activity in the laboratory). Influences were found to be insignificant and below measurement accuracy. To minimize the influence of the electrical connection on the set-up, the wiring and the connection was done with strain relief units, establishing a loose connection. During measurements, the shaker operated within its recommended specification with a linear sinusoidal sweep from 20 Hz to 3 kHz. The sweep duration was set to 5 s, and the sampling rate was 25 kHz. Each sweep was repeated 3 times, and an average response was calculated. For the sweep duration, 2 and 10 s were also tested. As the eigenfrequency of the measurement set-up was 18 Hz (see also below) and the measurement was performed with a linear sweep, it was important to minimize the influences of the eigenfrequency on the values of interest. The decay time of the signal could be calculated with $\tau = \frac{1}{\delta}$ and $\delta = \omega \times D$, with D being the damping ratio. According to Table 2, our lowest D was about 0.1, assuming that the eigenfrequency has the same damping as the cell. This means that the 18 Hz frequency of the set-up impacts the 2 s measurement until a frequency of 1487.5 Hz, which includes the frequencies of interest. Thus, as a compromise between steady state conditions and measurement time, 5 s was chosen. The 18 Hz frequency was decayed by the time the shaker was excited at 297.5 Hz, which is already below our lowest frequencies of interest.

Table 2. Damping ratio of new and cycled cells for all SOC levels at all natural frequencies.

Cell	Eigenfrequency	SOC 0%	SOC 25%	SOC 50%	SOC 75%	SOC 100%
New	1.	0.2083	0.1849	0.1609	0.1339	0.1284
Cyc	1.	0.1113	0.1111	0.1115	0.1106	0.1111
New	2.	0.1563	0.1664	0.1245	0.1205	0.1225
Cyc	2.	0.0781	0.0779	0.0786	0.0775	0.0774
New	3.	0.1075	0.1074	0.1067	0.1052	0.1021
Cyc	3.	0.0718	0.0712	0.0743	0.0732	0.0729

The data was transferred to the frequency domain using a fast Fourier transformation algorithm implemented in an Octave mathematical environment. Different forces were tested to find out the optimum for the given cell. Overly strong force lead to bumps during measurement, producing unwanted noise, while too weak a force leads to very low amplitudes, which are hard to measure.

After several trials, an excitation of the given system, with a maximum force of 2.38 N and a root mean square force of 0.56 N, was determined as an optimum value. Applying such low force has the benefit of not changing any properties within the cell. Higher force or excitation over long periods are found to change the internal properties of the cell [2,19]; even when other work does not observe such an impact [20], it should not be neglected.

For cycling and SOC adjustment, the cells were first cycled with two standard cycles according to the manufacturer's specifications. This means a 0.5 C charge until 4.15 V with a constant voltage phase of 30 min and a discharge with 1 C down to 2.75 V, with C being the nominal capacity of the cell divided by 1 h. The capacity measured during the second discharge was then taken as the basis for further calculations. The measurement was performed at SOC levels 0, 25, 50, 75, and 100%. The FRF is determined starting from SOC 0% and charging to 100% and then again when discharging down to 0%. The SOC levels were set to a constant current charge and discharge, and a coulomb counting to the according value. A rest period of 90 min between SOC adjustment and measurement was set as the relaxation time.

When each cell was measured, the mechanical set-up remained untouched; when the cells were swapped, it was necessary to remove both the electrical connections as well as the shaker itself. Slight misalignments during the new set-up can affect the measured FRF, either in terms of the amplitude or, in the worst case, the measured frequency peaks due to different modes being excited if the shaker is in a different position and the peaks are closely spaced. To evaluate these uncertainties a 'blank' measurement was performed; thus, the set-up was fully assembled and disassembled six times for the cycled cell at SOC 0%, each time followed by a measurement of the FRF. The uncertainties are shown in Figure 3. It can be seen that the exact placement in the middle of the cell did lead to reproducible results regarding frequency stability for the regions of interest ($\leq$1400 Hz), while the amplitudes show stronger variations, especially for the fourth eigenfrequency peak. This variation in measurement needs to be considered for the results achieved for different cell types when the set-up is changed in between.

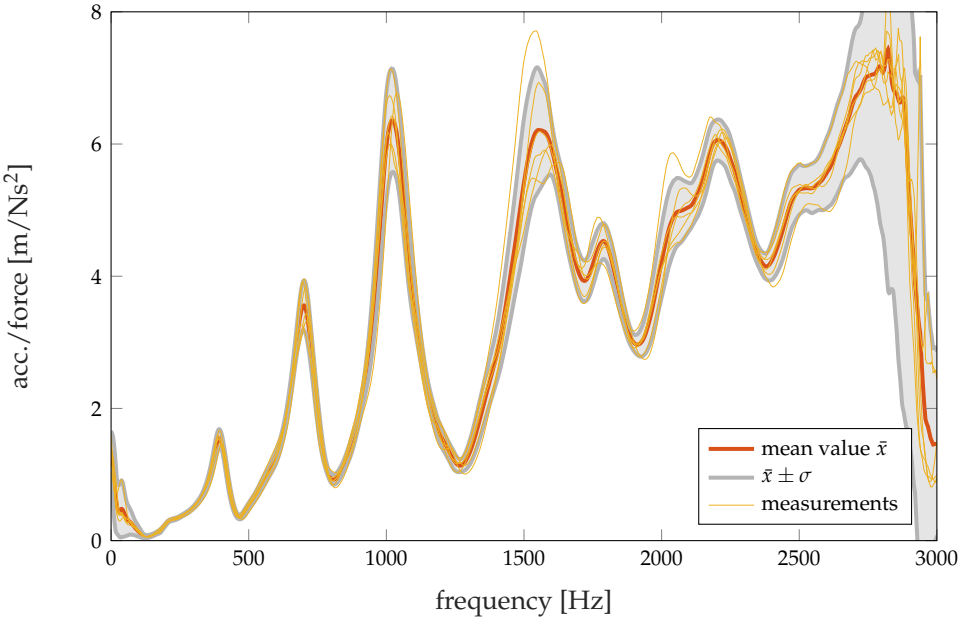

Figure 3. Mean value and standard deviation after full disassembly and reassembly of the set-up with the cycled cell (6 measurements).

To test the influence of the position of the shaker, a measurement was conducted with two additional impedance heads placed on the longitudinal and the lateral axes of the cell, 2 cm and 4 cm away from the center. With a higher distance from the center, a larger damping of the curve was

measured. Additionally, especially for lower frequencies, a shift of the peaks in the frequency domain was detected. Accurate placement of the shaker and impedance head of the cell is thus crucial for the reproducibility of this method.

The eigenfrequency of the foam bedding under the plate during the experimental set-up (i.e., including the load of the cell) was determined using the decaying vibration response after impulse loading. It was measured to be 18 Hz, indicating that the eigenfrequency of the set-up was well below any eigenfrequency of the cell itself and thus had a negligible impact on the subsequent measurements.

As temperature and temperature distribution have a high impact on cell performance [21], all measurements were taken under controlled environmental conditions. Cell temperature was measured with a thermocouple type K on the cells surface. When the surface reaches the test temperature ±1 °C, 2 h are needed to reach thermal equilibrium before measurements are taken.

All figures and the according measurement data can be found as supplementary material.

3. Results and Discussion

Figure 4a shows the smoothed FRF of the new cell for different SOC levels obtained during discharge at 25 °C. The full frequency range from 0 to 3000 Hz is displayed. The response at very low frequencies (≤100 Hz) resulted from the natural frequency of the foam material (see Section 2) and thus is not further considered. At higher frequencies, three distinct peaks can be seen in the FRF for this cell type. All are within the range of 400–1400 Hz, while the magnitudes become greater at higher frequencies. Above 1600 Hz, there is a plateau with only minor changes and a steep decline close to 3000 Hz, marking the frequency limit of the shaker. The FRF curves from 100 Hz upwards show a shift towards higher frequencies with increasing SOC. Using the equation of harmonic motion

$$k = \omega^2 m \tag{1}$$

where k defines the cell stiffness, ω the natural frequency, and m the mass of the cell, it can be seen that the cell becomes stiffer at higher SOC levels. Literature states that cells with a graphite-based anode show an increasing thickness during charging [4,22,23], mainly as a result of the volume change caused by staging of the anode during lithium intercalation [18], while the change in the cathode material is usually minor in comparison. Assuming the limited expansion within the pouch due to the surrounding materials, the observed increase in stiffness can be mainly linked to the staging process in the anode. The observation of higher stiffness at higher SOC levels is additionally supported by structural measurements on pure and on fully lithiated graphite (LiC_6), which can be found in literature. In [24], it is stated that LiC_6 has a significantly higher modulus of elasticity (E). That stiffness is calculated by $k = E\frac{A}{L}$, with A being the surface area and L being the length, indicates that the value of the stiffness of lithiated graphite is greater than that of pure graphite.

Figure 4b shows the FRF of the cycled cell. At first sight, the higher magnitude compared to the new cell is obvious. Considering potential measurement inaccuracies during rearrangement of the set-up (see Figure 3 and Section 2), not all of the changes in magnitude can be attributed to the decrease in SOH. The value for the 3rd eigenfrequency peak at approximately 1 kHz is 4.90 m/Ns^2 for the new cell and 6.79 m/Ns^2 for the cycled cell, with a standard deviation of 0.78 m/Ns^2 at this point, according to Figure 3. However, it can be stated that the shifts between the peaks of the aged cell at different SOCs in comparison to the new cell are much smaller. According to Equation (1), this indicates that, due to decreased reactivity, a cycled cell, though associated with inevitable degradation of the active materials, shows smaller changes in investigated mechanical characteristics with altering SOC. In other words, the stiffening is not so distinct with increasing SOC and, on average, the cycled cell appears to be less stiff than the new one. This is supposed to result from the irreversibly intercalated ions, the delamination, and the passivation films that formed a solid electrolyte interface, where the latter become more noticeable with every cycle [25].

Furthermore, it can be seen that the peaks of the cycled cell are narrower than those of the new one. This suggests a decrease in the damping ratio D of the cell with decreasing SOH. The damping ratio for each natural frequency can be approximated from

$$D = \frac{1}{2Q} \tag{2}$$

where Q is defined as the Quality-Factor

$$Q = \frac{\omega}{\Delta\omega} \tag{3}$$

where ω is the natural frequency, and $\Delta\omega$ is the frequency width between those points, which are half the maximum amplitude (full width at half maximum). Table 2 contains the damping ratios calculated for the three peaks at all SOC levels for both the new and the cycled cell. It can be seen that the changes in the damping ratio of the cycled cell at different SOC levels are much smaller than those of the new cell, providing a further indicator for significantly reduced reactivity in the active materials.

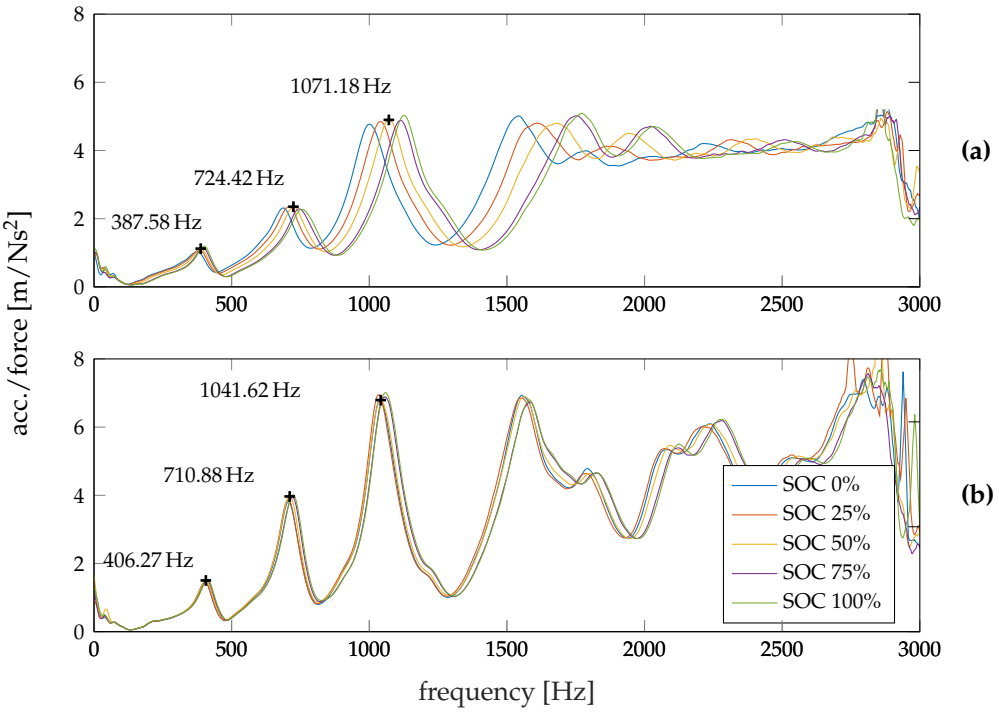

Figure 4. FRF of new (**a**) and cycled (**b**) cells during discharge for all SOC levels at 25 °C.

In Figure 5a the absolute change in frequency Δf and in Figure 5b the gradient of Δf for each SOC level is depicted for both cells in relation to SOC 0% at a temperature of 25 °C. The markers represent the peak frequencies for the first three eigenfrequencies. It is noteworthy that, for the absolute change in frequency, the new cell shows substantial fluctuations compared to the cycled cell; furthermore, this behavior is strongly manifested at higher SOC levels. This again is a strong indicator of significantly reduced system reactivity, which directly affects the measured capacity (dropped to 74.5% of the initial value). Most likely this reduced reactivity results from the formation of various passivation films, especially the Solid Electrolyte Interface (SEI), delamination, micro-cracking, and irreversible intercalated ions [25]. The figure also implies a trend in the peak shift for both cells towards higher frequencies up to SOC 75% and then decreases for SOC 100%. This has also been found in former work [16]. The underlying process has yet to be identified and requires a denser dataset between SOC 75 and 100%. However, this ambiguity, at the moment, inhibits a distinct correlation of the SOC with the FRF over the entire SOC range, but this correlation is possible at a lower SOC. The gradient of Δf shows the change in frequency scaled by the peak frequency at SOC 0%. This confirms the findings that an

aged cell can be easily distinguished from a new cell by charging or discharging it to a mid-range SOC of 50–75% and comparing the eigenfrequency peaks. Actually, determining the absolute SOC of a cell of unknown SOH is easier for new cells than for old ones, particularly at the aforementioned mid-range SOCs. The peaks of the eigenfrequency visible in Figure 4 and the given bandwidth in Figure 5 indicate that an SOC or SOH estimation can also be performed with a narrow frequency window. To estimate SOC and SOH using, for example, the third eigenfrequency, a window of 100 Hz around a center frequency of 1050 Hz is enough to detect all effects. This becomes practical for optimizing measurement time and saving equipment costs, especially considering a possible future application, for example, in an electric vehicle or a grid storage unit.

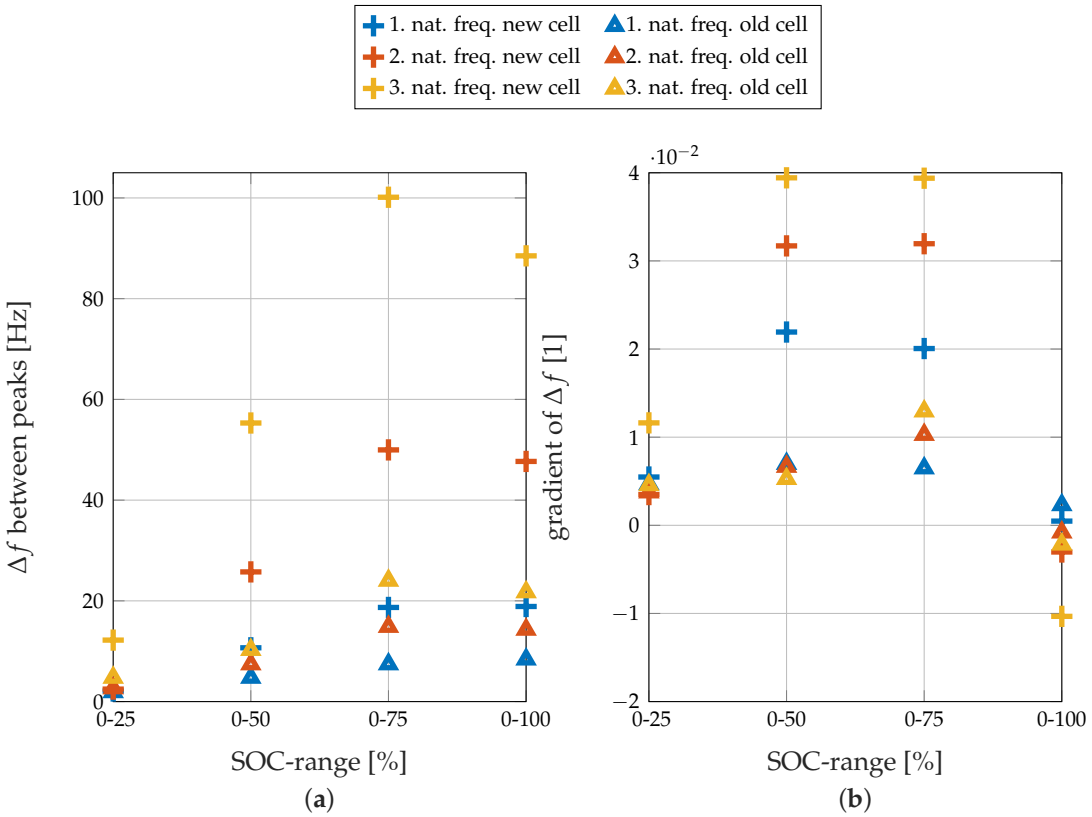

Figure 5. Absolute (**a**) distance between peaks and gradient (**b**) at different peaks of new and cycled cells during charge for all SOC levels at 25 °C.

The FRF of the cell at a certain SOC level varies, depending on how the SOC is reached. This is most likely due to the hysteresis effects of anode swelling, which could be related to the cell's charge or discharge history, or even the previous C-rate [22]. Figure 6 shows the FRF for the new cell for charge and discharge at selected SOC levels. It can be seen that there is a small shift in both magnitude and frequency for each SOC between the values reached by charging and those reached by discharging the cell. In [22], similar hysteresis behavior is found for thickness increases of an NMC/G cell and is identified as a result of the transformed intercalation structure during charge and discharge. The difference observed at SOC 0% originates in an altered discharging regime. While the initial SOC was reached with an uninterrupted discharge from SOC 100% down to 0%, the second value was reached by the stepwise discharge required for the measurement. Nevertheless, without existing prior knowledge about the system, this shift is not sufficient to allow for correlation of the frequency response directly to the SOC level.

The complete results obtained from the new and cycled cells imply that this method is appropriate for the indication of structural changes in the active materials caused by alterations in the state of the battery. It has to be underlined that, since the relevant frequency range is not very broad (no high

frequency set up required), the implementation of this method into test benches should be relatively easy, and is necessary for potential new applications of LIBs in the near future. The number and position of the peaks are a result of the form factor of the cell or object under test. For modules or hard case cells, more peaks and different shapes are to be expected.

Often LIBs are exposed to sharp temperature variations with regard to their vast spectrum of application, so the effect of the temperature change on the FRF is also investigated. In this scenario, the new cell is tested at 0, 25, and 45 °C at every SOC. For the sake of legibility, Figure 7 only shows two SOC values per temperature, but the other SOC levels exhibit similar behavior. It can be observed that the magnitude of the signal becomes greater with rising temperature, whereas the peaks shift to lower frequencies. Because the materials tend to soften at higher temperatures, their stiffness is reduced as they warm up, so natural frequencies are detected at lower values. Herewith, the influence of temperature becomes the dominating effect over frequency shifts due to changing SOC.

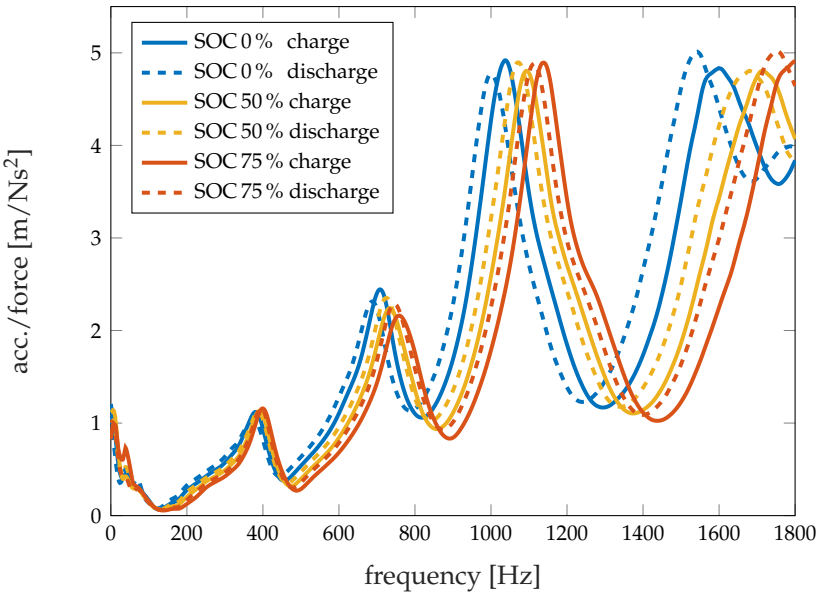

Figure 6. FRF of the new cell during charge and discharge for three SOC levels at 25 °C.

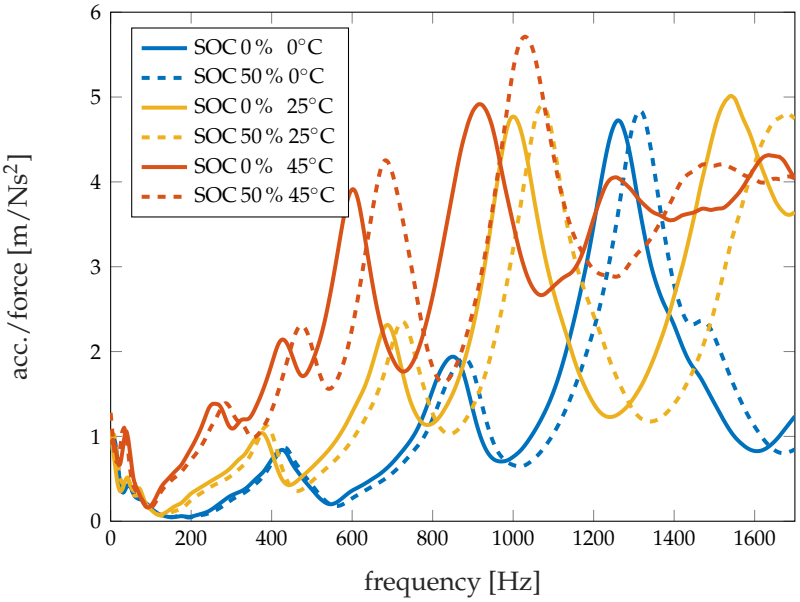

Figure 7. FRF of the new cell during discharge for SOC 0% and SOC 50% at three different temperatures.

In Figure 8, the natural frequencies of the system are presented. Their shifts indicate the changes in the cell´s mechanical properties. Because the first natural frequency shows an insignificant shift compared to the higher eigenfrequencies, the graph displays only the second and third natural frequencies for each SOC level relative to SOC 0% for all of the three chosen temperatures. A noticeable monotonic increase in all eigenfrequencies up to SOC 75% is detected at all temperature levels. For 0 and 25 °C, this monotonic increase continues up to SOC 100%, while at 45 °C for SOC 100% the frequency value is lower than the one measured at SOC 75%. In summary, at higher temperatures, the peak shifts are more pronounced, as expected, due to stimulated system reactivity with increased temperature. However, a noteworthy observation here is that, for SOC 25%, a greater change is observed at lower temperature values.

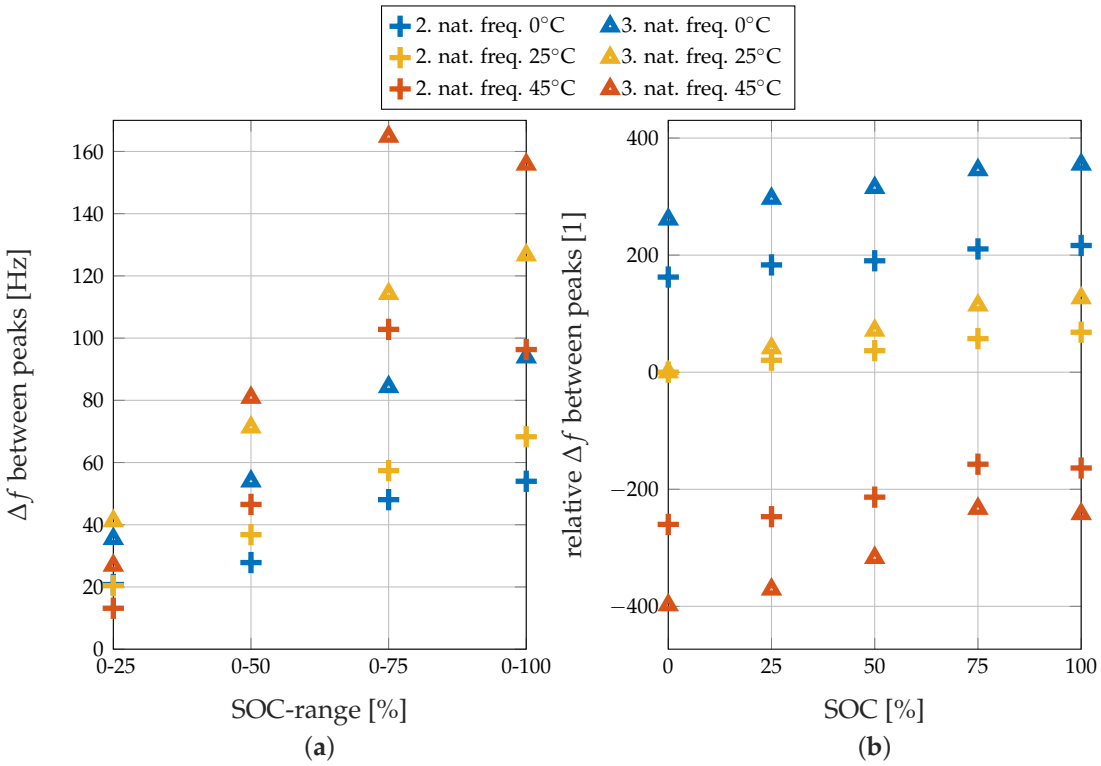

Figure 8. Distance (**a**) and relative distance to value at SOC 0% and 25 °C (**b**) between peaks of the new cell during discharge at three different temperatures.

4. Conclusions and Outlook

In this work, the correlation between the SOC and the FRF at low-frequency mechanical excitation of an LIB was presented. The obtained results show visible and distinct changes in the FRF with varying SOC, and reproducibly confirm detectable shifts with sharp temperature variations for the particular case of 20 Ah commercial pouch cells manufactured with NMC-cathode and G-anode. Since the test setting is well-defined and repeatable, it is projected that a determination of the SOC becomes feasible when prior knowledge about the system is available, although it is not sufficiently practical at the present moment. Nevertheless, at a given temperature, the FRF measurements could become a method of choice in determining the absolute SOC of the cells at a given temperature.

Regarding the SOH, it was found that the pre-aged cell with a long cycling-life history tends to become softer and that the absolute changes in the FRF are smaller than for a new cell, which could be attributed additionally to internal cracking, de-lamination, or fracture. However, the influence of other parameters on the FRF was found to be stronger than the influence of the SOH itself, which confirms that prior system knowledge is a major requirement for determination. This method is suitable for

monitoring changes of the mechanical parameters, which is very important during construction of battery systems, and highly relevant for the automotive sector [15,26,27]. Therefore, the approach presented in this work could assist as a non-destructive method of collecting information about parameters of the battery cell such as damping and stiffness. The non-destructive aspect is particularly relevant because other mechanical tests may bring undesirable side reactions and are thus often performed only at lower SOC [26,27]. The measurement procedure validated with our experiments is based on the frequencies within the audible range (in this case, from 20 Hz to 3 kHz); therefore, in comparison to ultrasonic analysis, requirements to this test, both for excitation and measurements, are not very demanding.

As a future goal for investigations, the actual changes in the materials have to be investigated (which may include different physico-chemical methods, including destructive tests), and the correlation between measured FRF values and factual changes in materials structure with regard to diverse cell chemistries and geometries should be defined. Refining the repeatability when reassembling the set-up is still necessary. Since swelling of the battery casing is also often observed during and after battery operation, especially on hard case prismatic cells [23], it is of utmost interest to consider this geometry type for modal analysis. For feasible future investigations, this would have a major impact on whole battery module systems.

Supplementary Materials: Supplementary materials can be found at http://www.mdpi.com/1996-1073/11/3/541/s1.

Acknowledgments: The work performed at the AIT Austrian Institute of Technology received partial funding from the European Union's Horizon 2020 research and innovation programme under the Grant Agreement No. 653331 (eCAIMAN). The authors wish to thank nbn Elektronik Austria for purchasing the shaker and impedance head.

Author Contributions: H.P. conceived and designed the experiments; G.G. performed the experiments; H.P., G.G., K.A., I.G. and A.B. analyzed the data; W.B. programmed the test bench software and supervised the measurements; All authors wrote parts of the paper.

Conflicts of Interest: The authors declare no conflict of interest.

Abbreviations

The following abbreviations and mathematical symbols are used in this manuscript:

C_m	measured capacity
C_n	nominal capacity
DAQ	data acquisition board
FRF	frequency response function
G	Graphite
LIB	lithium-ion battery
NMC	Nickel-Manganese-Cobalt-Oxide
SOC	state of charge
SOH	state of health
τ	decay time (s)
δ	decay constant
ω	natural frequency ($rads^{-1}$)
D	damping ratio
k	cell stiffness (N/m)
m	mass of the cell (kg)
f	frequency (s^{-1})
E	modulus of elasticity (N/m^2)
Q	quality factor

References

1. Wang, X.; Sone, Y.; Kuwajima, S. In Situ Investigation of the Volume Change in Li-ion Cell with Charging and Discharging: Satellite Power Applications. *J. Electrochem. Soc.* **2004**, *151*, A273–A280.
2. Somerville, L.; Hooper, J.M.; Marco, J.; McGordon, A.; Lyness, C.; Walker, M.; Jennings, P. Impact of Vibration on the Surface Film of Lithium-Ion Cells. *Energies* **2017**, *10*, 741, doi:10.3390/en10060741.
3. Lee, J.H.; Lee, H.M.; Ahn, S. Battery dimensional changes occurring during charge/discharge cycles—Thin rectangular lithium ion and polymer cells. *J. Power Sources* **2003**, *119*, 833–837.
4. Bauer, M.; Wachtler, M.; Stöwe, H.; Persson, J.V.; Danzer, M.A. Understanding the dilation and dilation relaxation behavior of graphite-based lithium-ion cells. *J. Power Sources* **2016**, *317*, 93–102.
5. Rieger, B.; Schuster, S.; Erhard, S.; Osswald, P.; Rheinfeld, A.; Willmann, C.; Jossen, A. Multi-directional laser scanning as innovative method to detect local cell damage during fast charging of lithium-ion cells. *J. Energy Storage* **2016**, *8*, 1–5.
6. Sommer, L.W.; Raghavan, A.; Kiesel, P.; Saha, B.; Schwartz, J.; Lochbaum, A.; Ganguli, A.; Bae, C.J.; Alamgir, M. Monitoring of Intercalation Stages in Lithium-Ion Cells over Charge-Discharge Cycles with Fiber Optic Sensors. *J. Electrochem. Soc.* **2015**, *162*, A2664–A2669.
7. Sommer, L.W.; Kiesel, P.; Ganguli, A.; Lochbaum, A.; Saha, B.; Schwartz, J.; Bae, C.J.; Alamgir, M.; Raghavan, A. Fast and slow ion diffusion processes in lithium ion pouch cells during cycling observed with fiber optic strain sensors. *J. Power Sources* **2015**, *296*, 46–52.
8. Siegel, J.B.; Stefanopoulou, A.G.; Hagans, P.; Ding, Y.; Gorsich, D. Expansion of Lithium Ion Pouch Cell Batteries: Observations from Neutron Imaging. *J. Electrochem. Soc.* **2013**, *160*, A1031–A1038.
9. Gold, L.; Bach, T.; Virsik, W.; Schmitt, A.; Müller, J.; Staab, T.E.; Sextl, G. Probing lithium-ion batteries' state-of-charge using ultrasonic transmission—Concept and laboratory testing. *J. Power Sources* **2017**, *343*, 536–544.
10. Hsieh, A.G.; Bhadra, S.; Hertzberg, B.J.; Gjeltema, P.J.; Goy, A.; Fleischer, J.W.; Steingart, D.A. Electrochemical-acoustic time of flight: in operando correlation of physical dynamics with battery charge and health. *Energy Environ. Sci.* **2015**, *8*, 1569–1577.
11. Löfdahl, M.; Johnsson, R.; Nykänen, A. Mobility measurement in six DOFs applied to the hub of a car. *Appl. Acoust.* **2014**, *83*, 108–115.
12. Harne, R.L.; Goodpaster, B.A. Impedance measures in analysis and characterization of multistable structures subjected to harmonic excitation. *Mech. Syst. Signal Process.* **2018**, *98*, 78–90.
13. Li, M.; van Keulen, W.; Ceylan, H.; Cao, D.; van de Ven, M.; Molenaar, A. Pavement stiffness measurements in relation to mechanical impedance. *Constr. Build. Mater.* **2016**, *102*, 455–461.
14. Noël, J.; Kerschen, G. Nonlinear system identification in structural dynamics: 10 more years of progress. *Mech. Syst. Signal Process.* **2017**, *83*, 2–35.
15. Hooper, J.M.; Marco, J. Experimental modal analysis of lithium-ion pouch cells. *J. Power Sources* **2015**, *285*, 247–259.
16. Pham, H.L. Health Diagnosis of Lithium-Ion Battery Cell Using Vibration-Based Test and Analysis. Master's Thesis, Purdue University, West Lafayette, IN, USA, 2013.
17. EIG. *Datasheet EIG C020*; Energy Innovation Group: Cheonan, South Korea, 2016.
18. Sethuraman, V.A.; Hardwick, L.J.; Srinivasan, V.; Kostecki, R. Surface structural disordering in graphite upon lithium intercalation/deintercalation. *J. Power Sources* **2010**, *195*, 3655–3660.
19. Hooper, J.M.; Marco, J.; Chouchelamane, G.H.; Lyness, C. Vibration Durability Testing of Nickel Manganese Cobalt Oxide (NMC) Lithium-Ion 18,650 Battery Cells. *Energies* **2016**, *9*, 52, doi:10.3390/en9010052.
20. Hooper, J.M.; Marco, J.; Chouchelamane, G.H.; Lyness, C.; Taylor, J. Vibration Durability Testing of Nickel Cobalt Aluminum Oxide (NCA) Lithium-Ion 18,650 Battery Cells. *Energies* **2016**, *9*, 281, doi:10.3390/en9040281.
21. Panchal, S.; Dincer, I.; Agelin-Chaab, M.; Fraser, R.; Fowler, M. Experimental and simulated temperature variations in a LiFePO4-20Ah battery during discharge process. *Appl. Energy* **2016**, *180*, 504–515.
22. Grimsmann, F.; Brauchle, F.; Gerbert, T.; Gruhle, A.; Knipper, M.; Parisi, J. Hysteresis and current dependence of the thickness change of lithium-ion cells with graphite anode. *J. Energy Storage* **2017**, *12*, 132–137.
23. Oh, K.Y.; Siegel, J.B.; Secondo, L.; Kim, S.U.; Samad, N.A.; Qin, J.; Anderson, D.; Garikipati, K.; Knobloch, A.; Epureanu, B.I.; et al. Rate dependence of swelling in lithium-ion cells. *J. Power Sources* **2014**, *267*, 197–202.

24. Kganyago, K.R.; Ngoepe, P.E. Structural and electronic properties of lithium intercalated graphite LiC_6. *Phys. Rev. B* **2003**, *68*, 205111.
25. Barré, A.; Deguilhem, B.; Grolleau, S.; Gérard, M.; Suard, F.; Riu, D. A review on lithium-ion battery ageing mechanisms and estimations for automotive applications. *J. Power Sources* **2013**, *241*, 680–689.
26. Tsutsui, W.; Siegmund, T.; Parab, N.D.; Liao, H.; Nguyen, T.N.; Chen, W. State-of-Charge and Deformation-Rate Dependent Mechanical Behavior of Electrochemical Cells. *Exp. Mech.* **2017**, doi:10.1007/s11340-017-0282-2.
27. Xu, J.; Liu, B.; Hu, D. State of charge dependent mechanical integrity behavior of 18650 lithium-ion batteries. *Sci. Rep.* **2016**, *6*, 21829.

Appendix C

Paper 2: 'State Estimation Approach of Lithium-Ion Batteries by Simplified Ultrasonic Time-of-Flight Measurement'

IEEE Access
Multidisciplinary ⋮ Rapid Review ⋮ Open Access Journal

Received October 24, 2019, accepted November 12, 2019. Date of publication xxxx 00, 0000, date of current version xxxx 00, 0000.

Digital Object Identifier 10.1109/ACCESS.2019.2955556

State Estimation Approach of Lithium-Ion Batteries by Simplified Ultrasonic Time-of-Flight Measurement

HARTMUT POPP[1,2], (Student Member, IEEE), MARKUS KOLLER[1], SEVERIN KELLER[2], GREGOR GLANZ[1], REINHARD KLAMBAUER[2], AND ALEXANDER BERGMANN[2]

[1]Center for Low-Emission Transport, AIT Austrian Institute of Technology, 1210 Vienna, Austria
[2]Institute of Electronic Sensor Systems, Graz University of Technology, 8010 Graz, Austria

Corresponding author: Hartmut Popp (hartmut.popp@ait.ac.at)

This work was supported by the Austrian Research Promotion Agency (FFG) under Grant 865148.

ABSTRACT This work presents an approach to monitoring the State-Of-Charge of Lithium-Ion battery cells via piezo disc-based ultrasonic Time-Of-Flight measurement by measuring the traveling time of a mechanical pulse through the cell between two surface-mounted sensors. The main advantage of this approach is the simplicity and the resulting low cost, which makes it suitable for future application in battery management systems. In detail, the excitation of the piezo actuator is done using a single semiconductor switch instead of a power amplifier, and the received signal is processed with an amplifier and Schmitt-trigger combination to condition the signal for the microprocessor, which is part of a battery management system. Both the functionality and the limits of the design are evaluated with a high energy density Lithium-Ion pouch cell under different operational scenarios. Several parameters such as temperature, current rates, and excitation frequency are varied to prove the design concept. For validation purposes, an estimation function is generated and a real-world driving cycle applied. An estimation with an error of 1.29 % of the Time-Of-Flight total value or 16.85 % of the State-Of-Charge value under challenging conditions is achieved with the current setup.

INDEX TERMS Battery management system, diagnostics, lithium-ion battery, piezoelectric transducers, state-of-charge, time-of-flight, ultrasonic.

I. INTRODUCTION

Due to their high energy density and long lifetime, Lithium-Ion batteries (LIBs) are nowadays predominant in mobile applications, modern stationary storage solutions, and in electric vehicles, and will maintain this position in the near and mid-term future [1]. One very important aspect of ensuring the longevity and safety of LIBs is proper operation within the constraints of the systems. This is the task of the battery management system (BMS). Determining the state-of-charge (SOC) of the battery is one of its key functionalities [2], [3]. Xiong et al. [3] in their review state that in principle there are four groups of methods to do so:

1) lookup table,
2) ampere-hour integral,
3) model based estimation, and
4) data driven.

These methods have in common that they all rely on measurement of the electrical two-pole behaviour of the cell, with the more sophisticated methods combining the actual measurement with cell temperature and operational history of the battery. So, the SOC is measured in an indirect way, or derived from other values.

In recent years, methods where the SOC is determined in a direct way via non-destructive, in-situ measurements of the properties of the active materials in the cell have been investigated more deeply by various research groups. The reason is that during operation the Li^+ ions move from anode to cathode upon discharge and vice versa during charge. This leads to SOC-dependent structural changes in both electrodes, with a very pronounced change for anodes containing e.g. graphite [4] or silicon [5]. While graphite expands up

The associate editor coordinating the review of this manuscript and approving it for publication was Fabio Massaro.

to around 10 % from the unlithiated to the lithiated state, the change becomes drastic for silicon, which can expand by around 300 %, so in the future direct determination will be of even higher relevance. There are three main groups of methods to determine the internals states:

1) imaging,
2) dilatometry, and
3) acoustics,

with the first and second having been employed on LIB full cells since the beginning of this century [6], [7] while the third has been receiving more attention over the last years [2], [8]–[12]. Hsieh *et al.* [8] employ acoustic ultrasonic measurements in transmission and reflection geometry, Ladpli *et al.* [9], [10] and Gold *et al.* [2] combine ultrasonic time-of-flight (TOF) and amplitude measurements, and Popp *et al.* [11] use acoustic signals in the audible range. All authors were able to identify correlations between the acoustic response of the system and the SOC, and partially also the SOH. All authors used complex and expensive lab equipment and did tests with artificial cycles that cannot be found in real world applications. Only one work [11] investigated the phenomena at different temperatures and found significant dependencies.

This work now opted for utilization of the technique of acoustic ultrasonic surface TOF signals in the range of 25 kHz to 40 kHz, as they are comparatively easy to measure. The whole setup aims at integration into a BMS. Thus, it is designed with electronic equipment of a total additional cost in the single-digit Euro range per unit, excluding economies of scale. To achieve the stated cost reduction, the circuit was assembled with inexpensive piezo actuator discs; instead of excitation with an amplifier and the corresponding complex signal generation, control of the actuator disc was maintained with an electronic switch, while the measurement of the TOF employing a Schmitt-trigger based circuit and the possibility to control the circuit using spare channels on the existing microprocessor from the BMS were realized.

The designed circuit passed the initial functionality tests. Feasibility tryouts and TOF behaviour were investigated on an off-the-shelf 12 Ah high energy pouch cell at different experimental conditions. The cell was operated with a real world driving cycle, the worldwide harmonized light vehicle test procedure (WLTP) [13] cycle. WLTP is the standard test nowadays for evaluation of energy consumption of passenger cars and reflects various realistic loads from everyday operation. The obtained results are discussed in terms of their accuracy, the limitations are evaluated, and the feasibility of application of the TOF approach for SOC estimation is evaluated.

II. TIME-OF-FLIGHT MEASUREMENT ON LIB

The TOF method is well known in other applications but requires adaptation to be usable for LIB state estimation. This section first provides the theoretical background on the mechanical composition and behaviour of LIB pouch cells regarding TOF measurement and then presents a practical approach to implementing the method in a BMS.

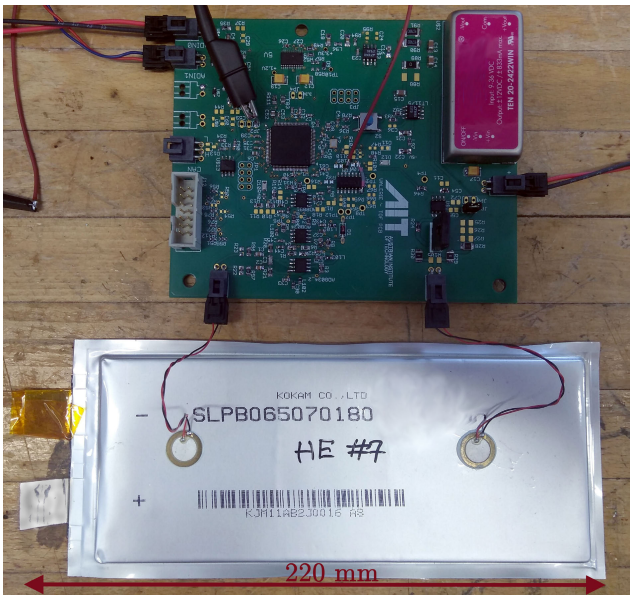

FIGURE 1. Developed PCB and cell connected to piezo transducer discs placed on pouch cell.

A. THEORETICAL BACKGROUND

During battery operation, the lithiation level of the anode, representative of SOC, has a significant impact on cell behaviour, ageing, and cyclability. Because of the complex physico-chemical nature of the lithium-ion battery, identifying the internal changes that lead to battery degradation and failure is challenging, but as a feature of interest extracted from a non-destructive ultrasonic response signal, TOF could be used for analysing battery performance, which leads to changes in both mechanical impedance and ultrasonic velocity [9], [14], [15]. The lithium concentration affects the Young's modulus and the density of the graphite electrode [16]. This influences the ultrasonic wave propagation speed, the latter being indirectly dependent on the SOC. For example, a high lithium concentration in the electrode alters the Young's modulus and therefore causes a higher wave propagation velocity.

For the measurement an emitter and a receiver, in this case piezo discs, are placed on the cell under test at a known distance from each other (Fig. 1). The emitter sends an ultrasonic signal burst that propagates through the battery cell and is detected by the receiver. The time between emitting and receiving the signal is measured as TOF. The battery cell consists of thin layers of anode, cathode, separator and, current collector materials. As the thickness of these layers is smaller than the wavelength of the propagating waves, the waves are considered to behave as Lamb waves. Lamb waves are guided waves in thin plates and can propagate over long distances with little attenuation. Lamb waves are dispersive, enabling the determination of elastic properties and the thickness of the plate [17].

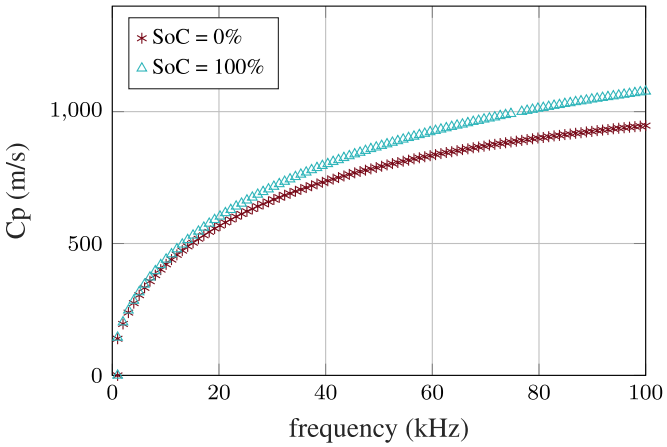

FIGURE 2. Calculated velocities of an empty and a fully charged LIB cell.

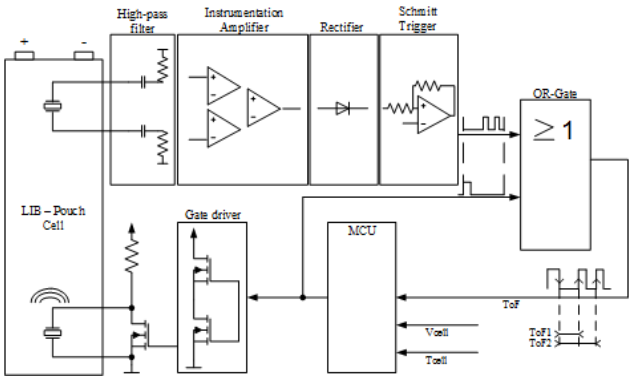

FIGURE 3. Functional diagram of TOF setup and implementation.

A calculation of the wave velocities for different frequencies can be found in Fig. 2. The formula for this calculation is in the appendix. It was found that frequencies above 20 kHz show significant differences between a fully charged and a fully discharged cell. The greater the difference in velocity, the greater the difference in TOF, permitting a less complex, or more accurate, measuring system. In addition, lower frequencies also have lower demands on excitation and measurement. Thus, frequencies in the region between 25 kHz and 40 kHz were chosen for this study. As the sensors were placed 10 cm from each other, the TOF of the signal at e.g. 25 kHz was expected to be between 161 μ s for a fully discharged and 150 μ s for a fully charged cell.

B. IMPLEMENTATION FOR A BMS

Ladpli *et al.* [9], [10] and Gold *et al.* [2] showed that changes in LIB can be detected both by the variation in the amplitude at the receiver and by the TOF through the cell. Because of a reduced sampling rate and less effort for signal processing, TOF measurement makes lower demands on the hardware than processing the variation in amplitude. As cost plays a major role in the field of battery applications [1] this work focuses on the implementation of a low-cost TOF approach that could be used in a BMS. Piezo transducers are utilized both as actuator and sensor. Both are commercial piezo discs from PUI Audio (Dayton, OH, USA) type AB1290B-LW100-R with a resonance frequency of 9 kHz and a capacitance of 8 nF. They are directly attached on the longitudinal axis of the cell, each 5 cm away from the centre and fixed in position with epoxy glue (Fig. 1).

Fig. 3 shows the block diagram of the ultrasonic sensing system. The main components are the two piezo discs, the microcontroller, the transmitter circuit, and the receiver circuit. The receiver circuit consists of a high pass filter with a cut-off frequency of 3.3 kHz. This filter reduces low frequency noise, which can occur from mechanical vibrations in the environment. The filtered signal is amplified by an instrumentation amplifier with a gain factor of 201. The rectifier, which consists of a simple single diode, cuts off the negative voltage of the amplified signal. The rectified signal is fed into a Schmitt-trigger which generates a pulse when the signal is greater than 2 V. The transmitter circuit consists of a MOSFET operated as semiconductor switch, with an additional pull-up resistor connected to +12 V. The measurement starts when the microcontroller generates a square-wave pulse with an adjustable frequency between 20 - 50 kHz. After 50 - 200 μs, depending on the condition of the cell, the microcontroller receives two or more pulses which are generated by the receiver circuit. The microcontroller measures the time between the first falling edge and the second or third rising edge, if any. The first falling edge is the reference pulse which was generated from the microcontroller. This type of setup only requires the use of one general input and output (GPIO) of the microcontroller to generate the pulse for the transmitter circuit, and one enhanced capture module (eCAP) to measure the time elapsed between the triggers generated by the receiving circuit. It has a clock of 100 MHz, leading to a sampling time of 10 ns. This could also be done by combining a fast GPIO or analogue digital converter (ADC) with a timer module if the microcontroller does not have this feature.

The influence on processor load is very low, so the already existing microcontroller of a BMS can be used to perform this task, further driving down the cost of the TOF application. So, in total only some very low-cost components like common operational amplifiers, electronic switches, and passive components are needed to realize the TOF circuit, reducing cost down to the single-digit Euro range, even before considering economies of scale.

The evolution of SOC impacts the overall mechanical impedance of the cell. Thus, not only the TOF shifts, but also the waveform of the signal itself as well. For some cases at the boundary regions of the system, the Schmitt-trigger level could be too low or too high; this generates different trigger sequences. Therefore, the execution of an algorithm that sorts out the pulses and utilizes the correct one is required. The description of the functionality of such an

algorithm is presented as pseudo-code in the supplementary materials.

III. EXPERIMENTAL

This study used commercially available high energy pouch cells from Kokam Company, Ltd. (Gyeonggi-Do, Republic of Korea) type SLPB065070180 [18] with a capacity of 12 Ah and an energy density of 260 Wh/kg (Fig. 1). The cell is composed of a Nickel-Manganese-Cobalt cathode and a graphite anode, representing two commonly used active materials in state-of-the-art Lithium-Ion technology.

Before the actual test the cells were cycled 5 times with a current of 0.5 times the rate of the nominal current (C-rate) between the upper and the lower voltage limit, all according to the manufacturer instructions. Evaluating the TOF approach, under conditions of real-world applications requires tweaking of parameters to which a battery cell's mechanical properties are most sensitive. Despite cycling and storage history, which is negligible in our case of fresh cells, these parameters are temperature [11] and current rates [19]. To estimate the temperature dependency of the TOF approach the arbitrary cell was set at SOC 50 % and subjected to three temperature cycles between 5 and 45°C while the TOF was monitored constantly. Temperature was elevated by 10°C per hour. To estimate the current dependency the cell current on both charge and discharge was set to 0.1, 0.5 and 1 C-rate of the cell under test. Additionally, the cell was discharged with WLTP cycles [13] from SOC 95% until the lower voltage limit was reached. Each cycle lasted 1800 s. The profile was downscaled to cell level and consumed 1.38 Ah of charge, with peak current during the highest discharge pulse set to 18.53 A.

A controlled ambient temperature was secured as all the tests were performed in a calibrated climatic chamber. Temperature was monitored by an in-house developed cell test unit (CTU) via a K-type thermocouple taped onto the upper segment of the cell together with insulation material for decoupling the thermocouple from the ambient temperature. The CTU was also responsible for controlling the cell current and voltage. The channel was calibrated with an accuracy of 0.2 % for the current and 0.1 % for the voltage, both for measured value. Synchronization of the measured TOF by the BMS board (see sec. II) with values obtained by the CTU was done via controller area network (CAN) serial bus protocol; all values were incorporated into the CTU data log file.

All the TOF signals in the following graphs are filtered with a median filter over 100 samples in order to suppress measurement noise.

IV. RESULTS AND DISCUSSION

In Fig. 4 (a) the square wave input signal and the measured and amplified system response of the battery are shown. Both values were measured using an oscilloscope; for normal operation, only the pulses are analysed by the

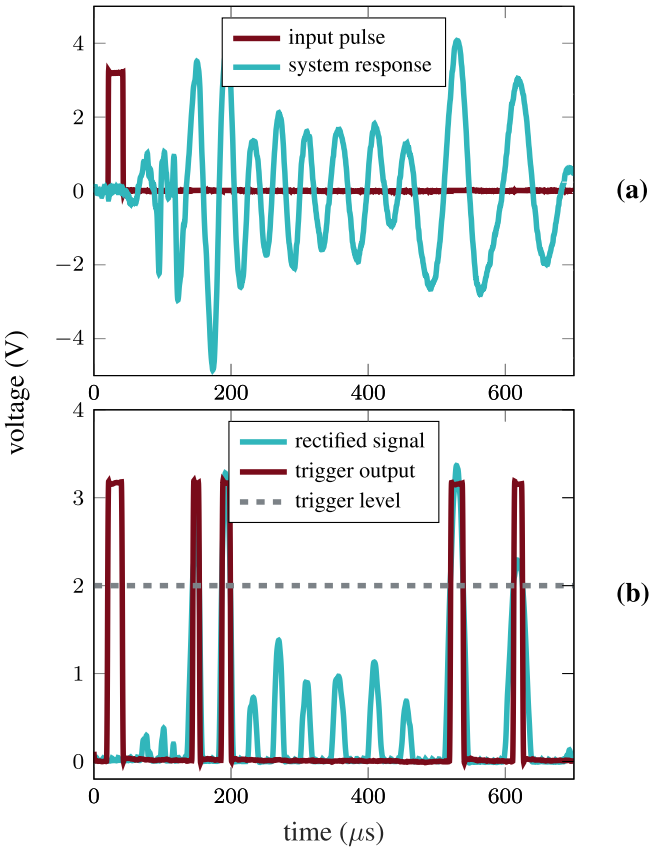

FIGURE 4. Input pulse and system response (a), rectified signal for Schmitt-trigger and trigger output (b).

system. It can be seen that the mechanical excitation via a rectangular pulse leads to a pronounced non-harmonic wave motion of the system with an initial noisy peak after 72 μ s with pronounced half waves starting around 140 μ s, which is in agreement with the values estimated in sec II. To cancel the initial noise, the trigger level needs to be set accordingly.

Fig. 4 (b) depicts the post-processing of the measurement. The amplified signal is rectified by a single diode rectifier so that the subsequent circuitry only needs to process positive signals (see also Fig. 3). The Schmitt-trigger then has a trigger level of 2 V and has a rectangle signal on the output if the value is higher. In the case shown here this is true for two initial pulses and also for the pulses along the signal. The pulses are received on the eCAP input of the microcontroller. This is a capture and counter module. It triggers the first positive edge and then counts the time until the next rising edge is detected. The microcontroller software considers the first two response pulses as relevant and discards the others. Those two pulses are traced and taken for calculation over the entire SOC since the time between the trigger and the edges of the signal represents the TOF and will change over SOC (see also Fig. 3).

The progress of the TOF for a full cycle and different sampling frequencies with a current of 0.5 C-rate is given in Fig. 5, where a correlation of the TOF with

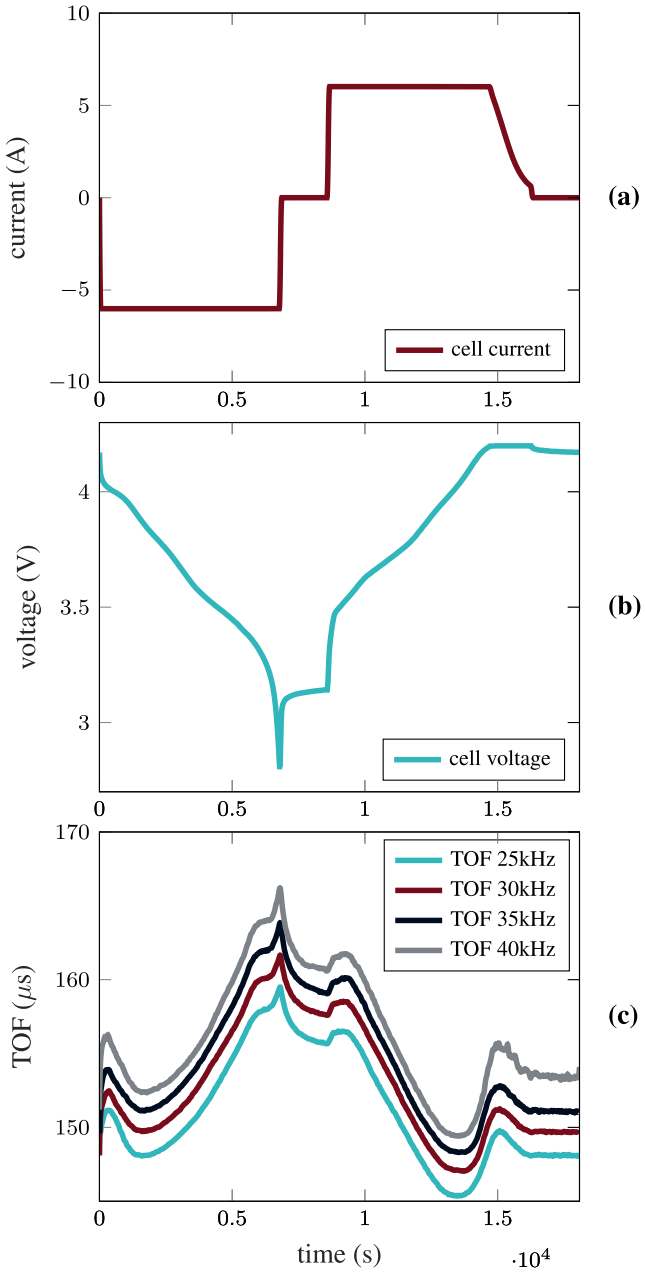

FIGURE 5. Full cycle with voltage (a), current (b) and TOF for several frequencies (c).

the SOC is obvious. As expected (see sec. II), and observed with different approaches in other publications [2], [9], [10], in general the TOF decreases as the SOC increases. Higher frequencies lead to a higher overall TOF, but the progress of the slope over the cycle is similar. Longer TOF also means higher damping of the signal. This is why the TOF at 40 kHz already shows higher distortion in the low SOC region - not all pulses can be detected. However, higher frequencies also could be measured, if necessary, by adapting the parameters of the electronics. The piezo discs chosen for this work have higher attenuation at higher frequencies. Therefore, for the subsequent measurements described in the manuscript a frequency of 30 kHz was chosen.

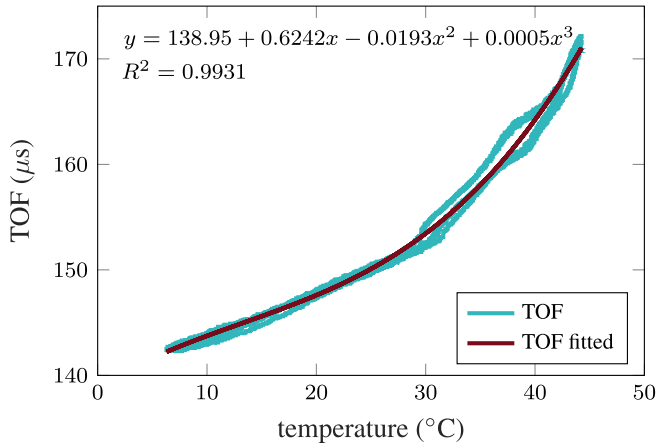

FIGURE 6. Temperature dependency of TOF for the cell at SOC 50 %.

During idle phases the TOF shows a relaxation similar to the one of the cell voltage; thus, after a constant voltage phase during charging the relaxation behaviour is less pronounced compared to the one after constant current discharge. When cell current is applied again, both in the charged and discharged states, the initial peak in TOF is observed again. Bauer *et al.* [20] also observed such behaviour for dilation and attributed it to Lithium staging related phenomena.

Tests on half cells, done separately for anode and cathode of the cells under investigation, have shown that it is most likely local responses resulting from different lithiation stages in the graphite anode [21] that lead to different mechanical properties over the SOC, and thus proves the tendency of an increasing TOF with reducing the SOC. With other cells or other operational parameters also unique TOF to SOC correlations can be observed [2], [12], making the method quite plausible for a BMS application.

In Fig. 6, the dependency of TOF on temperature is depicted. One can see that the TOF declines proportionally to the temperature decrease. This is explained by the higher stiffness of the battery at lower temperatures and thus a higher propagation speed of the wave. The difference between the lowest and the highest TOF is 30 μ s, which is 20 % of the value measured at 25°C. The hysteresis observed in the TOF is related to the temperature level to which the cell was heated or cooled down. This temperature dependency is especially relevant for a real BMS application as batteries in mobile or outdoor stationary applications would endure wide variations in temperature. The slope of the temperature for a BMS can be represented by a 3rd degree polynomial function, also given in Fig. 6. The goodness of the fit is $R^2 = 0.9931$, with a maximum deviation of 2.41 μ s or 1.49 % of measured value at 161.6 μ s. So, a simple compensation of variations in TOF by temperature can be implemented in the BMS when cell temperature is monitored.

Additional uncertainties arise from TOF response as a result of different C-rates. According to Fig. 7, which shows

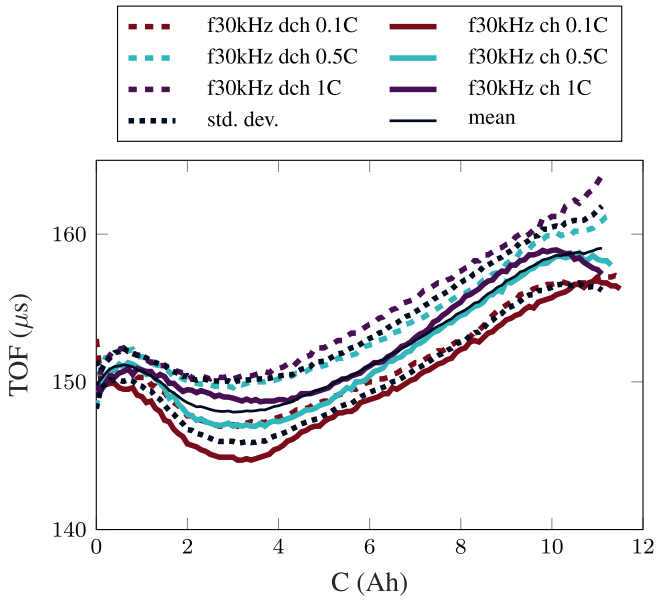

FIGURE 7. TOF for charge and discharge with different C-rates over transferred charge.

the TOF over charge for different profiles with a sample frequency of 30 kHz, higher C-rates lead to longer TOF. Very low C-rates lead to more pronounced local minima at low SOC. Different mechanical behaviour for different C-rates was also observed by Grimsmann *et al.* [19] for dilation. Higher C-rates lead to thinner layers, or indeed thinner cells. The authors attribute this behaviour to inhomogeneous lithium distribution within the electrodes or the particles themselves. This also is believed to influence the TOF as measured here.

Fig. 7 also provides the mean value and the standard deviation calculated for all charge and discharge curves. The highest deviations are observed in higher SOC regions with the maximum of 2.85 μ s from 159.05 μ s at 11.1 Ah, which is an error of 1.79 %. Greater deviations arise from the not clearly determined signal over the SOC. Taking for example the mean value, the peak value of 151.15 μ s at 0.6 Ah can also be found on the curve at 6.1 Ah, which is more than 10 times the SOC value. This means that a BMS with TOF-based state estimation also needs an additional functionality for detection of the position on the curve. Coupling with voltage measurement for a single estimation of a battery in an unknown state or a Kalman filter would be a solution for running operation. A single standalone TOF measurement is not suited for estimation of the SOC in case of the cell under test. This is expected to be different with other types of cells based on the findings regarding TOF progress in other studies [2], [12].

In Fig. 8, the TOF response to consecutive WLTP cycles is shown. To reflect operation in a battery electric vehicle, the cycle starts at a SOC at 95 % and the battery is then exhausted by applying WLTP cycles, each consuming 1.38 Ah. The mean value calculated from the measurements as in Fig. 7 is corrected for the measured cell temperature

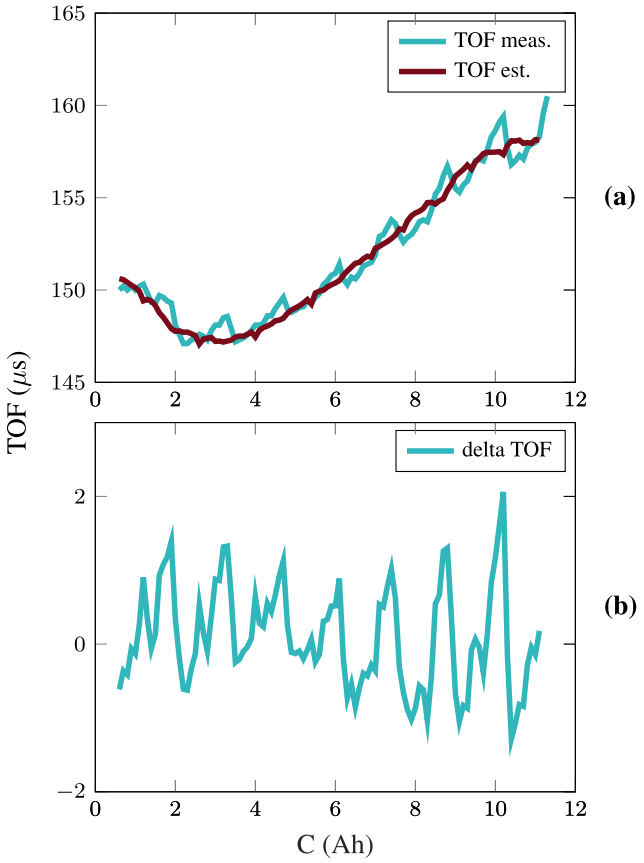

FIGURE 8. TOF measured under driving cycle and estimated TOF (a) and deviation between measured and estimated TOF (b).

during the cycles, with the approach from Fig. 6 serving as an estimator for the TOF to SOC relationship. It can be seen that even during cycles, with such fluctuations between C-rates and charge and discharge, the trend of the TOF is similar to that in constant cycles and the corrected mean value serves as an estimator, producing a maximum error of 2.06 μ s which is an error of 1.29 % of the measured value, or 16.85 % of the total change in TOF, that corresponds to the SOC in the test case. Note that an advanced algorithm like the one described above is necessary to achieve this result.

While the general trend of the SOC over the WLTP is followed by the TOF curve, there are repeating peaks in the real SOC which are not reflected in the TOF curve. These peaks result from the phase with higher power, including peak C-rates of 1.54 C at the end of the WLTP cycle. As shown above, higher C-rates lead to larger changes in the mechanical behaviour of the cell. As the estimator is produced by fitting of mean values, it does not reflect such high peaks. However, after less power intensive sections of the cycle the error is compensated for.

V. CONCLUSION

This work confirmed the correlation between SOC and TOF, using a method that does not require complex laboratory equipment and can be directly implemented into a BMS at

low additional cost. For the first time the approach was validated in real application scenarios for various temperatures, C-rates, and a driving cycle that represents variations in operational parameters comparable to a real application. From the results obtained during this investigation, one should conclude that some variables, like the temperature, have a significant impact on TOF; as there is a change of 30 μs for change in temperature from 5 to 45°C, while for example at 25°C the total variation in TOF between fully charged and discharged cell is 10 μs. Thus, knowledge of the current cell temperature and compensation for it are necessary. While this can be implemented with low effort, the errors caused by non-straightforward dependency of the TOF on the SOC found for the investigated cell, and by the uncertainties stemming from the C-Rate makes the approach less reliable for SOC determination. However, advanced processing of the data, like Kalman filtering or such, would highly improve data usability. Another possible field of application is the surveillance of the mechanical stability of the cell in the pack, which becomes especially interesting after a crash or other mechanical stress.

APPENDIX

As stated above, a LIB consists of multiple different layers. The connection between the layers can be mathematically represented by using the Global Matrix [17], [22], [23].

$$G = \begin{bmatrix} D_{1hb} & D_{2t} & & & & \\ & D_{2b} & D_{3t} & & & \\ & & D_{3b} & \cdots & & \\ & & & \cdots & D_{(n-1)t} & \\ & & & & D_{(n-1)b} & D_{nht} \end{bmatrix} \tag{1}$$

Doing this, each layer again is represented by a Top

$$D_t = \begin{bmatrix} -k & -k \\ -\sqrt{\frac{\omega^2}{c_l^2}-k^2} & \sqrt{\frac{\omega^2}{c_l^2}-k^2} \\ -i\rho(\omega^2-c_s^2k^2) & -i\rho(\omega^2-c_s^2k^2) \\ -i\rho c_s^2 k\sqrt{\frac{\omega^2}{c_l^2}-k^2} & i\rho c_s^2 k\sqrt{\frac{\omega^2}{c_l^2}-k^2} \\ -\sqrt{\frac{\omega^2}{c_s^2}-k^2} & \sqrt{\frac{\omega^2}{c_s^2}-k^2} \\ k & k \\ i\rho c_s^2 k\sqrt{\frac{\omega^2}{c_s^2}-k^2} & -i\rho c_s^2 k\sqrt{\frac{\omega^2}{c_s^2}-k^2} \\ -i\rho(\omega^2-c_s^2k^2) & -i\rho(\omega^2-c_s^2k^2) \end{bmatrix} \tag{2}$$

and a Bottom Matrix,

$$D_b = \begin{bmatrix} ke^{id\sqrt{\frac{\omega^2}{c_l^2}-k^2}} & \frac{k}{e^{id\sqrt{\frac{\omega^2}{c_l^2}-k^2}}} \\ \frac{\sqrt{\frac{\omega^2}{c_l^2}-k^2}}{e^{-id\sqrt{\frac{\omega^2}{c_l^2}-k^2}}} & -\frac{\sqrt{\frac{\omega^2}{c_l^2}-k^2}}{e^{id\sqrt{\frac{\omega^2}{c_l^2}-k^2}}} \\ \frac{i\rho(\omega^2-c_s^2k^2)}{e^{-id\sqrt{\frac{\omega^2}{c_l^2}-k^2}}} & \frac{i\rho(\omega^2-c_s^2k^2)}{e^{id\sqrt{\frac{\omega^2}{c_l^2}-k^2}}} \\ \frac{-2i\rho kc_s\sqrt{\frac{\omega^2}{c_l^2}-k^2}}{e^{-id\sqrt{\frac{\omega^2}{c_l^2}-k^2}}} & -\frac{-2i\rho kc_s\sqrt{\frac{\omega^2}{c_l^2}-k^2}}{e^{id\sqrt{\frac{\omega^2}{c_l^2}-k^2}}} \\ \frac{\sqrt{\frac{\omega^2}{c_s^2}-k^2}}{e^{-id\sqrt{\frac{\omega^2}{c_s^2}-k^2}}} & -\frac{\sqrt{\frac{\omega^2}{c_s^2}-k^2}}{e^{id\sqrt{\frac{\omega^2}{c_s^2}-k^2}}} \\ -ke^{id\sqrt{\frac{\omega^2}{c_s^2}-k^2}} & -\frac{k}{e^{id\sqrt{\frac{\omega^2}{c_s^2}-k^2}}} \\ -\frac{-2i\rho kc_s\sqrt{\frac{\omega^2}{c_s^2}-k^2}}{e^{-id\sqrt{\frac{\omega^2}{c_s^2}-k^2}}} & \frac{-2i\rho kc_s\sqrt{\frac{\omega^2}{c_s^2}-k^2}}{e^{id\sqrt{\frac{\omega^2}{c_s^2}-k^2}}} \\ \frac{i\rho(\omega^2-c_s^2k^2)}{e^{-id\sqrt{\frac{\omega^2}{c_s^2}-k^2}}} & \frac{i\rho(\omega^2-c_s^2k^2)}{e^{id\sqrt{\frac{\omega^2}{c_s^2}-k^2}}} \end{bmatrix} \tag{3}$$

where k is the wave number, ω the angular frequency, c_l the longitudinal wave velocity, c_s the shear wave velocity, ρ the density, and d the thickness of each layer.

To determine the propagation speed of the ultrasonic vibration wave, the determinant of the Global Matrix G has to be found. As G is dependent on the sub-matrices D_t and D_b the factors of these two matrices play a crucial role. The factors c_l and c_s represent the longitudinal and shear velocities of the propagating waves. These velocities are dependent on the Young's modulus. In this context, the wave propagation velocity is dependent on the Young's modulus and therefore connected to the SOC.

To determine the parameters for the calculation above, a cell was dismantled and its physical properties determined by post mortem analysis. For details see [21].

ACKNOWLEDGMENT

The authors want to express their appreciation to Dr. I. Gocheva, Dr. M. Jahn, and Mr. D. Dvorak for the scientific discussions and their comments on earlier versions of the manuscript, and to Mrs. J. Winter and Mr. B. Ganev for correction and polishing of the language.

REFERENCES

[1] M. A. Hannan, M. M. Hoque, A. Hussain, Y. Yusof, and P. J. Ker, "State-of-the-art and energy management system of lithium-ion batteries in electric vehicle applications: Issues and recommendations," *IEEE Access*, vol. 6, pp. 19362–19378, 2018.

[2] L. Gold, T. Bach, W. Virsik, A. Schmitt, J. Mueller, T. E. Staab, and G. Sextl, "Probing lithium-ion batteries' state-of-charge using ultrasonic transmission—Concept and laboratory testing," *J. Power Sources*, vol. 343, pp. 536–544, Mar. 2017. [Online]. Available: http://www.sciencedirect.com/science/article/pii/S0378775317301003

[3] R. Xiong, J. Cao, Q. Yu, H. He, and F. Sun, "Critical review on the battery state of charge estimation methods for electric vehicles," *IEEE Access*, vol. 6, pp. 1832–1843, 2018.

[4] V. A. Sethuraman, L. J. Hardwick, V. Srinivasan, and R. Kostecki, "Surface structural disordering in graphite upon lithium intercalation/deintercalation," *J. Power Sources*, vol. 195, no. 11, pp. 3655–3660, Jun. 2010. [Online]. Available: http://www.sciencedirect.com/science/article/pii/S0378775309022964

[5] D. Schneider, "Silicon anodes will give lithiumion batteries a boost," *IEEE Spectr.*, vol. 56, no. 1, pp. 48–49, Jan. 2019.

[6] J. H. Lee, H. M. Lee, and S. Ahn, "Battery dimensional changes occurring during charge/discharge cycles—Thin rectangular lithium ion and polymer cells," *J. Power Sources*, vols. 119–121, pp. 833–837, Jun. 2003. [Online]. Available: http://www.sciencedirect.com/science/article/pii/S0378775303002817

[7] X. Wang, Y. Sone, and S. Kuwajima, "*In situ* investigation of the volume change in li-ion cell with charging and discharging satellite power applications," *J. Electrochem. Soc.*, vol. 151, no. 2, pp. A273–A280, Jan. 2004. [Online]. Available: http://jes.ecsdl.org/content/151/2/A273.abstract

[8] A. G. Hsieh, S. Bhadra, B. J. Hertzberg, P. J. Gjeltema, A. Goy, J. W. Fleischer, and D. A. Steingart, "Electrochemical-acoustic time of flight: In operando correlation of physical dynamics with battery charge and health," *Energy Environ. Sci.*, vol. 8, pp. 1569–1577, Mar. 2015. [Online]. Available: http://dx.doi.org/10.1039/C5EE00111K

[9] P. Ladpli, F. Kopsaftopoulos, and F.-K. Chang, "Estimating state of charge and health of lithium-ion batteries with guided waves using built-in piezoelectric sensors/actuators," *J. Power Sources*, vol. 384, pp. 342–354, Apr. 2018. [Online]. Available: http://www.sciencedirect.com/science/article/pii/S0378775318301770

[10] P. Ladpli, C. Liu, F. Kopsaftopoulos, and F.-K. Chang, "Estimating lithium-ion battery state of charge and health with ultrasonic guided waves using an efficient matching pursuit technique," in *Proc. IEEE Transp. Electrific. Conf. Expo, Asia–Pacific (ITEC Asia–Pacific)*, Jun. 2018, pp. 1–5.

[11] H. Popp, G. Glanz, K. Alten, I. Gocheva, W. Berghold, and A. Bergmann, "Mechanical frequency response analysis of lithium-ion batteries to disclose operational parameters," *Energies*, vol. 11, no. 3, p. 541, Mar. 2018. [Online]. Available: http://www.mdpi.com/1996-1073/11/3/541

[12] P. Ladpli and F.-K. Chang, "Battery state monitoring using ultrasonic guided waves," U.S. Patent WO 2017 223 219 A1, Jun. 21, 2017.

[13] UNECE - United Nations Economic Commission for Europe. 2017. *WLTP—Worldwide Harmonized Light-Duty Vehicles Test Procedure*. [Online]. Available: www.unece.org/fileadmin/DAM/trans/doc/2012/wp29grpe/WLTP-DHC-12-07e.xls

[14] C. Yang. (2017). *Distributed Piezoelectric Transducers and Their Applications in Structural Health Monitoring*. [Online]. Available: http://dokumentix.ub.uni-siegen.de/opus/volltexte/2017/1101

[15] J. Noël and G. Kerschen, "Nonlinear system identification in structural dynamics: 10 more years of progress," *Mech. Syst. Signal Process.*, vol. 83, pp. 2–35, Jan. 2017. [Online]. Available: http://www.sciencedirect.com/science/article/pii/S088832701630245X

[16] K. R. Kganyago and P. E. Ngoepe, "Structural and electronic properties of lithium intercalated graphite LiC_6," *Phys. Rev. B, Condens. Matter*, vol. 68, Nov. 2003, Art. no. 205111. [Online]. Available: https://link.aps.org/doi/10.1103/PhysRevB.68.205111

[17] R. Lammering, U. Gabbert, M. Sinapius, T. Schuster, and P. E. Wierach, *Lamb-Wave Based Structural Health Monitor. Polymer Composites*. Luxemburg, Germany: Springer, 2018.

[18] *Superior Lithium Polymer Battery (SLPB) Cell Specification*, Kokam Company, Suwon, South Korea, 2017.

[19] F. Grimsmann, F. Brauchle, T. Gerbert, A. Gruhle, M. Knipper, and J. Parisi, "Hysteresis and current dependence of the thickness change of lithium-ion cells with graphite anode," *J. Energy Storage*, vol. 12, pp. 132–137, Aug. 2017. [Online]. Available: http://www.sciencedirect.com/science/article/pii/S2352152X1730097X

[20] M. Bauer, M. Wachtler, and H. Stöwe, J. V. Persson, and M. A. Danzer, "Understanding the dilation and dilation relaxation behavior of graphite-based lithium-ion cells," *J. Power Sources*, vol. 317, pp. 93–102, Jun. 2016. [Online]. Available: http://www.sciencedirect.com/science/article/pii/S0378775316302932

[21] M. Luthfi, "State estimation of lithium ion battery using non-invasive method," M.S. thesis, Carinthia Univ. Appl. Sci., Villach, Austria, 2018.

[22] M. J. S. Lowe, "Matrix techniques for modeling ultrasonic waves in multilayered media," *IEEE Trans. Ultrason., Ferroelectr., Freq. Control*, vol. 42, no. 4, pp. 525–542, Jul. 1995.

[23] A. Demčenko and Mažeika, "Calculation of Lamb waves dispersion curves in multilayered planar structures," *Ultragarsas*, vol. 44, no. 3, pp. 15–17, 2002.

HARTMUT POPP (S'18) received the M.Sc. degree in industrial electronics from FH Technikum Vienna, Austria, and in environment and bioresources management from the BOKU University Vienna, Austria, respectively. He is currently pursuing the Ph.D. degree with the Institute of Electronic Sensor Systems, Technical University Graz, Austria. After working as a Design Engineer at Siemens AG, he joined the AIT Austrian Institute of Technology. His research interests include testing, modelling, and diagnostics of Lithium-Ion batteries. He is a Student Member of IEC/OVE TC21 Working Group.

MARKUS KOLLER received the M.Sc. degree in embedded systems from the University of Applied Science Technikum Vienna, in 2015. Since then, he has been working as a Researcher with the Center for Low-Emission Transport, AIT Austrian Institute of Technology. His field of work includes the development of battery management systems, the software development of active and passive balancing algorithms, and commissioning of battery management systems hardware.

SEVERIN KELLER is currently pursuing the bachelor's degree in mechanical engineering with Hochschule Augsburg. He performed a Practical Semester at the TU Graz Institute of Electronic Sensor Systems. His research interests, concerning his bachelor thesis, include testing and modelling diagnostic systems for Lithium-Ion batteries.

GREGOR GLANZ is currently pursuing the bachelor's degree in mechanical engineering – economics with the Technical University of Vienna. He joined the AIT Austrian Institute of Technology, in 2017, as a Working Student. His field of work and research interests include the mechanical properties and testing of Lithium-Ion batteries.

REINHARD KLAMBAUER received the master's degree in electrical engineering from the University of Technology in Graz, Austria, in 2014. His master thesis was part of the international research project A3 Falcon with the topic spatially resolved impedance spectroscopy in a PEM fuel cell. He worked as a University Project Assistant on various industry projects focusing on embedded systems. Since 2016, he has been employed as a University Assistant with the Institute of Electronic Sensor Systems. He is currently working on his Ph.D. thesis with the preliminary title Ultrasonic in Reactive Flows.

ALEXANDER BERGMANN received the Ph.D. degree in physics from Karl Franzens University, Graz, Austria, in 2000. From 2001 to 2016, he worked in different industrial Research and Development positions in the field of sensors and sensor systems. Since 2016, he has been a Professor and the Head of the Institute of Electronic Sensor Systems, Faculty of Electrical and Information Engineering, Graz University of Technology, Graz. He has coauthored two books, more than 65 articles, and filed more than 20 patents. His main research areas include modelling, simulation and design of electronic sensor systems, aerosol sensors and ambient air sensors, photo- and thermoacoustic sensors, sound, ultrasound and vibration sensors, distributed, multimodel sensors and sensor networks, highly integrated sensors, and sensor systems.

Appendix D

Paper 3: 'Mechanical Methods for State Determination of Lithium-Ion Secondary Batteries: A Review'

Journal of Energy Storage 32 (2020) 101859

Contents lists available at ScienceDirect

Journal of Energy Storage

journal homepage: www.elsevier.com/locate/est

Mechanical methods for state determination of Lithium-Ion secondary batteries: A review

Hartmut Popp[*,a,b], Markus Koller[a,b], Marcus Jahn[a], Alexander Bergmann[b]

[a] AIT, Austrian Institute of Technology GmbH, Center for Low-Emission Transport, Giefinggasse 2, Vienna 1210, Austria
[b] Graz University of Technology, Institute of Electrical Measurement and Sensor Systems, Inffeldgasse 10/II, Graz 8010, Austria

ARTICLE INFO

Keywords:
Lithium-Ion secondary battery
Non-destructive testing
Mechanical properties
State estimation
Battery management system
In-operando methods

ABSTRACT

Lithium-Ion batteries are the key technology to power mobile devices, all types of electric vehicles, and for use in stationary energy storage. Much attention has been paid in research to improve the performance of active materials for Lithium-Ion batteries, however, for optimal, long and safe operation, detailed knowledge of -among others- the state-of-charge and the state-of-health of the battery is paramount both in laboratory use, as well as during application by the battery management system. Today's systems often derive their estimators from data of the voltage, current and temperature measurements, which can lead to inaccurate estimations of values during operation. Mechanical based measurements became very popular recently to fill the gap in data by complementing conventional measurements and thus provide more accurate information about the internal state of Lithium-Ion batteries. This review aims to present the current state of this promising topic for both laboratory use and applications on non-destructive in-situ and in-operando methods for measurement of mechanical battery parameters like expansion, strain and force, experimental modal analysis, ultrasonic probing and acoustic emission technologies. The intention of this summary is to provide insights in this emerging topic by showing benefits, drawbacks, possibilities and applications of each technique and compare those to each other, thus providing the readers with a deep insight into the topic.

1. Introduction

Lithium-Ion secondary batteries (LIB) have been commercially available since their introduction by Sony in the year 1991. Due to continuous improvements, they have successfully conquered the market [1,2]. While in the early stage they were used as one alternative among several battery chemistries to power mobile devices, later, due to their high energy density and their longer lifetime compared to other electrochemical energy storage systems, LIB became the chemistry of choice for many different applications. Nowadays, they are indispensable components of mobile and consumer devices, power tools, and electric vehicles [2,3]. Becoming price-competitive has opened a new area of utilization for LIBs as stationary home storage and to a certain degree even in grid storage applications [4]. By tuning material parameters for active and passive components, and with optimized manufacturing, LIB are expected to further decrease in cost and increase in performance [2,4].

A drawback of LIB is that for proper and safe use, they require constant surveillance to maintain operation in a narrow window of voltage and temperature. This is usually done with a battery management system (BMS). For single cells, the BMS is a relatively simple analogue electrical circuit; for more complex systems with many cells, more complex hardware with micro-controllers and dedicated software is implemented. One of the main tasks of the BMS is the estimation of the state-of-charge (SOC) of the cell. Other state estimations like state-of-health (SOH), state-of-function (SOF) and others (SOX) are also performed. State-of-the-art BMS perform the estimation via the electrical two pole behaviour of the cell, meaning that they measure the cell voltage and / or the cell current, sometimes combined with the cell temperature. From these values, the SOX are derived. Xiong et al. [5], in their review list four main methods for this: i) lookup table, where e.g. the open circuit voltage (OCV) of the cell is compared to OCV reference values for the SOC in a table; ii) ampere-hour integral, where the cell current is measured permanently and the transferred charge is calculated and compared to the cell capacity; iii) model-driven methods, where electrochemical-, equivalent circuit-, and / or impedance models of the cell are stored and the measured values compared with those predicted by the model and iv) data driven, where data training or a data-model fusion method are used to later estimate the SOC. The third method is often improved on by applying advanced

* Corresponding author.
E-mail address: hartmut.popp@ait.ac.at (H. Popp).

https://doi.org/10.1016/j.est.2020.101859
Received 6 August 2020; Received in revised form 3 September 2020; Accepted 4 September 2020

Nomenclature

Abbrevations

AE	Acoustic Emission
Al	Aluminum
BMS	Battery Management System
C	Carbon
CEI	Cathode Electrolyte Interface
CNT	Carbon Nano Tube
CWT	Continuous Wavelet Transformation
C-rates	Current rates
DFT	Density Functional Theory
DPM	Driving-Point Measurement
DUT	Device Under Test
EIS	Electrochemical Impedance Spectroscopy
EMA	Experimental Modal Analysis
EMI	Electro Magnetic Interference
EOL	End Of Life
FBG	Fiber Bragg Grating
FEM	Finite Element Model
FFT	Fast Fourier Transformation
FPGA	Field Programmable Gate Arrays
FRF	Frequency Response Function
GPIO	General Purpose Input / Output
LFP	Lithium-Iron-Phosphate
Li	Lithium
LIB	Lithium-Ion Secondary Battery
LIC	Lithium Capacitor
LMO	Lithium-Manganese-Oxyde
LTI	Linear Time Invariant
LTO	Lithium-Titanate-Oxyde
MDOF	Multi Degree of Freedom
NDE	Non Destructive Evaluation
NMC	Nickel-Manganese-Cobalt
OCV	Open Circuit Voltage
OSI	Optical Sensor Interrogator
P-	Pressure-
PCA	Principal Component Analysis
PCG	Pitch Coated Flaky Graphite
RUL	Remaining Useful Life
S-	Shear-
SDOF	Single Degree of Freedom
SEI	Solid Electrolyte Interface
SHM	Structural Health Monitoring
Si	Silicon
SOC	State-of-Charge
SOF	State-of-Function
SOH	State-of-Health
SOX	State-of-X
STFT	Short-Time Fourier Transformation
TM	Transfer Measurement
TOF	Time-f-Flight
US	Ultra-Sonic
XRD	X-Ray Diffraction

Math. Symbols

a	Acceleration ($m \cdot s^{-2}$)
A	Normalized Amplitude (1)
c	Speed of Propagation ($m \cdot s^{-1}$)
F	Force (N)
Q	Charge ($A \cdot s$)
V	Voltage (V)
λ	Wavelength (m)
ξ	Damping (1)
ω	Frequency (s^{-1})
ρ	Density ($kg \cdot m^{-3}$)

algorithms like Luenberger observer, Kalman- or particle swarm filter and others [5]. These increase accuracy, but they also increase computational load. Waag et al. [6] in 2014 in their review already analysed over 350 publications handling the topic of SOX estimation with these methods, and the numbers have been increasing steadily in the meantime, as can be seen in newer reviews [7,8]. The accuracies achieved are sufficient for normal operation. However, as already stated, all methods rely on electrical- and in some cases additional temperature measurement, so the SOC is measured in an indirect way, as it is derived from electrical behaviour [9].

Another important LIB cell property is that its mechanical values can change during operation (details see Section 2). LIB active materials swell and shrink over the SOC, with a share of non-reversible physical changes in particular, partially reflecting the SOH. Therefore, by measuring the mechanical properties of the LIB cell, one can directly derive SOX values. These values are crucial for battery systems mechanical design to safeguard the cell from swelling forces with enough damper material to absorb the expansion. Insufficient buffer space can lead to serious and dangerous defects as experienced with the Samsung Galaxy Note 7 incidents [10]. On the other hand, an adequate mechanical force on the (pouch) cell, applied as per manufacturer's recommendations, improves both the electrochemical performance and lifetime [11,12] of the LIB cell. Also, constructing a functional, fault tolerant, and safe LIB battery housing requires information about the structural integrity of the cell which determines its ability to sustain mechanical loads during operation, such as vibration of the environment [13–15], and to minimize critical situations when mechanical forces caused for instance by a vehicle accident occur [16]. Parameters containing this information on the mechanical behaviour of the cell cannot be measured by its electrical two pole behaviour.

In order to overcome the lack of data on the mechanical properties, and also to have a second source of SOX parameter values, mechanical measurement methods were developed in recent years. There are four main methods [9] for measurement of the mechanical properties of LIB:

- destructive testing,
- imaging methods,
- expansion based methods, and
- acoustic based methods.

The first one, as the name implies, is destructive, meaning the cell is destroyed or seriously affected in its operational behaviour and safety; the others are classic non-destructive approaches. The third and the fourth have the potential for in-situ and in-operando application, as this work aims to show. In addition, this form of testing can give useful information for potential use in second life applications. Here, the SOH estimation after collection of used LIBs tends to be the most difficult and costly part of the operation.

Destructive mechanical tests, usually involve (heavy) machinery which bend, stretch, or compress single components, cells, modules, or systems of a LIB all the way from reversible (elastic) to a non-reversible (non-elastic) scale [16–23]. With the applied force and the resulting deformation, calculations of the mechanical values of the cell such as strain or Young's modulus are possible. The reviews [16,17] provide deeper insight into this topic and its applications. This method is not practical for analysis without destruction (in-situ) and thus neither for analysis during operation (in-operando) monitoring.

Imaging methods like X-ray or computer tomography provide

insights into the physical structure of the cells or materials and enable measurement of layer thickness through changes in SOC or SOH, and identifying structural defects in materials and in cell components caused e.g. by ongoing ageing. Some methods can be used both in-situ and in-operando. A comprehensive overview on the topic of imaging methods and of the strengths and weaknesses of each technique is given in [24,25]. Even the imaging techniques capable of in-operando work require extensive laboratory equipment, and hence space as well as capital cost, and are therefore normally not suited for use within an application.

As this work focuses on in-situ or in-operando non-destructive mechanical tests, the first two methods are not discussed any further. Readers are referred to the existing literature. The last two methods are based on the non-destructive measurement of the expansion of the material and on the non-destructive measurement of the mechanical properties of the material or cell in question. Both are classical approaches in non-destructive testing [26,27] and are also increasingly applied to the characterization of LIB. A detailed explanation on the underlying phenomena in this context, as well as a review of these methods, has been missing so far. This work aims to fill that gap. Therefore, first the changes in mechanical behaviour of the cell over its operational life investigating reversible changes by cycling and non-reversible changes by ageing and abusive conditions are described. Secondly, the expansion- based and the acoustic- based methods are described more in detail, including their suitability for different cell formats. Third, a discussion on the usefulness for laboratory and real-world applications is given and possible future fields of research are discussed. Fourth, a conclusion on the topic is given.

2. Changes in mechanical behaviour of LIB

The rocking-chair mechanism governs the operation in LIBs (Fig. 1). In brief, the Lithium-Ions (Li^+)stored in host lattices in the electrodes are shuttled by diffusion from the negative electrode to the positive electrode during discharge, undergoing solvation at the negative electrode interface and de-solvation at the positive electrode interface. Upon charge, the Li^+ ions are extracted from the cathode and inserted in the anode. Therefore, in contemporary batteries no lithium metal but lithium containing compounds are used. As a consequence of such a mechanism, sluggish Li^+ kinetics are quiet unavoidable during both charge and discharge. Nonetheless, much progress has been achieved; it should be pointed out that these advancements have largely been applied to conventional LIBs containing transition-metal oxide electrodes, as explained in following paragraphs. In today's LIB cells, there are mostly Lithium-Metal-Oxides and phosphates on the cathode and Graphite on the anode side, whereas newer cells having additions of 4% to 5% of Silicon (Si) in the anode material. For these and for some promising future electrode materials as well, the insertion and removal of Li-ions goes hand in hand with a change in volume arising primarily due to changes in lattice dimensions, changes in crystal structures, and phase transitions. These changes in volume are hindered by the mechanical constraints of the inactive materials like casing or current collectors and thus lead to strain in the materials. This strain results in mechanical instabilities, including plastic deformation, fragmentation, disintegration and fracturing. Such effects are known as a major source of performance fading in LIB cells over their cycle lifetime, and hence are intimately connected to the SOH [28].

In addition to this, both ageing arising from the mechanical volume changes and ageing caused by chemical side reactions take place. The majority of these effects originates from electrolyte decomposition over time (calendar ageing) and the cycles themselves. This decomposition process of the electrolyte is rather delicate, as it leads to production of side-products, but it is initially needed to form the solid electrolyte interface (SEI) layer on the anode which is then slowing down the degradation of electrode and electrolyte by forming a protective layer. Subsequent decomposition reactions can lead to gas evolution and undesired SEI growth which increases internal resistance [8,31]. More information on the topic is found below in this section. Such products further alter the physical properties of the cell and its materials.

Another important factor for the mechanical properties of LIB cells is the casing. In general, there are two popular formats for LIBs, prismatic and cylindrical; while the prismatic ones can be further divided into hard case- and soft case cells, so called pouch cells (Fig. 2). Cylindrical cells have wound bulk / core materials (Fig. 2 (middle)), and so do most of the hard case prismatic cells, while pouch cells mostly have stacked or z-folded bulk / core layers [32]. This internal structure of the cells accounts for different constraints on the material expansion [33]. First there is the core itself. In cylindrical cells, the core, virtue of its mechanical setup, limits the expansion space and thus strain is produced. This is also true for the prismatic cell windings, especially in the turns on the broad side of the cells (Fig. 2 (right)). The stacked structure of pouch cells in itself allows for expansion. The second limiting factor is the battery cell case. Cylindrical cells and prismatic housings, usually have solid cases made of aluminum (Al) or stainless steel, while pouch cells have a soft laminated metal-plastic compound foil. The first is more rigid, limiting expansion, while the second permits more swelling of the material. As the electrodes usually are placed over each other layer by layer, an increase in thickness / strain on the casing is usually assigned to the overall expansion of the cell [34].

The following subsections are a summary of the mechanical changes in frequently applied or promising LIB materials to outline the methods discussed in this work. For a deeper analysis the reader is referred to [28].

2.1. Anode

Graphite is still the most common anode material used in contemporary LIB. It can host one Li-ion per six carbon (C) atoms, leading to a maximum theoretical gravimetric capacity of 372 mAh/g. The expansion of graphite over its lithiation states has been thoroughly investigated. Major contributions to its understanding were made around the time of its commercialization using imaging methods, mainly X-ray diffraction [35,36]. Fig. 3 shows the expansion of unlithiated C to its fully lithiated LiC_6 state. The volume increases up to about 10% with the Li^+ content [28,35,37,38]. Qi et al. [37] investigated other mechanical values, too, and found a threefold change in the Young's modulus for cycling of the graphite anode. This value is obtained by applying density functional theory (DFT) simulations and comparing them with literature values.

Lithium-Titanate (LTO) has a comparably low theoretical gravimetric capacity of 175 mAh/g but it is still a popular anode material when high cycle life and high-power are demanded. It is known as a zero strain material; this means there are no [40,41] or only minimal changes of 0.1% to 0.3% [42] in volume with changing Li^+ content. Si,

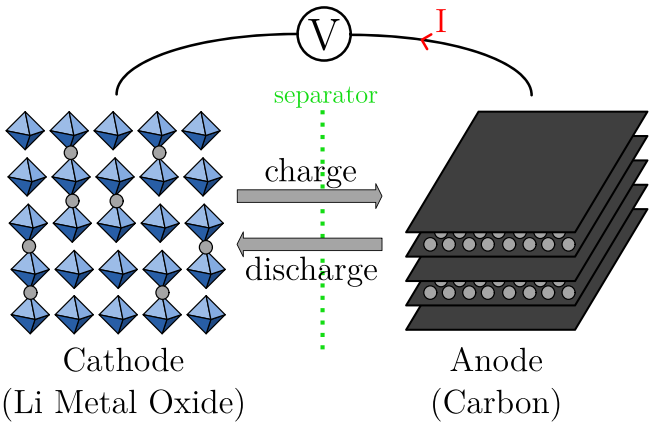

Fig. 1. Working principle of LIB (based on [29,30]).

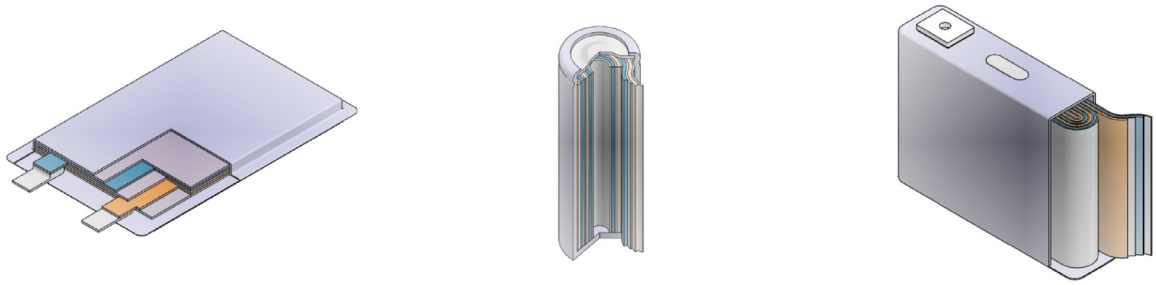

Fig. 2. Sketch of pouch (left), cylindrical (middle) and prismatic cell (right).

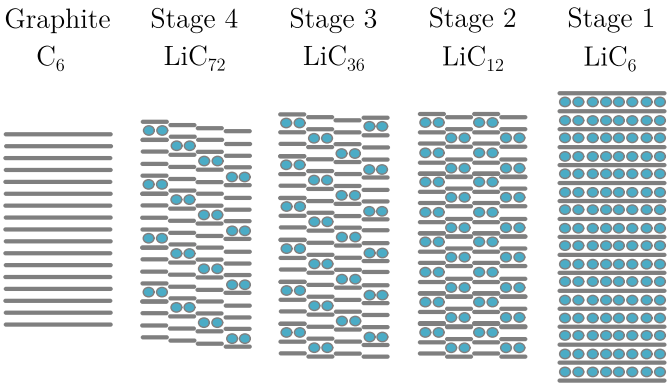

Fig. 3. States of intercalation of Li in graphite (own representation based on [39]).

one of the promising transition metal anode materials, is seen as a candidate for future high capacity LIB systems as it can host 4.4 Li-ions per one Si atom which leads to a theoretical gravimetric capacity of 4200 mAh/g, even above that of metallic Li (3860 mAh/g [1]). The fact that Si intercalates so many Li^+ leads to drastic changes in volume upon lithiation; reports range from 280% [38] to 400% [28]. Currently, the most commonly targeted solution is a Si-C composite with a maximum of 5% to 10% Si content, in order to mitigate its volume expansion.

Other possible materials such as tin are also considered for future applications. Tin has a high theoretical capacity of 993.4 mAh/g and offers low cost and suitable working potentials but tin also shows a great change in volume of about 300% between full and empty lithiation states [43].

In general, one can say that the higher the theoretical capacity of intercalation materials, the higher also the changes in volume. Here, the differences between intercalation and conversion reaction mechanisms play an important role, because conversion or alloying reactions, occurring in transition metal anodes, limit the reaction rate of Li insertion into the material and thus lower the possibly achievable charge and discharge rates. In addition to the material's properties themselves, the morphology of the corresponding electrode needs to be taken into account. The intercalation mechanism of Li into the anode host structure is also limited by the pore size of the electrode, which is reflected in the associated Li diffusion coefficient. This results in a limited charge and discharge capability, especially for high energy electrodes, which tend to have very small pore sizes due to high compaction rates. The resulting limitation in Li diffusion can lead to Li plating on the anode surface, particularly when higher charge rates are chosen. Li plating is mostly irreversible and can lead to safety risks since it facilitates the formation of Li dendrites [44].

2.2. Cathode

Cathode materials, mostly comprised of Li-M-oxides (M = (Nickel (Ni), Manganese (Mn), Cobalt (Co), Iron (Fe) and/or Aluminum (Al))), are the main capacity limiting factor in LIB. Nevertheless, since Li-ions are not intercalated into these compounds, but are rather (de-)inserted into the crystal structure upon cycling, their lattice structure does not change as much as observed for anode materials. Lithium-Nickel-Cobalt-Aluminum (NCA) changes about 4.5% [38] in volume during charge/discharge, while Lithium-Iron-Phosphate (LFP) changes by about 4.7% [45]. For the cathode material Lithium-Nickel-Manganese-Cobalt-Oxide (NMC) the data vary significantly. Sauerteig et al. [40] in their study, analysed six different studies and found values from -3.4% to 2.4% for de-lithiation. Their own study found an increase of 0.8% upon de-lithiation. It should however, be noted that due to the (de-) insertion of Li ions into and from the crystal lattice, there is a maximum of Li that can be removed before the lattice structure collapses. For most Li metal oxides, this maximum can be found between 40% to 60% of the total Li amount. This accounts for the fact that all cathode materials have a commensurately higher theoretical capacity than that which is practically and reversibly achievable.

2.3. Other relevant phenomena

Phenomena which take place at interfaces or are common for both the positive and the negative electrode are explained in the next subsections.

2.3.1. Solid electrolyte interface and gas evolution

A crucial and very complex phenomenon is the formation and subsequent evolution of the SEI layer, especially on the anode side of the battery. The SEI layer is an interface layer that consists of decomposition products of the electrolyte on the negative electrode surface [46]. The formation of a cell is a decisive factor in the development of this SEI layer and its stability. Since this process is kinetically driven, the first charge and discharge cycle of a LIB, which is called formation cycle, is typically performed under comparably small currents, as small as a fiftieth of the nominal current for some chemistries. Furthermore, the more sophisticated formation protocols, such as those aimed at creating batteries that survive hundreds or thousands of cycles, can take several days. The correct formation protocol is vital to achieving a stable SEI layer, which in turn protects the graphite or negative electrode surface from further degradation upon cycling. However, the SEI formation is not a static process, but rather a continuous partial forming and destruction of the layer during cycling. The stability of the SEI layer varies depending on the cell chemistry. Particularly the above-mentioned Si expansion leads to a larger degradation of the SEI layer and hence decreased stability overall. If the SEI layer is formed too extensively, it can inhibit the Li-ion flow upon charge and discharge and therefore increase the internal resistance. This continuous growth of the SEI and associated increased resistance, is a well-known ageing mechanism in LIB cells, especially those using Si and advanced materials in the negative electrode. The increased SEI layer also means an increased electrolyte degradation and often gas evolution within the cell. This has an impact not only on the overall cell performance, but also increases the internal pressure of the cell [46]. Particularly when it occurs in pouch cells, this gas evolution can lead to significant swelling of the

cells and needs to be considered in the manufacturing of battery modules to accommodate these volume changes.

The electrolyte degradation is also enhanced under elevated temperature conditions. Typical electrolytes use carbonate-based solvents, which have a low boiling point and will start to evaporate in many cases for battery temperatures above 80° C. This is the main reason for employing cooling systems at module and pack level. During charging and discharging at high rates, the internal cell temperatures can rise significantly, and often are more localised around the tabs of the cell. This has been the subject of many different cell geometries and cooling strategies. Nonetheless, the inhomogeneous temperature distribution inside the cell can lead to localised electrolyte degradation and associated gas evolution [1]. This effect is mostly non-reversible and leads to increased pressure within the cell, possibly leading to increased internal resistance due to less electrolyte being available [47,48] or, in the worst case, even potentially hazardous events like venting or rupture. Depending on the used electrode-electrolyte system, the onset temperature of this can vary between 60° C and 80° C and is one of the driving factors behind recent innovations in the all-solid-state battery cells development, which does not see degradation due to moderately high temperatures. The increased pressure is a mechanical aspect of cell degradation, which once more needs to be accounted for in the module and pack design. The reaction products, which strongly depend on the used chemistry and electrolyte additives, can enhance further degradation of the electrolyte and therefore lead to a more rapid performance decrease or catastrophic failure. One well-known example of such degradation is the production of hydrofluoric acid within the cell as a degradation product. This is mainly enabled by the presence of water within the cell, but is enhanced by elevated temperatures, since all electrolyte degradation products are subject to thermodynamically driven reaction kinetics [46].

2.3.2. Electrode porosity, balancing and ion insertion kinetics

There are different cell types available commercially, not solely with respect to their geometry, but also with respect to their intended application. The largest difference can be seen between cells optimised for high power and those optimised for high energy application [49]. The former often have higher electrode porosity (> 30%) and lower active material loading (1-2 mAh/cm^2). Conversely, high energy cells tend to display lower electrode porosity (< 20%) and higher active material loading (3-4 mAh/cm^2) [50,51]. High energy cells therefore often show a higher absolute capacity, with current cells achieving in excess of 100 Ah per cell. Firstly, these cells therefore inherently display different mechanical properties due to the difference in cell construction with differently loaded electrodes. Furthermore, the differing levels of loading and porosity are chosen mainly to either facilitate ionic movement into and out of the electrodes (high power cells) or to increase energy density in high energy cells. In addition, electrode balancing, which is the ratio of areal capacities of the negative (N) to the positive (P) electrode, also called N/P ratio, ranges typically between 1.05 and 1.2, with the latter being more applicable for high power cells [52,53]. The underlying principle is to provide sufficient space for Li-ions to be hosted into the respective negative anode. This ionic movement is driven by electromotive force as well as diffusion processes inside the electrode, which are directly influenced by the electrode design. With an over-capacity of the anode, ions are allowed to diffuse more easily from the electrode surface to available insertion sites. For higher rates, this diffusion process becomes the bottleneck of homogenous lithiation inside the negative electrode and can lead to various negative side effects, if corresponding C-rates are exceeded.

The variation of ionic movements has a direct impact on internal resistance, particularly at higher rates, and gives rise to potential negative side effects such as expansion hysteresis due to current density, as well as Li plating on the negative electrode. The first effect, hysteresis of electrode expansion in dependence of current densities applied, describes the diffusion path of Li-ions through the negative electrode. Li-ions are inserted first on the top layer of the negative electrode and are then allowed to comparatively slowly diffuse further into the electrode upon charging. This means that the top electrode layers are more strongly populated with Li-ions at the beginning of charging and therefore swell more locally. The swelling is decreased overall once the Li-ions are allowed to distribute more homogenously throughout the electrode [54]. This has a localised impact on the mechanical properties of the cell in a manner and can therefore influence the measurement of SOC and SOH by mechanical means. More importantly however, this effect can also result in Li plating, when C-rates exceed the inherent limitations of the electrode. When Li ions do not have sufficient time to diffuse into the electrode during charging, there is an increased chance for Li metal to form on the negative electrode surface [54]. This effect is not fully reversible and is called Li plating [54,55]. This not only results in a measurable loss in capacity, due to fewer Li-ions being available within the system, but also forms potential seeding sites for Li dendrite growth, which represents a safety hazard [44]. However, the detection of such changes during the cycling of cells can be vital for the accurate measurement of SOX and could lead to a better accuracy of its estimation.

3. Expansion-based methods

As discussed above, one main change during the operation of a LIB is the expansion and shrinking of its active material, as well as various other phenomena causing a change in volume of the bulk material. The following subsections show the methods to quantify such changes and the application of these methods. Even though they are closely linked, the methods were divided into four main types for the sake of readability, namely i) expansion-based methods (dilatometry, strain and force) ii) experimental modal analysis iii) ultra-sonic probing and iv) acoustic emission.

3.1. Dilatometry

Dilatometry is a classic method for the investigation of volume expansion in material samples. A very common application is the measurement of the increase of the thermal coefficient of probes, where temperature is controlled and the resulting change in volume is measured by the dilation of the probe in one direction. In the late1970′s the method was also extended for measurement of volume expansion due to intercalation of ions in host lattices. For investigation of LIB materials the resolution was too poor at the time. When this method was improved in the1990′s, Winter et al. [56] conducted a study in 1999 on its application for measuring the intercalation-related swelling of LIB components, in this case binder free graphite probes. The conclusion was that it can be a useful tool for observing such phenomena if handled correctly.

3.1.1. General single point 1-D contact based dilatometry

Not long after, in 2003 Lee, Lee and Ahn [57], already proposed a test setup for full cell investigation. Their setup was based on the same one-dimensional (1-D) principle as the general one shown in Fig. 4. Usually these setups consist of 1.) the electrical connection to the cell for charge/discharge, 2.) optional springs or sometimes a weight to put controlled force (F) on the cell under test, 3.) a frame which together with 4.) studs to hold the cell and the measurement device in a fixed position 5.) the cell under test (in this case a pouch cell is shown, but it can also be prismatic or even cylindrical cell) and 6.) an optional plate (it can be used to measure the expansion of the whole surface at once, and not only at the tip of the measurement device and / or to distribute the controlled force across the whole cell under test) 7.) a thickness gauge with its measurement tip. These gauges in most cases are dial indicators (as shown in Fig. 4), or linear variable differential transformers which also work as 1-D contact-based displacement sensors. These thickness gauges are usually connected to a data logger where the

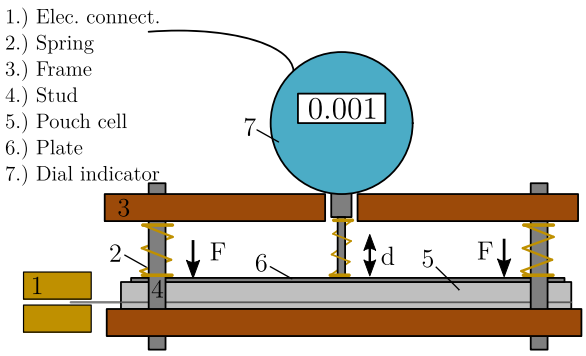

Fig. 4. Typical setup of 1-D contact measurement with dial indicator for investigation of cell expansion.

measurement is recorded time synchronized with the other values. Many studies also operate the whole setup in a climatic chamber for controlled conditions during their tests and for investigation of effects caused by certain temperatures. A similar setup / concept was later used for investigating pouch cells in [38,54,58–60], and also with vertical alignment of the cell on both sides of the pouch cell [61–64] and the prismatic cell [65,66].

In the case of Lee, Lee and Ahn [57], a plate with added weight was used and the setup was operated in a climatic chamber. They tested four different small LIB cell types with a capacity ranging from 550 mAh up to 780 mAh, with a stacked and wound electrode bulk and with a soft pouch and rigid case. They found a steep incline in thickness for the formation during the first charge (Fig. 5 (left)). This is attributed to the formation of the SEI layer. Half of the 4% increase in thickness took place before reaching a SOC of 10%. For further cycling they found between 2% and 4% reversible expansion for every cycle (Fig. 5 (right)). This is attributed to the swelling of the C anode upon lithiation. Greater contractions and expansions were observed for the cell type with a wound core. The authors speculate that this can be partly attributed to the flaky graphite used in the cells, but also partially to the type of core winding, as wound cells are known to experience higher distortions. They also discovered breathing of the cell volume for cell formats with rigid casing, which indicates that the expansion of the active material produces enough force to bend even rigid metal cases, making the swelling observable also from the outside for such cell formats.

So far, this initial study demonstrated already the potential of the 1-D method for investigating the phenomena related to volume changes of active materials of LIB in-operando. As it can be seen in Fig. 5, even for such small cells with a capacity of below 1 Ah and initial thickness of 3.5 mm the volume changes lead to changes in total thickness in the second digit range on a millimeter scale (10^{-5} m). For larger cells, these changes are correspondingly more distinct, and hence less resolution is required for monitoring. Today's dial indicators offer a resolution of 10^{-6} m and communication to an external logger starting around 200 €. The rest of the setup consists of standard mechanical supplies, so the total cost is very low compared e.g. to imaging methods. Another benefit is, that the setup is comparatively small, and thus can be operated in a climatic chamber and thus also enables placement of other sensors like thermocouples directly on the cell. These advantages explain the popularity of the method for further investigations.

3.1.2. Multi-point 1-D contact based dilatometry

Oh et al. [65] investigated the swelling of 5 Ah prismatic cells for automotive purpose with NMC cathodes and graphite anodes. With five 1-D contact expansion measurement devices, one centered and four distributed in a cross with points equidistant from the center, on each side of the cell, they had a view of the ratio of swelling in different locations. For the same cycle, they observed a maximum expansion of nearly 1.6% at the center, and a minimum of 0.6% at the side. This is partially due to the mechanical constraints of the case. As the expansion on the top and the bottom are higher than on the sides, it can be concluded that the strain on the wound bulk is not equally distributed, as the sides do not experience the same counter force due to geometric reasons - an ellipsoid bulk in a rectangular cuboid case. However, as the ratio of expansion between the measurement spots remains constant during cycling, they conclude that a single point 1-D measurement is sufficient for studying internal phenomena of the cell.

3.1.3. C-rate and temperature dependency

Oh et al. [65] performed also discharge tests with current-rates (C-rates) of 0.4, 1, 2 and 4 times the nominal cell current and found that the contraction shows its minimum for highest C-rate, although nearly the same amount of charge was withdrawn from the cell and the cell potentials are similar during discharge. The main observable difference was that during discharge the cell temperature was highest for the highest C-rate. As the difference in contraction was reduced upon a subsequent relaxation phase, where the cell was able to cool down, the authors assign the difference in contraction mainly to thermal expansion of the material, and partially to relaxation of internal mechanical stress. This is in line with the observations of Grimsmann et al. [60], where the thermal expansion of the cell was measured beforehand by inductive or joule heating and the C-rate related values were then corrected by these thermal expansion values. After a rest period to establish a (thermal) equilibrium, only minor deviations for certain intercalation states were observed. For graphite, an anode SOC of 25% yields the greatest observed difference before relaxation; after relaxation the difference was too small to be measured by the dial indicator. By measuring merely the thermal expansion of the cell via stepwise cooling and heating, Oh et al. were able to attribute the swelling

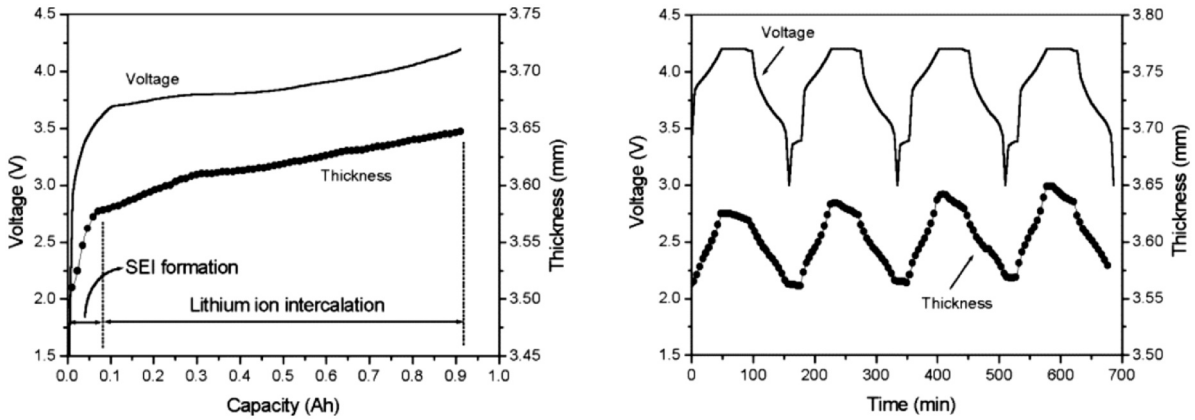

Fig. 5. Expansion of the cell upon formation (left) and reversible expansion during cycling (right) (with permission [57]).

relaxation phenomena to thermal relaxation with a similar setup in a later study [66]. The authors discovered additionally that the investigated 5 Ah prismatic cell they investigated, showed a quadratic increase of expansion for low temperatures ranging from 5° C to around 20° C, while from 20 C to 45° C the expansion showed linear growth. As the growth was also dependent on the SOC and the point of measurement at the cell, the authors attribute this non-linear behaviour (partially) to the geometry of the cell, as there are gaps in between the electrode layers and between them and the casing of the cell, which must be filled before expansion can be measured on the outside. The linear expansion for higher temperatures is confirmed by the work of Rieger et al. [62]. In this work a pouch cell was heated by using joule heating (pulse charge and discharge without altering the SOC) starting from 25° C and found a linear dependency of the expansion on the temperature with 1.1 µm/K, whereas the authors did not observe an effect of the SOC beyond the inaccuracy of their measurements. This would support the theory by Oh et al. [66] mentioned above that the observed non-linear expansion originates from the mechanical structure of the tested prismatic cell, rather than from the materials.

In addition to the results achieved above, the authors Oh et al. [65] also were able to correlate overall cell dilation with the behaviour of the anode. This was achieved by analyzing the derivative of swelling s related to the charge Q ds/dQ and comparing it to the derivative of the potential V over the charge dV/dQ (Fig. 6). Phase transitions are represented as maxima in the dV/dQ slopes. Most of those seen in the graph correlate with literature values of graphite phase transitions. The rate of ds/dQ also shows local minima/maxima at those points, indicating that the dilation is mainly caused by the changes in graphite. The cathode material NMC seems to play a marginal role and should not contribute to the peaks in swelling, as the material does not fill in stages and such does not show such distinct peaks in over-voltages as graphite does.

3.1.4. Plating and fast-charging

Bitzer and Gruhle [59] used the 1-D measurement setup to develop a method to detect Li plating in-operando in a commercial pouch cell. This was beneficial, as in-operando detection of Li plating until then had required a reference electrode to measure anode potential, which is not suitable for commercial cells. They started with initial calculations of mol masses for transferred charge, pointing out, that Li intercalation in graphite leads to less volumetric change than Li deposition on the surface of the electrode, so expansion of the cell during plating is expected to be greater. Fig. 7 shows their measurement of expansion over transferred charge for low current without plating and high current with plating. It can be seen that the expansion with plating is significantly greater than without. Another identifier for plating is the steep decrease in thickness in the relaxation phase after charging. This is interpreted as parts of the deposited Li being intercalated in the host structure of graphite. Not all the deposited Li can be dissolved again, so a difference remains. The plating at higher currents was confirmed by post-mortem analysis of the cell which clearly showed the remaining depositions of Li on the anode. In later studies, Bauer et al. [58,64] confirmed these results for Li plating and showed that during relaxation after a phase without plating, the cell is decreasing in volume, because of parts of the Li deposition on the surface being dissolved and intercalating in the anode. Grimsmann et al. [54] used a high-precision sensor to detect even small amounts of Li deposition and used this method to determine maximum C-rates for cells. This is especially useful for recuperation or fast charging of electric vehicles. Spingler et al. [67] used a contactless laser triangulation sensor for displacement measurement in pouch cells. The method was multiplexed over the area of the cell, allowing for measuring local expansion caused by e.g. non-uniform plating as well. The main goal of the study was to implement a fast charging strategy with minimum plating. The authors showed that for the cell under test, the plating was not equally distributed, but rather concentrated in the outer areas. The section in the middle was less affected and thus the setup with a 1-D measurement only in the center of the cell would have led to different results. Another comparison between single point and surface expansion measurement was done by Rieger et al. [63]. They compared a thickness gauge in the center with structured-light 3-D scanning technology of a pouch cell. For normal operation, that is, without plating, they concluded that the results of the single point expansion measurement over the SOC are well in agreement with the median expansion of the whole surface.

3.1.5. Other methods

The above-mentioned optical 3-D methods for measurement of the expansion of cells [63,67] are only described briefly to complement the other methods, as those are imaging procedures and thus not in the focus of this review. Another method already tested successfully on LIB pouch cells is three-dimensional digital image correlation [68]. For further details on those measurements see the review by Cheng and Pecht [34].

3.1.6. Implementation

A different approach for contactless measuring of the expansion of LIB cells on the basis of the eddy current principle was implemented by a General Electric Global Research team [69–71] and by Grimsmann et al. [54]. They developed flat coils for producing a high frequency magnetic field. This magnetic field induces eddy currents in a conductive material which is adjacent to the coil. Such eddy currents create an opposing field altering the initial impedance of the coil, and thus the voltage. As the generated magnetic field decays with increasing distance between coil and conductive material, the electrical response of the coil is inversely proportional to the distance between the two counterparts. The conductive material can be the casing of both a pouch or a hard case cell. Their coil works with a frequency of 2 MHz and the derived transfer function is linear for a gap range between 0.2 and 1.2 mm making it suitable for contactless battery expansion monitoring. The sensitivity achieved is between 6 mV/µm to 10 mV/µm. The concept was validated on single cells against a commercial laser distance sensor [70] and also in a battery system [71] consisting of 5 Ah prismatic cells including an additional force sensor for validation. It was found that the expansion of the cells is rather small (around 4 µm) within the constraints of the pack. However, the implementation was successfully demonstrated and validated against the force measurement, showing negative correlation.

Another contactless method for measuring the expansion of the cell over the SOC is implemented by Bohn et al. [72]. The authors of this work used an optical interferometer for investigation of pouch cells and

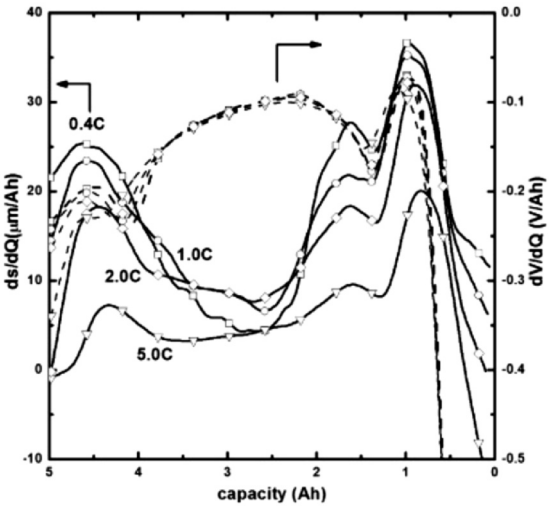

Fig. 6. Comparison of differential expansion ds/dQ (solid line) to differential voltage dV/dQ (dashed line) for various C-rates (with permission [65]).

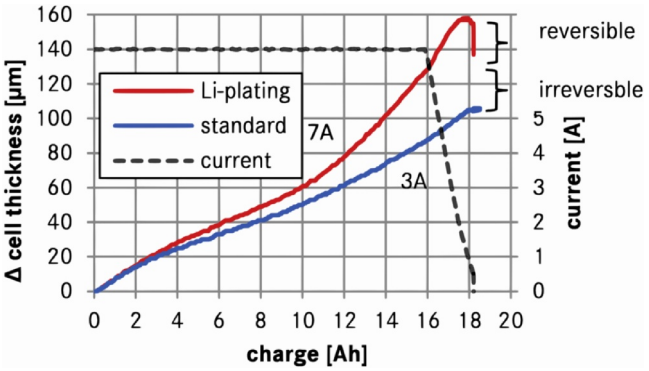

Fig. 7. Comparison of cell expansion with low current and without plating to expansion with high current and plating (with permission [59]).

achieved a resolution of 30 nm, which is very high compared to, e.g., dial indicators. For optical interferometry, usually a monochromatic light source (laser) with a wavelength λ is used. The light is sent through a beam splitter, where it is divided into two discrete beams. One beam travels towards a reference mirror being reflected to the beam splitter, the second beam travels towards a mirror installed on the target where it is reflected to the beam splitter. The beam splitter does a superposition of both signals and sends it back to a screen or sensor. A fringe pattern or light intensity is produced there, which is dependent on the phase between the two beams, which in turn is dependent on the distance of the target to the reference mirror. The resulting resolution is λ/2. A common interferometer only can perform relative distance measurements, which is appropriate for dilatometry techniques. Concepts for implementations of interferometry also capable of absolute distance measurement can be found in [73]. Beside the successful application of this technique to LIB cells, the paper does not contribute any new findings on LIB cells themselves.

3.1.7. Patents

A patent on SOC estimation via dilatometry was filed using a magnetic force sensor [74]. Here a magnet is attached to the surface of the cell and the change in distance between the magnet and a sensor on a fixed position is determined using the change in magnetic force. Another one is for implementation of eddy current distance measurement for a BMS [69]. Despite these two publications, no dedicated patents for SOX estimation were found. There are several methods and apparatus patented for quality inspection after production and for laboratory use [75–79].

3.1.8. Summary dilatometry

As shown in Table 1, mainly contact-based measurements methods were applied beside contactless measurements methods based on optical- and eddy-current-based distance measurement. As 1-D dilatometry methods usually are inexpensive and able to reveal a majority of phenomena that can occur within LIB, it is widely used for investigation at laboratory stage to get better understanding of internal processes in the LIB. The studies on SOC and C-rate mostly include hysteresis behaviour of the expansion and also anode and cathode phenomena are separated. Also, the influence of temperature on swelling is investigated in depth by several publications. No publications regarding dilation measurement for abusive conditions on cells have been found for this review. Despite the applied studies based on the eddy current principle, the method is mainly used for laboratory investigation of electrochemical phenomena. The majority of the studies was conducted on state-of-the-art LIB cells with Li-Metal-Oxide cathodes, graphite anodes, and liquid electrolyte. For possible future materials and technologies Louli et al. [38] made pouch cells with graphite and Si anodes and did full cell dilatometry to enable comparison between those materials. For (all-)solid-state LIB cells, no dilatometry measurement has been found by the time of this review.

3.2. Strain and force

As already mentioned above, the expansion of the cell and the resulting strain and force are closely linked [81]. A direct comparison is available by Hickey and Jahns [82] who measured the change in thickness with a thickness gauge and the strain on the casing with strain gauges and found a close correlation between those two values. The expansion of the active material within the limiting structure of the cell casing, leads to strain on the surface and also to forces on the outside of the cell in case there is a limitation by an additional housing structure like a battery module casing. Strain does not only arise on the surface of the cell, but also within. This phenomenon already takes place at single electrode level. Here the active material, which is coated on the current collector does not only expand in thickness of the layer but also in planar directions during Li insertion and extraction. As the current collectors usually are made of Al for the cathode and copper for the anode, which do not expand or shrink with SOC variation, this leads to strain [28]. Different thermal expansion coefficients of active material and current collector foil can also lead to strain. A method for measurement of such strain on electrodes is the curvature measurement [34,83]. Here the electrode is (pre-)lithiated and then let rest in a free condition without any external force. The strain caused by the expansion of the active material leads to a curvature of the overall electrode [28]. Considering the mechanical parameters of the current collector and the resulting curvature of the full electrode the lateral expansion of the active material can be calculated [34,83].

3.2.1. Cell force and strain

One early approach to measure the force produced by a full LIB cell during cycling was published in 2001 testing large pouch cells (50 Ah) for a stationary storage application [84]. In the study a load cell for measurement of the mechanical force is used and the goal is to better understand the ageing behaviour of different LIB cell materials. An initial force of 30 kgf (=294,199 N) was set on the load cell with a weight and for a second measurement a pressure of 0.3 kg/cm^2 (=29419.95 Pa) was applied to the device under test (DUT). In Fig. 8 the mechanical load produced by the cell with two different anode materials, pitch coated flaky graphite (PCG) and LTO, is shown. It can be seen that PCG leads to a maximum load of 480 kgf, while in contrast, LTO only peaked at 55 kgf. As LTO is considered an ideal zero strain material by the authors, they attribute this load to the LCO cathode. For both types an almost linear growth of the force for charging and linear decline for discharging is observed. Even though not stated in this work, this suggests the value being an indicator that is well suited for SOC estimation. Regarding cycle life performance, the cells with the LTO anode, and thus the least mechanical changes, shows the best ageing behaviour.

Table 1
Overview of covered areas of research for dilatometry.

Method	SOC	SOH & Cycling	Elec.-Chem.	SEI	Thermal Influence
Contact	[40,57–61,63–66,80]	[40,57,80]	C-rate [58,59,61,62,65], Plating [58–60]	[57]	[58,59,64–66]
Optical	[63,67,68,72]	[72]	C-rate [67], Plating [67]		
Eddy Current	[54,69–71]		Plating [54]		

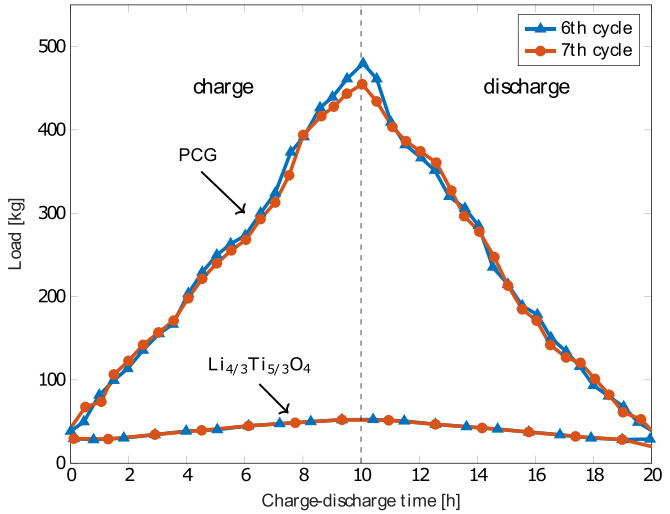

Fig. 8. Mechanical load over charge and discharge of a 50 Ah pouch cell with flaky graphite PCG and LTO anode (own representation based on [84]).

Wang et al. did a study on small pouch cells (0.6 Ah) for mobile phones focused on investigation of the volume change of the cell under constraint conditions [85]. A laboratory load cell was used and an initial load was set to 0 kgf (=0 N). The results were validated using in-situ X-ray imaging. It is shown that the strain increases almost monotonically during constant current charging, then the increase slows down in the first constant voltage phase then peaks and reduces slowly afterwards. During the relaxation phase also small relaxation effects in strain were found. During the discharge phase the strain monotonically decreased. Subsequent tests were conducted with different C-rates to better identify effects of excess volume change. It was observed that higher C-rates initially lead to higher strain and then to a higher relaxation. This behaviour is similar to the one described in Section 3.1 for dilatometry. The authors attribute this to the excess Li intercalation in the outer regions of the active material, which is higher for fast intercalation processes. During rest time the gradient of lithiation between outer and inner materials becomes less pronounced and thus the excess strain is released. The X-ray images of cell expansion delivered correlating results. The study also checked the progress of the strain during ageing of the cell and thus performed 16,250 shallow cycles with a DOD of 40%. It was revealed that the change in strain correlated well with the decline in performance of the cell. In a subsequent study Wang et al. presented a method for an implementation of strain measurement on several hard case prismatic cells in a module [86]. They also were able to confirm their measurements on small single cells with their work. Further research was done also for non-commercial technologies; Louli et al. [38] investigated the influence of SOC on both force and expansion for LIB pouch cells with Si anodes while Zhang et al. [87] investigated the pressure and expansion of solid-state small-scale LIB cells.

The connection between strain and expansion was also examined by Hickey and Jahns in their work on hard case prismatic cells [82]. They compared the measurement of the cell thickness with a thickness gauge and the surface strain on the casing with strain gauges for several spots on the cell. In Fig. 9 the cell voltage, the cell expansion and the surface strain of the cell are shown for a discharge pulse with 0.5 C. The normalized values all show similar behaviour; voltage, thickness and strain decrease with decreasing SOC. The main difference is in the impact of polarization effects on each value. The cell thickness does not show any relaxation phase during rest period and the strain also shows only minor deviation. The cell voltage on the contrary, is significantly influenced by polarization and thus the cell voltage recovers significantly during the rest phase. The authors conclude that behaviour makes the mechanical methods ideal candidates for SOC estimation.

3.2.2. Force / pressure

Cannarella et al. [88–90] did several studies on mechanical stress evolution of LIB. The authors used a load cell to put a defined pressure on the cell surface and then measured the strain the cell produces. In [88] a correlation between stress and SOC and SOH is established, the one for SOH is linear. The stress method was also positively evaluated for the detection of self-discharge. Investigation of the underlying phenomena showed that the stress to SOH relationship mainly originates from the growth of the SEI layer on the anode. Different levels of pressure were investigated in [89]. During the lifetime of the cell stress evolves for all levels of pre-set stress. For higher pressure levels the authors found a higher fade in SOH of the cell, while light cell pressure is beneficial compared to unconstrained (zero pressure) conditions. Following these observations, Mohan, Kim and Stefanopoulou [91] implemented a linear discrete quadratic estimator for cell force in addition to voltage measurement, and showed that the accuracy is improved especially for middle SOC regions. Performing a post-mortem analysis the authors found a mechanically mediated chemical degradation. Figueroa-Santos et al. [92] implemented a force-based algorithm and SOC estimation strategy for Lithium-Iron-Phosphate (LFP) cells. Combining voltage and force measurement, they were able to increase the accuracy of the estimation for most of the investigated conditions. However, they found a drift in force measurement which can be problematic and will be investigated by the authors in future. There are also proofs of concept for force based SOX estimation in modules or under module-like conditions [71,93,94]. In [90] Cannarella et al. revert the role of LIB and sensors and successfully apply LIB cells as mechanical force sensors. Knowing the force / pressure is not only relevant for SOX estimation, as this value has a major influence on performance and lifetime of a cell [11,12], it can also help to increase battery performance over lifetime.

3.2.3. Surface strain

The (surface) strain of a cell can be measured by resistive foil strain gauges (RFSG) (Fig. 10 (left)) or with fiber bragg grating (FBG) strain sensors (Fig. 10 (right)). RFSG sensors work on the change of the electrical resistance during contraction and expansion of a conducting material which usually is on a support structure. Their price is moderate and they do not require advanced measurement equipment. However, temperature compensation of DUT surface temperature can be difficult, as normally a Wheatstone bridge is used to compensate ambient temperature but this cannot be easily transferred to DUT surface temperature. In [95] a reference strain gauge is put on quartz glass, which has very low thermal strain, and inserted in the battery module to get reference values for temperature compensation. FBG sensors, on the

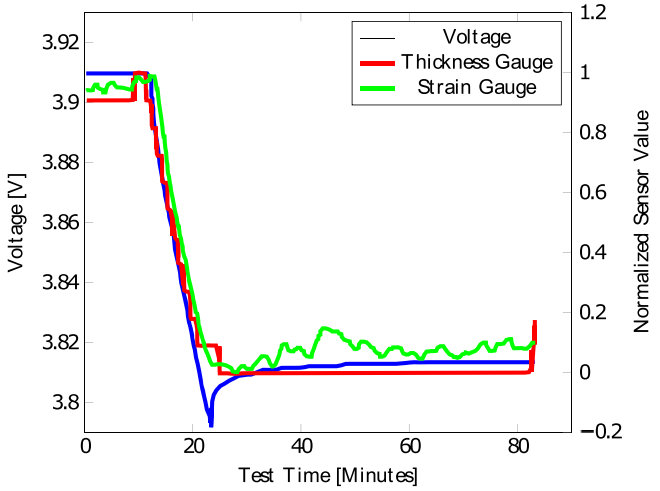

Fig. 9. Response of cell voltage, cell expansion and cell surface strain to a 0.5 C discharge pulse (own representation based on [82]).

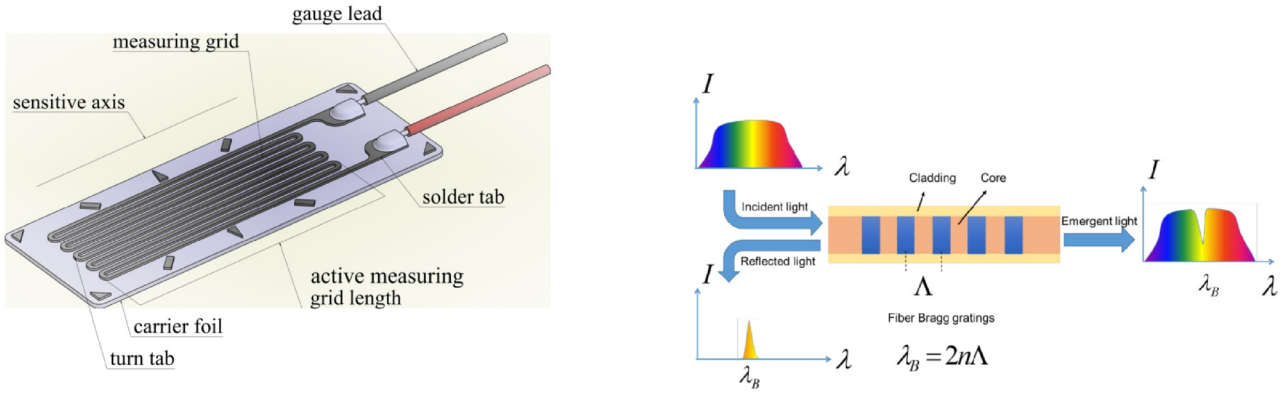

Fig. 10. Functional principle of resistive strain gauge (left) and FBG (right) [99] (CC BY 4).

other hand, work with the shift of the reflection of an optical signal passing through an expanding and contracting optical fiber (Fig. 10 (right)). FBGs are made by laterally exposing the core of a single-mode fiber to a periodic pattern of intense laser light. The exposure produces a permanent increase in the refractive index of the fiber's core, creating a fixed index modulation according to the exposure pattern. With bragg gratings, several points of reflection and thus points of measurement can be defined [96]. The FBGs are more costly than RFSGs, and need additional optical equipment for generation and processing of the signal. A benefit is that they are tolerant to electro-magnetic interference (EMI), ensure galvanic isolation, and can be used for measuring and / or compensating the temperature too, by adding an unconstrained FBG segment [97]. Sommer et al. in an initial study [97] compared these two strain measurement concepts. Therefore, they positioned a resistive strain gauge, an FBG strain and temperature sensor and a conventional negative temperature coefficient (NTC) temperature sensor on the surface of a commercial pouch cell. The resolution of the FBG setup is determined by the optical sensor interrogator (OSI), which measures the reflection of the signal. In this case 1 pm was achieved. The authors found that the FBG is capable of both measuring surface strain and surface temperature of a LIB cell. The FBG and the RFSG signal match quite well over charge and discharge cycles and over the relaxation periods; remaining differences are explained by missing surface temperature compensation of the RFSG and differing strain transfer coefficients between the DUT skin and the sensors. Another benefit of the FBGs highlighted in their work, is the smooth signal, free of noise caused by EMI, which increases the repeatability and the accuracy of the measurement. The work concludes that FBGs are well suited for LIB monitoring especially in harsh environments like battery packs in their respective applications. In a subsequent publication, Sommer et al. [98] used FBG to study excess volume of cells after cycling and their subsequent relaxation, and found phenomena like those described above in this and the foregoing section.

A very broad evaluation of FBGs for battery monitoring is given by Meyer et al. [100]. In their work the authors check the capabilities of FBGs for monitoring temperature, SOC, SOH and safety on single pouch cells and on modules consisting of nine pouch cells. For temperature and SOC the results found in other studies are confirmed. Concerning the SOH an increasing difference in strain between a full and an empty cell was observed. The authors state that for a new cell the change in strain between SOC 0% and SOC 100% amounts 40μ/m and for a cell with 400 cycles and a remaining capacity of 93.7% a change in strain of 120 μ/m was observed. This is in contrast to observations with other techniques, where the expansion and contraction of the material are reduced with ongoing ageing. Also to those of Willenberg et al. [101,102] applying in their studies RFSG to detect ageing of cylindrical LIB cells. The authors found a total increase in strain with ongoing ageing, calculated as a change in diameter, and estimated as reduced expansion or contraction per cycle.

For safety, Meyer et al. [100] found that the FBG shows earlier and more pronounced reaction to the side products produced during overcharge, than the cell temperature does. In total the authors conclude that FBGs have several assets when it comes to monitoring SOX of LIB cells and the method also works for modules. A bi-directional measurement of strain using FBG was implemented in [103]. A higher strain along the longitudinal axis was found compared to the transverse axis.

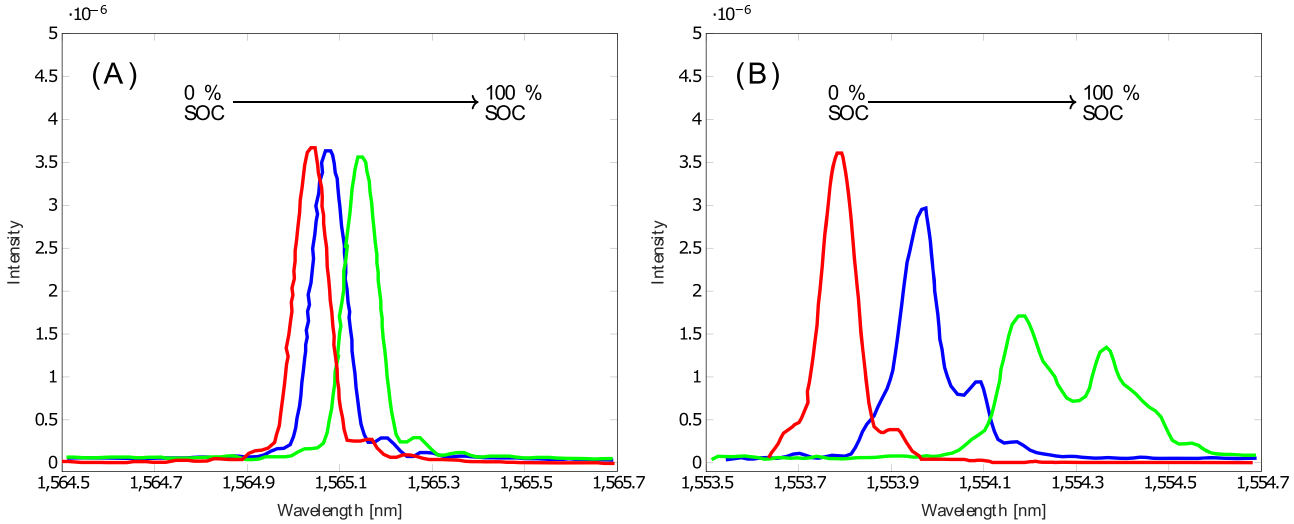

Fig. 11. Changes in wavelength over SOC for attached (left) and implanted (right) approach (own representation based on [104]).

The setup was suited to detect high-current and deep-discharge states.

3.2.4. Cell internal strain

FBGs can be made of inert material that is resistant to corrosive environments, which, combined with their properties regarding electrical insulation and small diameters [96], allows them to be integrated in cells. This has the benefit that effects in specific layers can be measured. Bae et al. [104] presented two approaches for this method. One is the 'attached' approach, meaning the fiber is between the layers on the surface of an electrode. This can be done during cell manufacturing upon stacking of the layers; the other is the 'implanted' approach, where the fiber is directly embedded in the active material. Therefore, the fiber is placed on the bare current collector foil and then the foil with the fiber is coated with active material. The diameter of the fiber is 100 µm, but the authors state that application of diameters down to 40 µm [105] is realistic. The fiber in this case is embedded in the anode which has a thickness of 110 µm, while the corresponding cathode has a thickness of 100 µm. It was found that both approaches are able to reflect the changes over SOC (Fig. 11). The wavelength of the peaks increases with increasing anode strain for higher SOC. This is normal peak shifting during longitudinal expansion of the fiber. For the implanted fiber, there is also peak splitting for higher SOCs. This is an indicator for a more complex strain field. The authors assign this observation to the longitudinal and transverse strain, the implanted sensor is exposed to as it is fully embedded in the structure. The attached fiber does not see the transverse strain as it is only on the surface and can release the stress on the separator. In addition, the authors also found a more pronounced change in the wavelength for the implanted approach. Thus it was concluded that the implanted approach is preferable for diagnostic over the attached one, as dimensional changes of electrodes can be measured directly in multiple axes and the change in strain is more pronounced.

In [106,107], a two part paper, the implementation of fibers in pouch cells is presented and evaluated. In [106] cells with different fibers are prepared and compared to cells without fibers. As sealing of the cell is very important for safety and lifetime of a LIB, the authors developed a protective heat seal film for the fiber, allowing to produce a tight cell with standard sealing method. As described above, the FBG element that should measure temperature, is not to be attached to the measured object. To achieve this in an implanted approach, the authors developed a special tubing, which allows the fiber to move under close to free conditions, while the FBG part for the strain is bound to the material using a styrene-butadiene-rubber binder. Thus strain and temperature measurement within the cell were realized. For evaluation of the effects of the sensor on the cell, cycling tests were performed. The cell without fiber achieved 1,373 cycles and the one with integrated fiber achieved 1,149 cycles, which is within the typical spread of results for prototype cells. Additionally, a cost estimation is provided. It is estimated, that, considering effects of economies of scale, the cost for such an optical measurement could be in the region of USD 100 $ to 500 $, depending on the size and type of the pack [106]. In the second part of the work [107] temperature compensation is evaluated. It was found that the internal measurement is more sensitive and less distorted than measurements on previous surface measurements conducted by the authors. They attribute this not only to the direct contact with the components where expansions take place, but also to improved temperature compensation in the embedded approach. SOC and SOH estimation was also implemented and evaluated. For SOC estimation an error of less than 2.5% was achieved using real world driving cycles and different temperature. The SOH prediction for one and 10 cycles ahead was realized with fault tolerances of 0.14% and 0.4% respectively. The authors state that the results are promising, but still they are working on further improvements.

Vergori and Yu [108] presented an integrated fiber optic approach which is not based on FBGs but on Rayleigh scattering distributed fiber optic sensors. Using an optical interrogator working on the coherent optical frequency domain reflectometry principle, the authors are able to measure temperature and strain distributed over the length of the cell continuously. The proof of concept was done on fresh pouch cells for different C-rates.

Nascimento et al. [103] presented a hybrid sensor concept, based on an FBG part and a Fabry-Perot cavity. This hybrid sensor allows for a better distinction between strain and temperature. The authors used the technique to monitor strain and temperature differences during various scenarios and at various positions in a pouch cell.

Feng et al. [95] evaluated their heat pipe based cooling concept for modules with 18650 cylindrical LIB cells using resistive strain gauges in terms of minimizing strain within the pack. As 18650 cell strain is very dependent on temperature [95,101], their cooling concept was able to reduce cell strain by 65% for a 0.5 C discharge. This is beneficial for stability of the whole structure.

3.2.5. Other techniques

Specialized strain sensors or techniques were also developed specifically for measurement on LIB. Peng et al. [109,110] designed a sensitivity enhancing structure for FBGs. This is mainly a mechanical amplifier working with bearings and leverages. The authors claim that the sensitivity of the FBG can be amplified by a factor of 11.55. Using such a sensitivity enhancing structure for FBGs phenomena which normally are lost can be detected. Choi et al. [111] developed a carbon nanotube (CNT)-based strain sensor which is manufactured by spray coating of CNT on a stretchable medium which can be attached to the cell. The design outperformed optical expansion measurements in their swelling test. O'Brien et al. [112] patented a binding belt with an integrated strain sensor for strain measurement in modules. The belt is spanned around a number of cells (representing a module) and allows to monitor the cells as a whole.

3.2.6. Patents

As stated above the method of strain and force measurement can be relatively simple compared to other methods and is well suited for SOX estimation. This led to several patents concerning SOX estimation with strain / force measurement also filed by major industrial companies in the last decade [112–119]. In [112] a binding belt with a strain sensor is laid around a number of cells which represent a module. Strain is increasing with temperature and loss in cell capacity. Patents [113,115,116,119] use resistive strain gauges on the surface of or in between cells for SOC and SOH estimation, in addition [119] provides a strain-based approach for a revival cycle for the LIB, which reduces the impacts of ageing. A load cell is used in [114] on a cell and a combination of strain and force measurement is used in [118]. In [117] strain sensors, among others, are embedded directly in the electrode and thus enabling the provision of information about each layer. Not all the patents are granted at the time of writing this review and some of their claims overlap.

3.2.7. Summary strain and force

As shown in Table 2 strain and force measurement is widely applied for SOC and SOH estimation. Various publications also present SOX estimators based on this principle. All methods are also applied to modules and are used for determination of C-rates and thermal influences on cell level, while only surface strain methods were evaluated for safety critical conditions yet. For strain measurement mainly FBG sensors were applied. FBGs are unique in that they can be inserted in cells without impacting the cell behaviour and thus can be used to measure anode and cathode phenomena separately in full commercial cells. The techniques are mainly applied on state-of-the-art LIBs, and only in [38] cell with Si/C compounds were investigated.

4. Experimental modal analysis

For the implementation of LIB in vehicles or other environments

Table 2
Overview of covered areas of research for strain and force.

Method	SOC	SOH & Cycling	Electrochemical	Thermal Influence	Safety
Force	[38,84–89,91,92,94,115,118]	[38,84,86,88,89,93,115]	C-rate [85]	[118]	Overcharge [100], Overdischarge [103], Fast-Discharge [103], Overtemperature [111,120,121]
Surface Strain	[82,95,97,98,100,101,103,110,120]	[82,100,101]	C-rate [98,103,110]	[95,98,101]	
Internal Strain	[104,107,108,117,122]	[106,107,117]	C-rate [107,122]	[107]	

where mechanical loads occur, physical properties like natural frequencies, level of damping, and the mode shapes of the cells, are of interest. In non-destructive testing the experimental modal analysis (EMA) is a common way to measure such parameters. For this purpose, the object under test is excited mechanically at some point with a force $F(\omega)$, and its response to this excitation is measured as acceleration $a(\omega)$. With these two values the frequency response function (FRF) can be calculated by applying Eq. 1 [123,124] where ω denotes the natural frequency.

$$FRF(\omega) = \frac{a(\omega)}{F(\omega)} \tag{1}$$

Amplitude and phase are dependent on ω and the amplitude typically shows a multitude of peaks over the spectrum, where each peak represents a natural frequency. Assuming the cell can be represented by a 2^{nd} order mechanical mass-spring-damper system, the stiffness of the tested object can be calculated with Eq. 2 [14,124].

$$k = \omega^2 m, \tag{2}$$

where k is the stiffness and m is the mass. The damping ξ of the test object is given by Eq. 3 [14,124].

$$\xi = \frac{1}{2Q}, \tag{3}$$

where Q is defined as the Quality-Factor in Eq. 4 [14,124],

$$Q = \frac{\omega}{\Delta\omega} \tag{4}$$

with $\Delta\omega$ as the width between the frequencies at half the maximum amplitude of its peak value (full width at half maximum).

Measurement can take place anywhere on the test object, including the point of excitation. When excitation and measurement are performed at the same point it is called a driving-point measurement (DPM); when the measurement is performed in another place, it is called a transfer measurement (TM). When the system is considered as one mass and restrained in all but one direction, it is called single-degree of freedom (SDOF), and when other directions are taken into account, too, it is referred to as a multi-degree of freedom (MDOF) measurement [123,125]. For EMA, the device under test is considered as a linear-time-invariant (LTI) system, meaning that the output caused by any combination of inputs is equal to the combination of the respective outputs caused by each individual input, and further, that the modal parameters of the system satisfy the superposition theorem, and that the modal parameters of the structure are constant over time [14,15]. Whether or not the system fulfills the LTI criteria can be tested in advance by determining the coherence for the desired frequency range and input signal [14,126]. Excitation can be conducted by impulse excitation (also hammer or impact testing), dynamic excitation and operational excitation. The first two are imposed by the test for characterization, while the third one is usually employed for verification testing of final systems. The test object can either be tested in free-free condition, meaning it is unrestrained, or in grounded condition, meaning it is restrained by clamping it down. Real free-free condition would require no influence of the testing environment on the DUT, which is not the case in reality, where testing usually occurs on a low density foam bed, as shown in Fig. 12 (left) for a pouch cell, or by hanging the DUT on springs or strings, which is shown in Fig. 12 (right) for a module; both have an impact on the setup. Hence, free-free conditions are referred to the highest natural frequency of the support medium when its maximum is 10% of the lowest frequency of the test object or if the natural frequencies are separated by at least 100 Hz. For systems like LIB cells, first natural frequencies usually are high enough for using common suspension equipment [14].

The topic of non-destructive evaluation of LIB mechanical properties entered the debate in 2013 as two research groups independently published their work [125,127,128]. The work of Pham et al. [125,127]

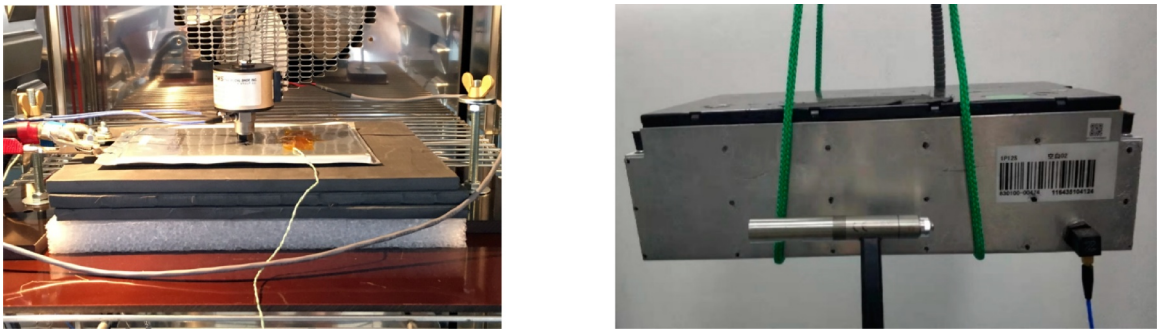

Fig. 12. Picture of FRF test setup using driving force excitation on cell (left) [124] and free-free condition for module testing with impact hammer (right) [15] (CC BY 4).

used an electrodynamic inertial shaker with an upside-down impedance head on a cell that was placed on a foam padding. Choi et al. [128] used an impulse hammer and foam padding for one test, and clamped the cell on a shaker test bench for another test. Also Hooper et al. [14] and Li et al. [129] used an impact hammer evaluation for pouch cells. The upside-down inertial shaker setup was also applied in the same manner by Popp et al. [124] and Luthfi [126]. As the shakers with impedance head have high masses (in case of [124,126], 269.2 g) compared to the tested cells (in case of [124], 418.6 g, and in [126], 171 g), no free-free condition is achieved with this setup, as sensor weight would have to be less than 1% of the measured unit [14]. This is a valid approach if the purpose is the detection of changes in the FRF, like in [124,126] but the weight of the test equipment does impact the overall frequencies of the system [123]. Fig. 12 shows such a setup for driving point measurement on a pouch cell (left) and a free-free condition for impact testing with a hammer on a battery module (right). Berg et al. [123,130] designed a test bench with a similar setup for free-free condition measurements of LIB cells, where the excitation is not performed with a hammer but with a stinger from below, coupled with a mechanical force transducer, and the measurement is executed with a common mechanical acceleration sensor for DPM that is also placed on other spots to perform TM.

All of the studies applying the upside-down measurement on pouch cells [124–127] and a study using an impact hammer [129] discovered a correlation between the SOC and the natural frequencies of FRF. As shown in Fig. 13, the peaks in the FRF, which represent the natural frequencies of the system, shift towards higher frequencies with higher SOC. Excitation was performed applying a linear sine sweep from 20 Hz to 3 kHz. The other study on pouch cell using the impact hammer [14] and the stinger [123] for excitation, did not find a significant SOC dependency. In [123], it is argued that the studies that did find such correlations, used linear sine sweep excitation, which is known to sometimes excite the nonlinear behaviour of a system. Therefore [123] used a random excitation to avoid this risk. However, as coherence tests were performed in [125–127], all resulting in a value of one (one means ideal linear behaviour) for the frequencies investigated, this might not necessarily be the reason. Additionally, in [126] contactless dilatometry was performed, finding correlations between the shift in FRF and the dilation of the cell. For prismatic cells, and using random excitation, the FRF dependency on SOC was found in another study [130] too while Volk et al. [131] did not find a significant influence of SOC on FRF on module level. For the prismatic cell used in [130], the authors were able to correlate the changes in FRF to literature values of intercalation induced swelling. On the whole, the current literature comes to varying results on the impact of SOC on the FRF.

Studies [123,124,126,129–131] also had a look at ageing. Luthfi [126] observed one cell permanently during cycling, while the others took new and previously aged cells for their study. Like in the case of the SOC, the results on SOH are quite inconclusive. While no differences were found on modules [131], all studies on cells found higher natural frequencies for aged cells, while e.g. [123] found much higher relative shift for a cell with a SOH of 90% than [124] for a cell with a SOH of 75%. This difference could be explained by the lower impact of the deviations of the cell in [123] on the total FRF of the cell and the comparably heavy FRF equipment in case of [124] impacting the overall frequencies of the combined cell and measurement setup. For stiffness of the cell, [124] states that it is negatively correlated with SOH and the cell becomes softer as it ages, whereas [123,130] concluded the opposite. For pouch cells one would conclude that the ageing effects like gassing, structural disordering and delamination (see also above) would lead to a softer structure in the nearly unconstrained gas filled pouch cell, which was evacuated tightly at the beginning, showing a more rigid structure. The restraining casing of a prismatic cell could lead to a stiffening of the total structure because materials cannot expand much. To overcome this ambiguity, new cells should be cycled and regular checkups of capacity and FRF should be performed as proposed in [126], but with a higher number of samples, and also different cells and cell geometries. Such an approach is also recommended in [130], where the problem of ambiguity was identified as well.

For influence of temperature on FRF and modes, the literature states uniform results. With lower temperature the cells become stiffer and natural frequencies become higher [123,124,126,130]. The change in values can be drastic. In [130] a fully charged cell at 17° C has a first natural frequency of around 800 Hz, while a discharged cell at 38° C has a first natural frequency of around 500 Hz. The concomitant damping ratio is reduced from around 9% to around 5%. Findings in the other studies support the significance of these values [123,124,126], e.g.

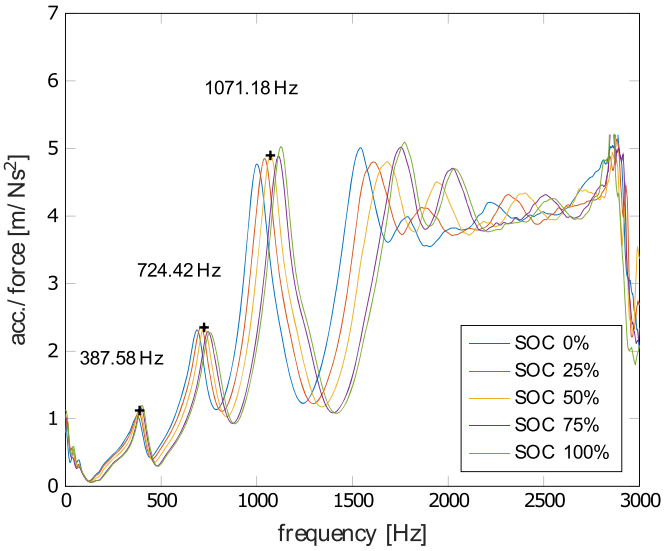

Fig. 13. FRF for several SOC resulting from linear sine sweep with upside down shaker and driving point measurement [124] (CC BY 4).

[124] states that temperature becomes the dominant value outweighing the influences of SOC and SOH.

While [130] states that this shift in mechanical behaviour needs to be considered for e.g. vibration endurance testing, [14] states that natural frequencies over 150 Hz do not have an impact on behaviour in automotive applications, since above this value, no frequencies with strong enough magnitudes are taking place to interfere with the measurement. None of the studies discussed above found a natural frequency below this value (150 Hz) for any condition investigated. For certain special applications those frequency regions might still be of interest as well as for construction of battery modules and systems.

As described above, not only the natural frequencies and the damping but also the mode shapes of objects are of interest for mechanical integration. Therefore, TM is necessary. This is done for pouch cells [14,123], prismatic cells [130], conventional modules [15,131], and composite and laminated structure modules [132] where the batteries are directly embedded in the structure. Fig. 14 (left) shows a setup of a MDOF testing on a module with LIB prismatic cells [15]. The points of impact in this case are excited one by one by hitting them with the impact hammer. The response is always measured in the same spot. The same procedure is followed in [14] for a cell in an SDOF setup, meaning all impact points are on the same side as the measurement. In [123,130] the excitation takes place at one point with a stinger and the measurement is performed at different spots. The same protocol is followed in [132], but for integrated module structures, and using a contactless laser Doppler vibrometer to measure the response over the structure. From the relationship between the FRF of each point of excitation and each point of measurement the transfer function of the system dependent on the frequency can be derived. In Fig. 14 (right) the FEM Simulation of a module and the measured mode shapes are compared [15]. Two mode shapes of six were extracted from the paper for the purpose of explanation. The grid structure results from the points of excitation shown in Fig. 14 (left). The first observed result is for the 1st order mode shape and shows a torsion, implying a twisting along an axis of the module and for the 2nd mode shape along the x-axes. The authors used the comparison of the FEM to the EMA results to demonstrate, that complex anisotropic LIB cell models (where the layered inner structure is considered) do not necessarily lead to better results in the overall simulation of a module, compared to less complex models where the cell is taken as a homogenous object.

4.1. Patents

No patents specific to batteries were found.

4.2. Summary experimental modal analysis

EMA is a relatively new topic for the instrumentation of LIB. It has already been applied to various cell formats and systems. From the current state of the literature, no clear conclusion can be drawn about the impact of SOC, SOH, and other effects on the EMA behavior and FRF. As shown in Table 3 it is not used to investigate internal phenomena of cells or modules yet. However, it proved to be a very useful tool for investigation of mechanical properties for development and mechanical integration.

Table 3
Overview of covered areas of research for experimental modal analysis.

Method	SOC	SOH & Cycling	Thermal Influence
Pulse Excitation	[14,129]	[129,131]	
Sinus Excitation	[124–127]	[124,126]	[124,126]
Stochastic Excitation	[123,130]	[123,130]	[123,130]

5. Ultra-sonic probing

In ultra-sonic (US) measurement, usually an actuator emits a mechanical wave into the DUT, the wave propagates through the medium / media, and a sensor measures the response of the system to the excitation. Thus, the acoustic impedance Z (Eq. 5) of the system is measured.

$$Z = \rho c \tag{5}$$

Here ρ is the material density of the DUT and c is the speed of propagation of the wave. The higher the density, the higher also the impedance and thus the attenuation of the signal. A single device can be used as both actuator and sensor, if reflections are measured and the actuator is put into sensing mode after emitting the signal for pulsed operation. In an unbound elastic medium, two types of waves can be found [133,134]: i) longitudinal waves, also called pressure (P-) or compressional waves. The displacement of the medium occurs in the same direction as the propagation of the wave. It can travel through both solids and liquids. The waves generate a compression of the material they are traveling through; ii) transverse waves, also called shear (S-) waves. The displacement of the medium is perpendicular to the direction of the wave propagation. It can only travel through solids. These two wave types are mainly of interest for through-body or reflection measurements. When reaching an interface, the waves are partially reflected, and the ongoing wave is attenuated. If the waves reach an interface at an angle, S-waves will arise. The larger the difference in mechanical impedance between the interfaces, the higher the magnitude of the reflection. In the case of LIB, with their thin laminated structures, these reflections lead to another type of wave propagation, so called Lamb (surface) waves [133]. Guided surface wave systems for LIB are mainly based on this type of wave propagation. As the materials of the LIB change mechanically during operation, the speed of propagation of the signal through the cells and the amplitude of the signals change, as well. The signal speed of propagation is usually measured as the time between sending and reception of the signal - the so called time-of-flight (TOF). Usually, the TOF is evaluated by the cross-

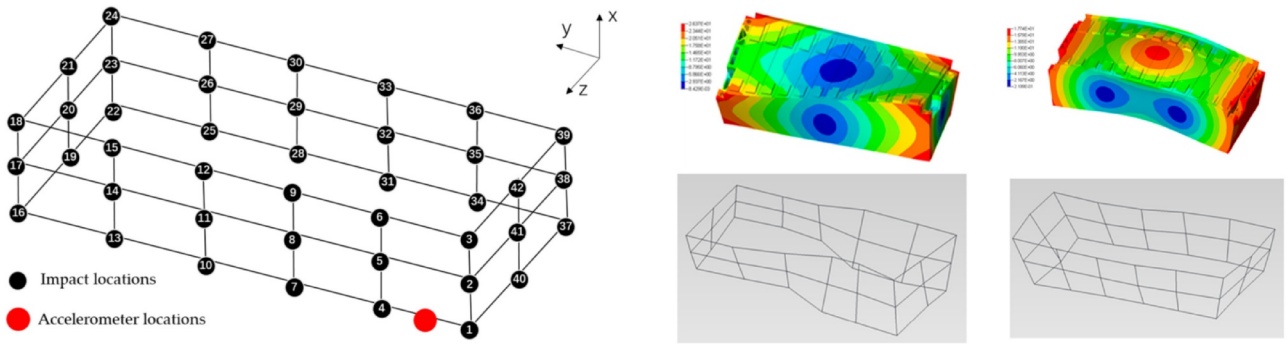

Fig. 14. Points of excitation and measurement for a LIB module with prismatic cells (left) and comparison of identified modes with FEM simulation (right) [15] (CC BY 4).

correlation [135] of the input with the output signal as described in (Eq. 6),

$$[f^*g](\tau) = \int_{-\infty}^{\infty} f(t)g(t+\tau)dt, \tag{6}$$

where f is the emitted signal, g is the received signal, t is the time and τ is the delay of the signal [136]. The point of maximum correlation is taken as a basis, and the change in τ is then the change in TOF. Another method is the comparison of the total signal amplitude A [135] as shown in (Eq. 7),

$$A = \int_{t_i}^{t_f} |f(t)|dt, \tag{7}$$

where t_f and t_i limit the waveform measurement window [136]. So the total transmitted signal strength is measured and can be compared for various states. Another method for postprocessing of US measurement is the comparison of the minimum of the Hilbert transformed signal which led to better results than the total signal amplitude method for the cell presented in [135].

There are mainly three types of measurement for US on batteries. In Fig. 15 they are shown for a pouch cell. In the reflection measurement, any of the actuators (1 to 3) sends a wave and is then put into receiving mode as sensor measuring the reflection of the signal from the opposite side and from the interfaces in between. In the through-body measurement, emitter 1 sends a signal which then is received by sensor 3. Surface waves are measured when emitter 1 sends a signal which then is received by sensor 2.

5.1. Through body measurement

The first publication covering US diagnosis on batteries that was found for this review, is a patent by Redko et al. [137], which was filed in 2007 and granted in 2010. It concerns remaining service life estimation of electrochemical energy storage in general, but also mentions LIB explicitly. The apparatus comprises a set of US sources on one side of the DUT and US sensors on the other side, so they are measuring through the body. No frequency range is defined; it is stated that the method is for 'high-frequencies'. The authors propose to use reference samples at known states of degradation or cycle life, respectively, and map their attenuation of the US signal for several voltages. The lookup tables generated in this way can then be used to determine the SOH or the remaining useful liefe (RUL) of samples.

After this patent it took several years for the first scientific work in this field of application to appear: in 2013 Sood, Osterman, and Pecht [138] presented an approach for SOH determination using US sensing. Their setup comprises an emitter / receiver combination on one side of a pouch cell and a pure receiver on the other side. The sender / receiver combination works in echo mode, thus measuring the reflection of the signal. This should enable the setup to detect and localize areas of degradation. The receiver on the other side is used for through-body transmission measurement to obtain information about the various interfaces in the cell. In their validation of the method, the authors compare the signal of a relatively new cell to one which already has had a long service life. It was found that the damping and the TOF of the signal were much higher for the cycled cell. Sood et al. [138] validated their findings by showing the swollen and delaminated structure of the aged cells with an X-ray image and argued that this softer structure leads to increased damping and higher TOF through the medium.

Hsieh et al. [139] did a study on TOF variations in LIB and alkaline batteries as a function of SOC and SOH. They used 2.25 MHz as sampling frequency in transmission and reflection measurement. The transducers were held in position with special holders and glycerine was used for mechanical coupling. The authors found significant differences between TOF and the transmitted signal and attributed this to internal changes in structure, concluding that this method was suitable for SOC and SOH determination. In a subsequent study [140], the authors investigated the method for catastrophic events like overcharge, over-discharge, and elevated temperatures, validated the results by conventional post-mortem analysis, and concluded that the US probing, especially combined with numerical analysis methods, is capable of detecting SOC, SOH, and the impacts of catastrophic events.

An approach for transmission measurements through the cell using comparatively cheap non-laboratory equipment was presented by Gold et al. [141]. They implemented standard piezo buzzer discs with a resonance frequency of 6.4 kHz as transmitter and receiver, and glued those directly onto the pouch cell surface with epoxy resin. Such a measurement setup could be feasible for implementation in a real world application. For the signal waveform, raised cosine pulses wit N oscillations ($RC_N - pulses$) were implemented. By running trials, the authors identified a signal frequency of 200 kHz as the optimum point for their setup. Fig. 16(a) shows the measured waveform for a fully charged and fully discharged cell for the same excitation signal. For this cell, a fast P-wave was observed, which does not change significantly in TOF nor in amplitude for the fully charged and discharged states. Additionally, a second slow S-wave was observed, which for the discharged cell has a significant delay in time and a high attenuation compared to the signal measured for fully charged cell. This behaviour becomes even more obvious when looking at the smoothed signal modulus in Fig. 16(b). The amplitude is reduced to (14.08 ± 0.61) % and the maximum of the second signal is found at (101.47 ± 0.66) s compared to (88.53 ± 0.99) s for the charged state.

To evaluate this behaviour further, the authors performed the measurement starting from 0% SOC going to 100% SOC in steps of 20%. In Fig. 17(a) the signal heights for each SOC step are arranged next to each other. The dashed blue line marks the peaks of the fast wave and the solid red line those of the slow wave. As the blue line is horizontal and crosses all the peaks, it is shown that the fast wave amplitude is nearly constant over SOC. The red line shows a linear growth with increasing SOC. For the TOF shown in Fig. 17 (b), the blue line is also horizontal, meaning constant TOF over SOC, while the red line shows a linear decrease in TOF for an increasing SOC.

While [141] for their cell and setup found linear behaviour for the transition of the signal over SOC, other studies also found local minima and maxima [9,135,136,142] on the signal. In case of [136,143] these are in the lower single digit per cent region of the total change, while in case of [9] it is around 16% of the total change in amplitude. There might be several reasons; one is that the local minimum mostly occurs near the discharged state and could originate from the behaviour of the nearly fully delithiated graphite [136]. Using steps of 20% SOC the tests in [141] do not have sufficient resolution (in terms of SOC) to measure this effect, as it lies in between two steps. The other studies perform continuous measurement and thus can detect these extrema. Other influences could be the frequency range, the measured wave, the time for relaxation and the behaviour of the material used in the cell. In [141] the authors claim that by trimming the frequency until the wavelength corresponds to the thickness of each layer of the battery, a region of monotonous (negative) growth in both signal amplitude and that these

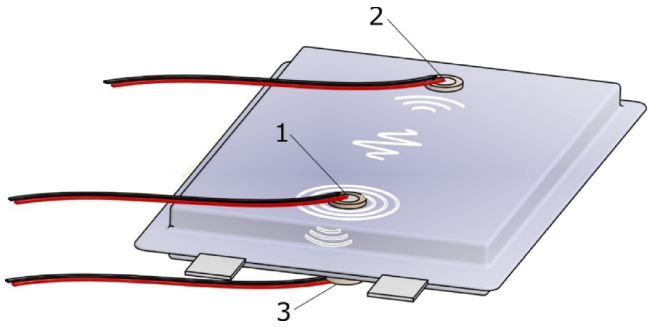

Fig. 15. Pouch cell with piezo discs as actuator and sensor.

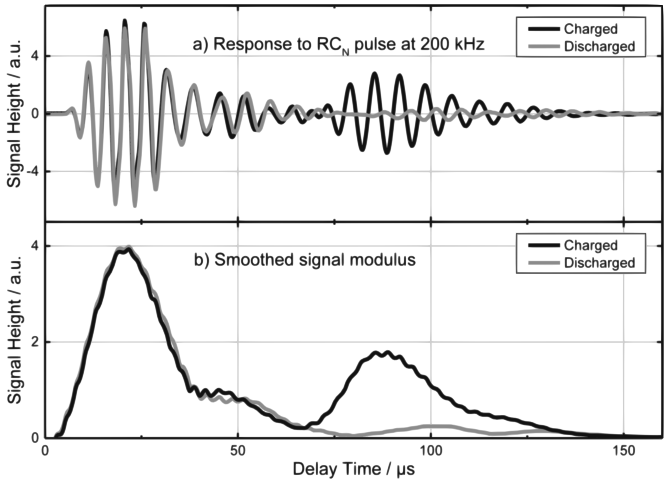

Fig. 16. Received US signal for a fully charged and fully discharged pouch cell. Response to RC_N – *pulses* (a) and smoothed signal modulus (b) (with permission [141]).

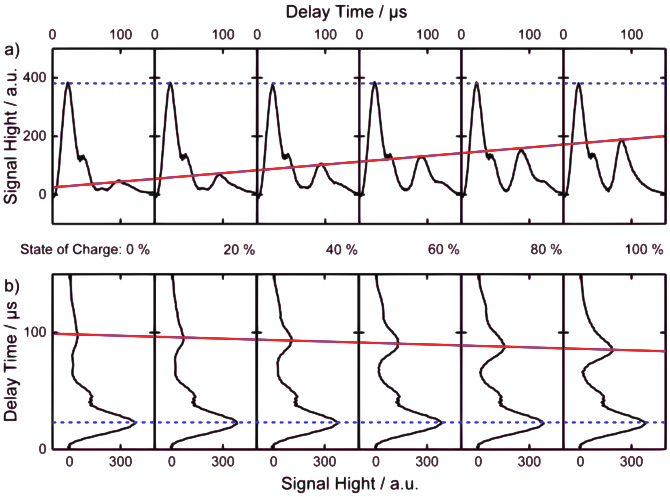

Fig. 17. Received US signal showing the trend of signal height (a) and delay time (b) for different SOC (with permission [141]).

findings are not restricted to this cell but also transferable to other cells applying non-zero strain materials.

5.2. Surface waves

A cooperation between Stanford University and Rensselaer Polytechnic Institute resulted in several publications on LIB monitoring using guided surface waves [142–145]. The authors use piezo transducer discs directly attached to the surface and perform the excitation with a windowed sine signal with a frequency of 125 kHz. In [142] both the signal amplitude and the TOF to SOC and cycle life of the cell are correlated. With a statistical analysis they show that US diagnostics could be used for SOC and SOH prediction with inaccuracies well below 1%. In a subsequent publication [143] the researchers collective uses matching pursuit decomposition, which decomposes complex guided wave signals into a combination of simpler, localized atoms, allowing the time-frequency information of the signals to be mined. By using statistical methods on this information, combined with the cell voltage, the authors can perform SOC prediction with a margin of error of 0.36%, and SOH prediction with a margin of error of 0.05%. They expand this approach to end of life (EOL) prediction [144] which even works when the cell SOH drops without cycling, due to external influences, e.g. mechanically induced fatigue of cell performance in this case. Also, Davies et al. [136] presented an approach where they apply machine learning to both single values / and a combination of cell voltage, US amplitude and TOF for an LCO and an LFP battery. They were able to reduce the error for SOC prediction from 0.03% achieved by measurement of voltage to 0.01% by combining all three parameters for the LCO cell. For the LFP cell with its partially flat voltage curve the error decreases from 0.06% to 0.01%.

Robinson et al. [146] performed a spatially resolved measurement of surface waves on a commercial mobile phone battery. They found different propagation speeds all over the surface, with regions where TOF increases, decreases or does not change at all with increasing SOC. This behaviour can be attributed to the cell design. The regions with no change in TOF are not in mechanical contact with active materials; for the other regions, the differences are explained by the position of the current collector, which serves as an anchor, leading to different mechanical stresses all over the surface. In a subsequent study [147] the authors evaluate US probing by using time resolved TOF measurement for several factors, such as temperature and C-rate. For their measured TOF at two temperature levels, 25° C and 30° C, they did not find a change in TOF, as opposed to [9]. Travel time of the signal should be higher when the temperature increases, as the cell expands (see Section 3.1) and becomes softer (see Section 4). Concerning C-rates, the authors were able to find higher stiffness of cells under high C-rates represented in the US signal.

5.3. Implementation

An approach for low-effort implementation of US diagnostic for BMS was presented by Popp et al. [9]. Instead of windowed sine signals, which requires advanced circuitry and amplifiers, the authors use a MOSFET as regular semi-conductor switch to drive the piezo disc actuator. The transferred signal is then captured using edge detection and also a piezo disc for sensing. With a tracing algorithm, the system can follow the correct edge and its changes over the SOC; this permits measurement of SOC. The excitation and the post-processing of the data are performed with spare channels on the microcontroller of an existing BMS. Changes of the TOF due to temperature changes of the cell were evaluated and a function was fitted to compensate those influences for SOC estimation. Thus, a margin of error of 1.69% of measured TOF value is stated for a real-world driving cycle on which the system was evaluated. The materials cost of the system was estimated at less than 10 € for the single prototype, that is, without benefit from any economies of scale.

5.4. Non-contact based method

While all of the above setups use direct coupling of the transducers and sensors with the DUT, Chang et al. [148] presented a method where the transducer and sensor are placed 40 mm apart (in air) from the pouch cell with NMC/G electrodes under test. The excitation frequency is 400 kHz with a sampling frequency 20 MHz, respectively. They found that detection of SOC is possible even when the signal to noise ratio is low for such a setup. Additionally, they state a nearly linear relationship between the amplitude of P- and S-waves and the SOC of the investigated cell.

5.5. Abusive scenarios and safety

Despite the methods described above, which are all about SOC and SOH estimation, there are also publications starting in early 2019 that use US probing for observation of LIBs under abuse conditions and out of the operational window. Oca et al. [149] used through body measurement with frequencies between 120 kHz and 500 kHz to detect under-discharge and overcharging for Li-Ion capacitor (LIC) pouch and prismatic cells. Their cells have an operational voltage of 2.2 V to 3.8 V and they are subjected to 'mild' abuse conditions of 2.0 V and 4.5 V and

to more challenging ones of 0 V and 5.2 V, respectively. The study investigated both the attenuation as well as the TOF of the signal. It was found that during mild overcharge the cell already reacts in its acoustic behaviour, while no changes in the electrical behaviour are visible. In under-discharge both the attenuation as well as the TOF can determine the internal side reactions promptly. The acoustic method works until the casing of the cell loses contact with the bulk material, indicating a very advanced state of abuse conditions. Wu et al. [150] performed US reflection measurements during overcharge of a LIB pouch cell, and also found that the TOF increases during overcharge, while there is a relaxation afterwards. But even after this relaxation a significant hysteresis compared to an unharmed cell persists.

Zappen et al. [121] performed US measurements during abusive high temperature testing of LIB cells. They conducted in plane-and through-plane measurements, using piezo discs. Post-processing of the signal was performed with signal intensity and center of gravity calculations. Different heating regimes were applied, and the cell was also monitored using electrical impedance spectroscopy (EIS). The authors discovered, that EIS and US are able to monitor safety-critical behaviour of LIB due to overtemperature, as the values correspond to distinct temperature levels where e.g. SEI decomposition and evaporation of the solvent occur.

Also, plating processes are detectable with US probing as shown by Bommier et al. [151]. They investigated plating on small 651628 (LCO/graphite) pouch cells using US probing across the cell with 2.25 Mhz and processing of TOF and total amplitude, as well as by destructive post-mortem analysis to confirm the results. Fig. 18 shows their results for first normal cycling, and then for increased charge rates where plating is supposed to take place. At the top, the acoustic heat map (which is an intensity plot) is shown. It can be seen, that the TOF repeatedly varies during low current cycling, while it becomes greater in total when the plating process starts; also, the intensity of the signal is reduced during the higher C-rate cycles, which can be also seen in the amplitude plot in the middle. For ongoing cycles, this behaviour continues until the signal disappears completely during the third cycle. The authors state that this might be related to plating, but even more might be related to gassing of the electrode, as gases have a totally different acoustic impedance and thus lead to high signal attenuation.

5.6. Patents

As already mentioned, the first publication on the topic of US sensing was a patent [137]. Here through-body waves are measured to determine SOH, which is the basis for further inventions [152,153] where the method was extended to other SOX and described in more detail. A method for SOX estimation based on surface waves was filed by Ladpli et al. [145].

5.6. Summary ultrasonic sensing

US diagnosis of cells has been becoming increasingly popular in recent years. Not only operational values like SOC and SOH but also abusive conditions like high temperature, plating and overcharge can be detected (Table 4). As measurements with small and inexpensive piezo discs are possible, there is a possibility for real application even in BMS. The technique has been implemented successfully for frequencies from 25 kHz up to 2.25 MHz, while approaches for use as laboratory method tend to higher frequencies and closer-to-application approaches tend to lower frequencies. Although the vast majority of the studies is on pouch cells, Oca et al. [149] showed that the technique can also be applied to hard case prismatic cells. Studies were carried out on state-of-the-art LIB cells and materials.

6. Acoustic emission

Though acoustic emission (AE) also works based on detection of sound, it differs from the methods named above as the DUT does not undergo an external mechanical excitation. Rather, the emission of waves of the material itself, normally created by the quick release of mechanical stress, is measured by an attached (surface) microphone [26]. As a potential source of the AE events in LIB several side reactions related to various degradation mechanisms of a battery cell could be listed. These are electrode cracking, transition metal dissolution, cathode electrolyte interface (CEI) formation, SEI formation and thickening, Li plating, structure disordering, exfoliation and decomposition.

The working principle makes AE per definition an in-operando method. In contrast to all the methods discussed above, it does not work on a LIB which is not in operation or in a relaxation phase closely following an operation. As the release of stress normally is spontaneous it generates a pulse, which contains a broad range of frequencies. Bubbling of the electrolyte leads to lower frequencies (see below). Typically, the most interesting frequency regions range from a few kHz to a few MHz, and hence, the equipment must be chosen accordingly.

Fig. 19 shows a typical setup for measuring AE on a LIB cell on the top and the bottom. The acoustic path is drawn in black, the electrical circuit in blue. The LIB cell (1) usually has the AE sensor(s)/transducer (s) (2) directly attached to its surface, in this case one on the top and one on the bottom. Those sensors are connected to pre-amplifiers (3), then the signal is filtered (4) to minimize noise, and then the filtered signal is amplified again (5). Usually, an acoustic event counter and signal conditioning unit (6) does the signal processing. The processed signal is then transferred to the computer (7), which does the data logging and can set the parameters like signal threshold for the signal condition unit. A controlled electrical source / load (8) is used to cycle the battery according to the required protocol. In some setups, material to mechanically decouple the cell under test from the testing environment can also be found.

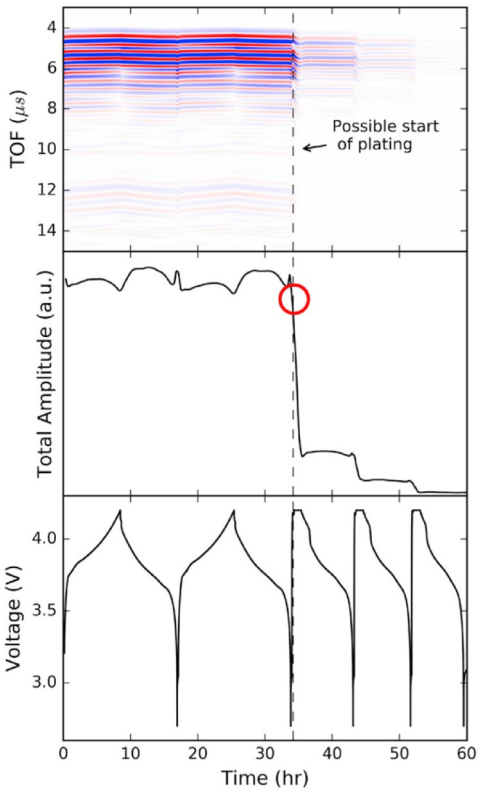

Fig. 18. TOF acoustic heat map (top) amplitude of transferred acoustic signal (middle) and cell voltage (bottom) during cycling of [151] (CC BY 4).

Table 4
Overview of covered areas of research for US Sensing.

Method	SOC	SOH & Cycling	Elec.-Chem.	SEI	Thermal Influence	Safety
Through Body	[136,139–141,147,149]	[136–140]	Plating [140,151], C-rate [141,147]	[139]		Over-temperature [121,140], Over-charge [140,149], Over-discharge [140,149]
Reflection		[150]				Overcharge [150]
Surface	[9,142–144,146]	[142,144,145]	C-rate [9]		[9]	
Air	[148]					

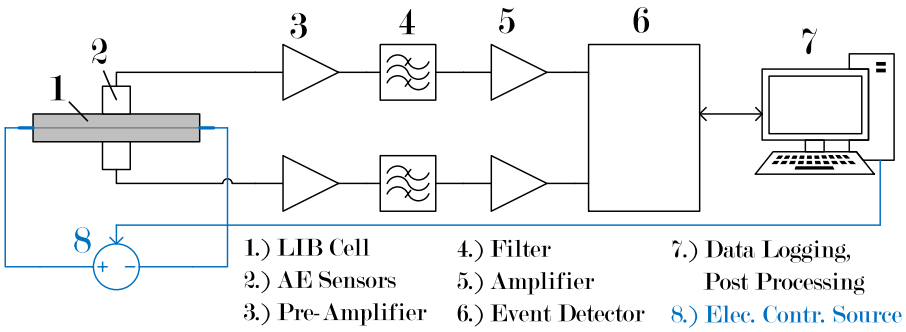

Fig. 19. Typical setup for AE testing of a LIB cell. Acoustic path is depicted in black, electric circuit in blue. (For interpretation of the references to colour in this figure legend, the reader is referred to the web version of this article.)

6.1. Half and coin cell measurements

AE was first employed for LIB to detect particle fracture of LMO cathodes by Ohzuku, Tomura and Sawai [154] in 1997. They implemented a laboratory setup where they measured pellets of active material with a diameter of 11.3 mm and active material pasted on Al foil against Li as counter electrode. The AE sensor was attached to the bottom of a self-developed test bed for such cells. An amplifier for detection of acoustic events was used. This means that when a signal over a certain threshold is detected, a 1 ms pulse is given on the output of the equipment, and this pulse is then counted as an event. The more events counted, the more changes in the material are occurring. Based on their previous work, the authors presume, that higher currents lead to higher stresses in the material, due to the gradient in lithiation between material that is in contact with, or close to the electrolyte and material that is further away. When the stress at a certain spot reaches a certain limit, the particle undergoes fracture and emits a sound wave. Thus, testing is done with lower and higher discharge currents and the acoustic events are counted. A discharge at 5 mA/cm^2 led to a maximum of around 700 events per minute and a total number of around 25,000 events, while lower rates e.g. at 1 mA/cm^2 led to a maximum of around 30 events per minute and around 7,000 events in total. When the current was reduced further, the number of events was in the single digit range. The authors were also able to detect some events during relaxation phase. Fewer events were recorded for the standard type electrode than for the pellet. This leads the authors to the conclusion that the preparation and dimensions of the electrode plays a major role in electrode stress, and that AE technique is a suitable tool for investigating the behaviour of the electrode samples. By analysing previous studies and the observed spectra of their findings, they also state that a characterization of physical processes like material fracture, phase transition or gas evolution should be detectable.

Kircheva et al. [155] investigated the formation of SEI on graphite with AE. They based their study on a coin cell with Li as counter electrode. By attaching an AE transducer on both sides of the cell (one was placed close to the graphite and one close to the Li- based electrode like shown in Fig. 19), and by trimming the threshold levels of each sensor to the specific electrode emission accordingly, they were able to distinguish between acoustic events originating from the graphite or the Li. Initially, such cells have an open circuit voltage of around 3 V. During the initial minutes of the first discharge of the cell, a sharp increase in acoustic activity is observed. The authors attribute this to initial cracking of the chemical passivation film. Then there is a plateau followed by a high concentration of acoustic hits in the region between

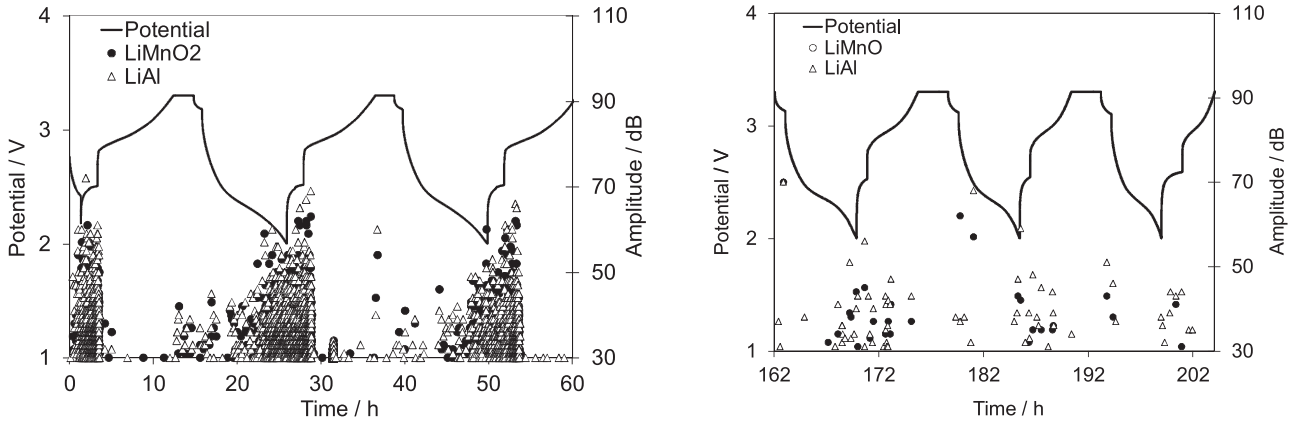

Fig. 20. AE analysis of LiAl/LMO cell during cycling for a new cell (left) and for the final cycles at aged state (right) (with permission [156]).

0.8 V and 0.5 V, where the SEI formation and according electrolyte decomposition are known to take place. The hits are fewer than for the subsequent region, and followed by several clusters of hits which correspond to the plateaus of Li staging into graphite in a region between 0.2 V and 0.01 V. As the AE sensor on the graphite side shows many more hits than the one on the Li side, the effects are attributed to the graphite electrode. The cells did not show so many hits in the region of SEI formation later on, a sign that the ones occurring during the first cycles were really originating from the initial SEI formation. The authors observed the same amount of cumulative acoustic energy independent from the C-rate used in cell formation. This is an indication that SEI formation, being a surface phenomenon, is not dependent on current densities as observed for intercalation phenomena like those describe above for LMO [154]. In another study, Kircheva et al. [156] investigated cells with Li-Al (LiAl) anode and LMO using a similar setup. For this cell several cycles were executed so that the cell already showed signs of ageing. Fig. 20 depicts the measured acoustic hits for the first cycles (left) and for the final cycles (right) during the test period. It is shown, that there are clusters of acoustic hits for the first cycles, especially at lower potentials. For the final cycles, there are only occasional hits, distributed more equally over the cycle. As the capacity of the cell degrades too, a correlation between fewer acoustic hits and reduction in cell capacity was established.

In their study on the LiAl/LMO cell [156] the authors also have a look at the characteristics of the acoustic hits. These can be differentiated by parameters like (peak) frequency, duration, and energy. Thus, it is possible to attribute the hits to phenomena in the cell, based on the acoustic characteristic. Bubbling of the electrolyte caused by decomposition is known to produce frequencies between 80 kHz to 250 kHz, while mechanical cracking exhibits frequencies from 250 kHz to 400 kHz. By validation with XRD, the authors were able to correlate the stress mechanisms to i) cracks and particle fragmentation in LMO electrodes and ii) crystalline phase transition in LiAl alloy electrodes. In this way, a detailed evaluation of the underlying electrochemical processes is possible using AE.

AE is also implemented to investigate Si electrodes [157–159]. As described above, Si faces material contractions / expansions of up to 400% upon cycling, therefore it is quite prone to structural stress. Similar to graphite, the highest emission of acoustic energy took place at the first discharge upon de-lithiation of the material [157–159]. By clustering the acoustic events mainly by frequency, the studies [157,159] were also able to assign the AE to specific phenomena. In the case of Yoshida et al. [159] this was done manually by analyzing the fast Fourier transformation (FFT) generated spectra, while Tranchot et al. [157] used an automated strategy. This automated strategy is called principal component analysis (PCA), which can extract, compress, and classify relevant information from AE data sets. It is useful for analysis of complex AE signals like those generated by Si electrodes. Each hit is assigned to a vector whose coordinates correspond to the various AE parameters (see above). The goal is to reduce the dimensionality of the AE data set, by finding a new set of variables smaller than the original one. Those variables are linear combinations of the acoustic parameters of the original set and therefore have no physical meaning; they are called principal components (PC1, PC2, ..., PCn). To obtain those variables an unsupervised iterative statistical clustering procedure is performed. The clustering was not able to classify around 30% of the AE signals. The remaining ones were clustered into three types, with frequencies around 700 kHz and low to medium amplitudes, 400 kHz with medium to high amplitudes and 200 kHz with very low amplitudes. By applying these PCs to the discharge curve, the authors were able to conclude that SEI formation does not cause significant bubbling during first cycles but significant electrode cracking. However, they also state that they are not able to fully differentiate the signals of their clusters and the method should be improved in the future.

6.2. Full cell measurement

On full cell investigation, there are fewer publications. Initially, the applicability of AE for full cells was demonstrated by Komagata et al. [160] on cylindrical 18650 cells. The authors measured AE during discharge of full cells. A newer study by Beganovic and Söffker [161] uses AE on full cells to detect SOH or RUL by AE without having the history of the DUT. In their setup, they use high frequency piezo elements and amplifiers combined with field programmable gate array (FPGA)-based fast data acquisition and computation. The system monitors the AE of the cell continuously during operation. To reduce the dimensions and complexity of the signal, specific parts of same length are taken by windowing the signal and transferring it to the frequency domain by short-term Fourier transformation (STFT). A deeper analysis is then performed, using continuous wavelet transformation (CWT) on the signal to calculate wavelet coefficients. These coefficients then contain the information of the properties of the AE signal in each signal window. Thus, it is observed that the intensity of the AE per window decreases with cycles and thus ageing. For demonstration of the method for SOH and RUL estimation, the data is correlated with the corresponding SOH values (remaining capacity) from conventional electrical measurements. A model was trained using four cells and then a SOH estimation was performed on two cells of the same type. The authors were able to achieve an error of less than 3% and claim their method works without knowing the previous history of the cell. In the validated case using the same cycles continuously this claim is valid; however, the method should also be investigated for different cycle regimes and cell histories as parameters may vary.

6.3. Other methods

A completely different use of AE for monitoring batteries was introduced by Cattin et al. [162]. They applied AE to detect arcs in LIB systems of electric cars. These can occur when the electrical connection becomes loose at some point, e.g. due to vibration or material fatigue. Those arcs can be harmful and lead to fires or other safety-critical conditions. From voltage or current measurements, arcs are difficult to detect, as there are many other transient and disturbing signals. The authors found that the arcs have a significant acoustic spectrum which can be distinguished from other spectra in the car. A demonstrator was built and validated.

6.4. Patents

AE application wise is mostly used for SOH but also for SOC and safety detection. In [163,164] a method for AE integration for cell and module / system level is presented. The working principle is close to the methods described above. Via lookup tables and / or clustering the number and the amplitude of acoustic events are assigned to a SOX. In [165] an apparatus that can monitor AE while putting force on the cell

Table 5
Overview of covered areas of research for AE.

Method	SOC	SOH & Cycling	Intercalation	SEI
Half Cell		[29,157,160]	[29,154,155,157–159,166]	[155,157,166]
Full Cell	[153,163]	[153,156,160,161,163–165]	[156]	

is presented.

6.5. Summary

As indicated in Table 5, AE is not widely applied for SOC estimation but frequently applied for detecting SOH and intercalation phenomena as the materials mostly emmit sound waves when they are degrading. Especially the ability to listen to electrode cracking made it a popular method for both investigating state of the art materials, but also next generation materials i.e. Si anodes in this case.

7. Integration in battery systems

For integration into a battery pack, sensors need different properties than for laboratory application. Stationary equipment also has other demands than mobile or automotive devices, but in general sensor systems for application should be i) inexpensive, ii) small and light, iii) robust, and iv) have a low power consumption. Compared to laboratory equipment demands on accuracy and resolution usually are lower. Considering these points, not all methods discussed above are equally suitable for integration. While dilation measurement with common contact 1-D technology is difficult to place in a battery pack because of limited space, and optical technology is even more difficult to integrate - the latter is also too expensive - the suitability of the eddy current technique for integration was demonstrated by Knobloch et al. [71]. They also performed the integration of a force sensor. Another practical eddy current implementation was demonstrated in [54]. The authors processed the signal of the eddy current sensor used for measurement of dilation with a high-resolution 28-bit automotive chip (LDC1612, Texas Instrument, USA). The chip is commonly used to convert signals from push or slider buttons but works also well in this type of application. With its I2C communication protocol, it can be integrated in common BMS designs. Another method for determining dilation is based on measuring the change in capacity between two plates caused by a variation in the distance between these plates. For two parallel plates the capacity C (eq. 8) is defined by

$$C = \epsilon \cdot \frac{A}{d}, \tag{8}$$

with ϵ (F/m) being the permittivity, A (m^2) the surface area and d (m) the distance between the two plates. No work has been found that uses this concept on commercial LIB cells, which is surprising as laboratory grade dilatometers used on batteries for material investigation (e.g. [167]) work on this principle, and it has been a common method for displacement measurements for decades [168]. Bohn et al. [72] claim that interferometer setups are well suited for miniaturization and thus could be used as additional source of information for BMS in applications like drones.

Strain and force, as also the number of patents for application implies (see sec. 3.2), has high potential for implementation. Fiber optic strain and temperature measurement offer promising possibilities and there are already existing commercial solutions [169,170], but due to their still costly technology they are yet not suitable for commercial BMS for broader use (common OSI start from over one thousand USD and then still fibers and auxiliaries are needed). However, in [106] a cost estimation is given, stating that the cost for a full add-on to a BMS can be reduced to USD 100 $ to 500 $ depending on the size of the system. RFSG offer cheaper solutions for strain measurements. In [112] an approach with monitoring the strain of a full module with just one strain sensor is presented. This brings cost and space requirements further down. Still, todays OSI require high operational power and are bulky.

EMA does not play a role for integration in a battery pack but can support the design phase by determining important mechanical parameters.

By using piezo disc actuators, a small and low-cost approach for US measurement can be realized. In [9] it is shown that receiver and transmitter for ultrasonic based SOX estimation methods can be implemented inexpensively and with low effort if there are unused general inputs and outputs (GPIO) or other suitable converter pins on the BMS controller. There are already systems on the market [171,172].

There are several patents on AE also for application (see Section 6). In [160,161] practical methods for SOH estimation are presented. The drawback of AE is that it is not really suited for SOC or other estimations beside SOH - see Table 5. Laboratory equipment for measuring AE is expensive. Literature for low-effort implementation for LIB was not found for this review but the use of FPGA like in [161] points in the right direction.

Koch et al. [173] compared the ability of various sensors to detect a thermal runaway for implementation. They showed that a piezo-resistive force sensor between two cells reacted very quickly before a thermal runaway. Due to gas production inside the cell and the subsequent expansion that takes place shortly before a thermal runaway the force sensor was able to detect the thermal runaway before the mounted gas sensor. In [173] it is also mentioned that the force sensors may be useless for thermal runaway detection if compression pads (soft structure) are placed between the cells. However, they showed that while every sensor type was able to detect a thermal runaway, each one has its advantages and disadvantages. It is suggested to use a combination of two or more sensors to build a thermal runaway detection system.

A different approach for measuring various mechanical influences and impacts was presented by Hu et al. [174]. The authors developed a surface sensor which bases on spatially distributed piezoelectric, pyroelectric and thin film transistor elements. As such it can detect and localize quasi-static impacts like swelling, dynamic impacts like mechanical forces and overheating of the cell. The concept was demonstrated with a 50 mm x 50 mm sensor on a pouch cell of the same size running several safety critical scenarios. It was shown that the sensor is suited to find hazards due to mechanical changes before other parameters like cell voltage show a reaction.

Table 6 summarizes the statements above and compares the estimated costs and the integrability of the various mechanical state determination methods based on the necessary sensors and electronics. EMA is not discussed in this table, as it is not intended to be

Table 6
Feasibility of concept for implementation in a battery system with BMS.

Method	Sensor	Cost	Integrability	SOX Indicator	Power Consumption	Size
Dilatometry	Dial indicator	high	difficult	SOC, SOH, Li-plating det.	low	large
	Inductance sensor	moderate	in development		low	small
	3D-Scanning	critical	difficult		high	large
	Optical interferometer	crictical	difficult		high	large
Strain/Force	RFSG	high	feasible	SOC, Thermal Runaway, temperature	low	small
	Fiber-optic sensor	high	difficult (in cell), feasible (surface)	measuring	high	large
	Resistive pressure sensor	low	feasible		low	small
Acoustic Emission	Piezoelectric AE	high	feasible	SOH, Arc detection	low	medium
Ultrasonic	Ceramic Piezo element	low	commercialised	SOC, SOH, Li-plating det.	low	small

implemented in an application.

Deep learning and statistical approaches, which are part of the data driven estimation methods [175–177] are usually also applicable to the mechanical methods discussed in this review. For example, Davies et al. [136] used a machine learning technique to estimate the SOC based on ultrasonic data. To train the network they used the TOF, the signal amplitude, and the cell voltage as an input vector. The authors used two cells to train the network and a third independent cell was used to test the resultant network for SOC prediction. Important to mention is that, unlike the coulomb counting method or other filter-based methods, the proposed algorithm is history independent, which means that no previous data is necessary to estimate the SOC. Such hybrid approaches that combine current and voltage data with other sensor data won by mechanical measurements can significantly improve SOC or SOH estimation.

8. Discussion and conclusion

The investigation showed that dilatometric methods are widely employed for investigation of LIB cells. One very popular approach is the measurement with 1-D contact sensors. With this, a wide variety of phenomena like Li-staging of graphite, thermal expansion and relaxation, full cell expansion, and Li plating have been investigated, and methods were developed for scenarios like fast charging with minimized harm to the electrodes. There were many contributions to the understanding of internal phenomena of state-of-the-art LIB cells, but also for promising materials like Si anodes. Methods enabling spatially distributed analysis of the expansion of the cells were presented. No methods for measurements on modules or systems were found. Interestingly, there is a certain lack of studies on ageing as well as on safety or abuse conditions apart from Li plating (Table 1). Integration in a battery system is difficult. In summary dilatometry is popular and useful for laboratory use but less for application, since integration in battery system is difficult.

This is different for the second expansion-based methods. Force, surface strain, and internal strain are widely applied on SOC and SOH estimation, as well as to determine current and temperature dependencies of cells. Surface strain is also often used for abusive condition. Until now, most research was done in the laboratory, but the number of patents, concepts for estimators and suitability for implementation (Table 6) point towards to be useful and hence towards future practical application. Proof of concept for implementation in modules was already done in a few publications for all three types of strain / force methods.

EMA is used to derive eigenfrequencies and modes via FRF. There is no real application for SOX estimation, but rather for improving the mechanical design of battery systems with the results of EMA. Current literature is inconclusive about SOX dependencies for EMA. Further research is needed.

US sensing is mainly applied for SOC and SOH measurement on cells until now. But also influences of temperature, C-rates, and abusive condition have already been examined. A validation for cells in module or system like configurations is as yet missing. The successful implementation on hard case prismatic cells, however, shows that the method is also suited for more rigid casings and thus could potentially work in constraint application too. Both through-body and surface waves concepts have shown promising results. Because of the low-cost demonstrators already built and the beginning commercialization, the technique is likely to find its way into applications.

AE is seldom used on full cells, and no publication on commercial cells was found. It is very popular for SOH estimation because it allows to observe in-operando the degradation of materials with high volume changes, like Si. So far it is a pure laboratory method.

Additional sensors also are in development mostly for application to identify hazards to the cell. They do not play a major role in laboratory measurements at the moment.

As this review shows, non-destructive mechanical methods for investigation of LIB are increasingly found in research. Often, these methods are less costly than common approaches providing information about material behaviour like imaging methods, but requiring less measurement time than e.g. EIS measurements and still enabling fully in-situ and in-operando investigation of LIB. Thus, they have contributed a lot to the understanding of LIB behaviour in the laboratory also by providing additional information to standard measurements. Knowledge and understanding were created regarding material contraction in general and due to variation in temperature and in C-rates in particular, irreversible expansion due to (SEI) layer formation and deterioration of internal structure, and abusive conditions like plating and thermal- and electrical- out-of-boundary conditions. Some methods additionally are likely to find their way into applications, as they can improve SOX estimation significantly. They work best in combination with traditional measurement concepts like voltage and current measurement, so they are not likely to replace those. Thus, cost for the sensor-systems still needs to be decreased to allow for integration in such cost-sensitive applications like those found in the battery sector.

CRediT authorship contribution statement

Hartmut Popp: Conceptualization, Formal analysis, Funding acquisition, Visualization, Writing - original draft, Writing - review & editing. **Markus Koller:** Formal analysis, Co-Writing Section “Implementation”- original draft, Writing - review & editing. **Marcus Jahn:** Conceptualization, Supervision, Writing Section “Other relevant phenomena”- original draft, Writing - review & editing. **Alexander Bergmann:** Conceptualization, Supervision, Writing - review & editing.

Declaration of Competing Interest

The authors declare that they have no known competing financial interests or personal relationships that could have appeared to influence the work reported in this paper.

Acknowledgements

The research leading to these results has received funding from the Austrian Research Promotion Agency (FFG) under grant number #865148.

The authors want to express their gratitude to Dr. Irina Gocheva and Mr. Hansjörg Kapeller for scientific discussion on earlier versions of this manuscript, Mr. Gregor Glanz for the support with figures, and Ms. Jacqueline Winter and Mr. Boschidar Ganev for linguistic proofreading and corrections.

References

[1] T. Placke, R. Kloepsch, S. Dühnen, M. Winter, Lithium ion, lithium metal, and alternative rechargeable battery technologies: the odyssey for high energy density, J. Solid State Electrochem. 21 (7) (2017) 1939–1964, https://doi.org/10.1007/s10008-017-3610-7.

[2] G.E. Blomgren, The development and future of lithium ion batteries, J Electrochem Soc 164 (1) (2017) A5019–A5025, https://doi.org/10.1149/2.0251701jes.

[3] Y. Ding, Z.P. Cano, A. Yu, J. Lu, Z. Chen, Automotive li-ion batteries: current status and future perspectives, Electrochemical Energy Reviews 2 (1) (2019) 1–28, https://doi.org/10.1007/s41918-018-0022-z.

[4] G. Zubi, R. Dufo-López, M. Carvalho, G. Pasaoglu, The lithium-ion battery: state of the art and future perspectives, Renewable Sustainable Energy Rev. 89 (2018) 292–308, https://doi.org/10.1016/j.rser.2018.03.002.

[5] R. Xiong, J. Cao, Q. Yu, H. He, F. Sun, Critical review on the battery state of charge estimation methods for electric vehicles, IEEE Access 6 (2018) 1832–1843, https://doi.org/10.1109/ACCESS.2017.2780258.

[6] W. Waag, C. Fleischer, D.U. Sauer, Critical review of the methods for monitoring of lithium-ion batteries in electric and hybrid vehicles, J Power Sources 258 (2014) 321–339, https://doi.org/10.1016/j.jpowsour.2014.02.064.

[7] P. Shrivastava, T.K. Soon, M.Y.I.B. Idris, S. Mekhilef, Overview of model-based online state-of-charge estimation using Kalman filter family for lithium-ion

batteries, Renewable Sustainable Energy Rev. 113 (2019) 109233, https://doi.org/10.1016/j.rser.2019.06.040.
[8] H. Tian, P. Qin, K. Li, Z. Zhao, A review of the state of health for lithium-ion batteries: research status and suggestions, J Clean Prod (2020) 120813, https://doi.org/10.1016/j.jclepro.2020.120813.
[9] H. Popp, M. Koller, S. Keller, G. Glanz, R. Klambauer, A. Bergmann, State estimation approach of lithium-ion batteries by simplified ultrasonic time-of-flight measurement, IEEE Access 7 (2019) 170992–171000, https://doi.org/10.1109/ACCESS.2019.2955556.
[10] M. Loveridge, G. Remy, N. Kourra, R. Genieser, A. Barai, M. Lain, Y. Guo, M. Amor-Segan, M. Williams, T. Amietszajew, M. Ellis, R. Bhagat, D. Greenwood, Looking deeper into the galaxy (note 7), Batteries 4 (1) (2018) 3, https://doi.org/10.3390/batteries4010003.
[11] V. Müller, R.-G. Scurtu, M. Memm, M.A. Danzer, M. Wohlfahrt-Mehrens, Study of the influence of mechanical pressure on the performance and aging of lithium-ion battery cells, J Power Sources 440 (2019) 227148, https://doi.org/10.1016/j.jpowsour.2019.227148.
[12] A.S. Mussa, M. Klett, G. Lindbergh, R.W. Lindström, Effects of external pressure on the performance and ageing of single-layer lithium-ion pouch cells, J Power Sources 385 (2018) 18–26, https://doi.org/10.1016/j.jpowsour.2018.03.020.
[13] J.M. Hooper, J. Marco, Characterising the in-vehicle vibration inputs to the high voltage battery of an electric vehicle, J Power Sources 245 (2014) 510–519, https://doi.org/10.1016/j.jpowsour.2013.06.150.
[14] J.M. Hooper, J. Marco, Experimental modal analysis of lithium-ion pouch cells, J Power Sources 285 (2015) 247–259, https://doi.org/10.1016/j.jpowsour.2015.03.098.
[15] B. Xia, F. Liu, C. Xu, Y. Liu, Y. Lai, W. Zheng, W. Wang, Experimental and simulation modal analysis of a prismatic battery module, Energies 13 (8) (2020) 2046, https://doi.org/10.3390/en13082046.
[16] J. Zhu, T. Wierzbicki, W. Li, A review of safety-focused mechanical modeling of commercial lithium-ion batteries, J Power Sources 378 (2018) 153–168, https://doi.org/10.1016/j.jpowsour.2017.12.034.
[17] G. Kermani, E. Sahraei, Review: characterization and modeling of the mechanical properties of lithium-ion batteries, Energies 10 (11) (2017) 1730, https://doi.org/10.3390/en10111730.
[18] V. Ruiz, A. Pfrang, A. Kriston, N. Omar, P. Van den Bossche, L. Boon-Brett, A review of international abuse testing standards and regulations for lithium ion batteries in electric and hybrid electric vehicles, Renewable Sustainable Energy Rev. 81 (2018) 1427–1452, https://doi.org/10.1016/j.rser.2017.05.195.
[19] J.A. Turner, S. Allu, S.B. Gorti, S. Kalnaus, A. Kumar, D.T. Lebrun-Grandie, S. Pannala, S. Simunovic, S.R. Slattery, H. Wang, Crash Models for Advanced Automotive Batteries: A Review of the Current State of the Art, Technical Report, (2015), https://doi.org/10.2172/1302885.
[20] L. Greve, C. Fehrenbach, Mechanical testing and macro-mechanical finite element simulation of the deformation, fracture, and short circuit initiation of cylindrical lithium ion battery cells, J Power Sources 214 (2012) 377–385, https://doi.org/10.1016/j.jpowsour.2012.04.055.
[21] G. Kermani, E. Sahraei, Dynamic impact response of lithium-ion batteries, constitutive properties and failure model, RSC Adv 9 (5) (2019) 2464–2473, https://doi.org/10.1039/C8RA08898E.
[22] H. Wang, A. Kumar, S. Simunovic, S. Allu, S. Kalnaus, J.A. Turner, J.C. Helmers, E.T. Rules, C.S. Winchester, P. Gorney, Progressive mechanical indentation of large-format Li-ion cells, J Power Sources 341 (2017) 156–164, https://doi.org/10.1016/j.jpowsour.2016.11.094.
[23] X. Zhang, T. Wierzbicki, Characterization of plasticity and fracture of shell casing of lithium-ion cylindrical battery, J Power Sources 280 (2015) 47–56, https://doi.org/10.1016/j.jpowsour.2015.01.077.
[24] D. Liu, Z. Shadike, R. Lin, K. Qian, H. Li, K. Li, S. Wang, Q. Yu, M. Liu, S. Ganapathy, X. Qin, Q. Yang, M. Wagemaker, F. Kang, X. Yang, B. Li, Review of recent development of in situ/operando characterization techniques for lithium battery research, Adv. Mater. 31 (28) (2019) 1806620, https://doi.org/10.1002/adma.201806620.
[25] J. Conder, C. Marino, P. Novák, C. Villevieille, Do imaging techniques add real value to the development of better post-Li-ion batteries? Journal of Materials Chemistry A 6 (8) (2018) 3304–3327, https://doi.org/10.1039/C7TA10622J.
[26] B. Raj, T. Jayakumar, M. Thavasimuthu, Practical non-destructive testing, 2. ed, Woodhead Publ, Cambridge, 2002. OCLC: 248861527
[27] R. Halmshaw, Introduction to the non-destructive testing of welded joints, 2nd ed, Abington, Cambridge, 1996. OCLC: 255311890
[28] A. Mukhopadhyay, B.W. Sheldon, Deformation and stress in electrode materials for Li-ion batteries, Prog Mater Sci 63 (2014) 58–116, https://doi.org/10.1016/j.pmatsci.2014.02.001.
[29] K. Rhodes, N. Dudney, E. Lara-Curzio, C. Daniel, Understanding the degradation of silicon electrodes for lithium-ion batteries using acoustic emission, J Electrochem Soc 157 (12) (2010) A1354, https://doi.org/10.1149/1.3489374.
[30] K. Fröhlich, Next generation HE-NMC cathodes for advanced lithium-ion batteries, Vienna University of Technology, Vienna, Austria, 2018 Ph.D. thesis.
[31] A. Barr, B. Deguilhem, S. Grolleau, M. Grard, F. Suard, D. Riu, A review on lithium-ion battery ageing mechanisms and estimations for automotive applications, J Power Sources 241 (2013) 680–689, https://doi.org/10.1016/j.jpowsour.2013.05.040.
[32] R. Schröder, M. Aydemir, G. Seliger, Comparatively assessing different shapes of lithium-ion battery cells, Procedia Manuf. 8 (2017) 104–111, https://doi.org/10.1016/j.promfg.2017.02.013.
[33] W. Li, Y. Xia, J. Zhu, H. Luo, State-of-charge dependence of mechanical response of lithium-ion batteries: a result of internal stress, J Electrochem Soc 165 (7) (2018) A1537–A1546, https://doi.org/10.1149/2.0051809jes.
[34] X. Cheng, M. Pecht, In situ stress measurement techniques on li-ion battery electrodes: a review, Energies 10 (5) (2017) 591, https://doi.org/10.3390/en10050591.
[35] R. Kanno, Y. Takeda, T. Ichikawa, K. Nakanishi, O. Yamamoto, Carbon as negative electrodes in lithium secondary cells, J Power Sources 26 (3–4) (1989) 535–543, https://doi.org/10.1016/0378-7753(89)80175-2.
[36] J.R. Dahn, Phase diagram of Li x C 6, Physical Review B 44 (17) (1991) 9170–9177, https://doi.org/10.1103/PhysRevB.44.9170.
[37] Y. Qi, H. Guo, L.G. Hector, A. Timmons, Threefold increase in the youngs modulus of graphite negative electrode during lithium intercalation, J Electrochem Soc 157 (5) (2010) A558, https://doi.org/10.1149/1.3327913.
[38] A.J. Louli, J. Li, S. Trussler, C.R. Fell, J.R. Dahn, Volume, pressure and thickness evolution of li-ion pouch cells with silicon-composite negative electrodes, J Electrochem Soc 164 (12) (2017) A2689–A2696, https://doi.org/10.1149/2.1691712jes.
[39] V.A. Sethuraman, L.J. Hardwick, V. Srinivasan, R. Kostecki, Surface structural disordering in graphite upon lithium intercalation/deintercalation, J Power Sources 195 (11) (2010) 3655–3660, https://doi.org/10.1016/j.jpowsour.2009.12.034.
[40] D. Sauerteig, S. Ivanov, H. Reinshagen, A. Bund, Reversible and irreversible dilation of lithium-ion battery electrodes investigated by in-situ dilatometry, J Power Sources 342 (2017) 939–946, https://doi.org/10.1016/j.jpowsour.2016.12.121.
[41] K. Ariyoshi, R. Yamato, T. Ohzuku, Zero-strain insertion mechanism of Li[Li1/3Ti5/3]O4 for advanced lithium-ion (shuttlecock) batteries, Electrochim. Acta 51 (6) (2005) 1125–1129, https://doi.org/10.1016/j.electacta.2005.05.053.
[42] J. Shu, Electrochemical behavior and stability of Li4Ti5O12 in a broad voltage window, J. Solid State Electrochem. 13 (10) (2009) 1535–1539, https://doi.org/10.1007/s10008-008-0723-z.
[43] L. Liu, F. Xie, J. Lyu, T. Zhao, T. Li, B.G. Choi, Tin-based anode materials with well-designed architectures for next-generation lithium-ion batteries, J Power Sources 321 (2016) 11–35, https://doi.org/10.1016/j.jpowsour.2016.04.105.
[44] Z. Liu, Y. Qi, Y.X. Lin, L. Chen, P. Lu, L.Q. Chen, Interfacial study on solid electrolyte interphase at li metal anode: implication for li dendrite growth, J Electrochem Soc 163 (3) (2016) A592–A598, https://doi.org/10.1149/2.0151605jes.
[45] W. Zhang, H.-C. Yu, L. Wu, H. Liu, A. Abdellahi, B. Qiu, J. Bai, B. Orvananos, F.C. Strobridge, X. Zhou, Z. Liu, G. Ceder, Y. Zhu, K. Thornton, C.P. Grey, F. Wang, Localized concentration reversal of lithium during intercalation into nanoparticles, Sci Adv 4 (1) (2018) eaao2608, https://doi.org/10.1126/sciadv.aao2608.
[46] A. Rezqita, A.-R. Kathribail, J. Kahr, M. Jahn, Analysis of degradation of Si/Carbon||LiNi $_{0.5}$Mn $_{0.3}$Co $_{0.2}$O$_2$full cells: effect of prelithiation, J Electrochem Soc 166 (3) (2019) A5483–A5488, https://doi.org/10.1149/2.0671903jes.
[47] A. Samba, N. Omar, H. Gualous, Y. Firouz, P. Van den Bossche, J. Van Mierlo, T.I. Boubekeur, Development of an advanced two-dimensional thermal model for large size lithium-ion pouch cells, Electrochim. Acta 117 (2014) 246–254, https://doi.org/10.1016/j.electacta.2013.11.113.
[48] S. Goutam, J.-M. Timmermans, N. Omar, P. Bossche, J. Van Mierlo, Comparative study of surface temperature behavior of commercial li-ion pouch cells of different chemistries and capacities by infrared thermography, Energies 8 (8) (2015) 8175–8192, https://doi.org/10.3390/en8088175.
[49] T. Hettensheimer, A. Thielmann, C. Neef, K.-C. Möller, M. Wolter, V. Lorentz, M. Gepp, M. Wenger, T. Prill, J. Zausch, P. Kitzler, J. Montnacher, M. Miller, M. Hagen, P. Franz, J. Tübke, Entwicklungsperspektiven für Zellformate von Lithium-Ionen-Batterien in der Elektromobilität (2017).
[50] D. Andre, S.-J. Kim, P. Lamp, S.F. Lux, F. Maglia, O. Paschos, B. Stiaszny, Future generations of cathode materials: an automotive industry perspective, Journal of Materials Chemistry A 3 (13) (2015) 6709–6732, https://doi.org/10.1039/C5TA00361J.
[51] W. Li, Y.-G. Cho, W. Yao, Y. Li, A. Cronk, R. Shimizu, M.A. Schroeder, Y. Fu, F. Zou, V. Battaglia, A. Manthiram, M. Zhang, Y.S. Meng, Enabling high areal capacity for Co-free high voltage spinel materials in next-generation Li-ion batteries, J Power Sources 473 (2020) 228579, https://doi.org/10.1016/j.jpowsour.2020.228579.
[52] H. Popp, N. Zhang, M. Jahn, M. Arrinda, S. Ritz, M. Faber, D.U. Sauer, P. Azais, I. Cendoya, Ante-mortem analysis, electrical, thermal, and ageing testing of state-of-the-art cylindrical lithium-ion cells, e & i Elektrotechnik und Informationstechnik (2020), https://doi.org/10.1007/s00502-020-00814-9.
[53] M. Lewerenz, D.U. Sauer, Evaluation of cyclic aging tests of prismatic automotive LiNiMnCoO2-Graphite cells considering influence of homogeneity and anode overhang, Journal of Energy Storage 18 (2018) 421–434, https://doi.org/10.1016/j.est.2018.06.003.
[54] F. Grimsmann, T. Gerbert, F. Brauchle, A. Gruhle, J. Parisi, M. Knipper, Determining the maximum charging currents of lithium-ion cells for small charge quantities, J Power Sources 365 (2017) 12–16, https://doi.org/10.1016/j.jpowsour.2017.08.044.
[55] V. Zinth, C. von Lüders, M. Hofmann, J. Hattendorff, I. Buchberger, S. Erhard, J. Rebelo-Kornmeier, A. Jossen, R. Gilles, Lithium plating in lithium-ion batteries at sub-ambient temperatures investigated by in situ neutron diffraction, J Power Sources 271 (2014) 152–159, https://doi.org/10.1016/j.jpowsour.2014.07.168.
[56] M. Winter, G.H. Wrodnigg, J.O. Besenhard, W. Biberacher, P. Novák, Dilatometric investigations of graphite electrodes in nonaqueous lithium battery electrolytes, J Electrochem Soc 147 (7) (2000) 2427, https://doi.org/10.1149/1.1393548.
[57] J.H. Lee, H.M. Lee, S. Ahn, Battery dimensional changes occurring during charge/

discharge cycles thin rectangular lithium ion and polymer cells, J Power Sources 119–121 (2003) 833–837, https://doi.org/10.1016/S0378-7753(03)00281-7.
[58] M. Bauer, M. Wachtler, H. Stwe, J.V. Persson, M.A. Danzer, Understanding the dilation and dilation relaxation behavior of graphite-based lithium-ion cells, J Power Sources 317 (2016) 93–102, https://doi.org/10.1016/j.jpowsour.2016.03.078.
[59] B. Bitzer, A. Gruhle, A new method for detecting lithium plating by measuring the cell thickness, J Power Sources 262 (2014) 297–302, https://doi.org/10.1016/j.jpowsour.2014.03.142.
[60] F. Grimsmann, F. Brauchle, T. Gerbert, A. Gruhle, M. Knipper, J. Parisi, Hysteresis and current dependence of the thickness change of lithium-ion cells with graphite anode, Journal of Energy Storage 12 (2017) 132–137, https://doi.org/10.1016/j.est.2017.04.006.
[61] R. Fu, M. Xiao, S.-Y. Choe, Modeling, validation and analysis of mechanical stress generation and dimension changes of a pouch type high power Li-ion battery, J Power Sources 224 (2013) 211–224, https://doi.org/10.1016/j.jpowsour.2012.09.096.
[62] B. Rieger, S.V. Erhard, K. Rumpf, A. Jossen, A new method to model the thickness change of a commercial pouch cell during discharge, J Electrochem Soc 163 (8) (2016) A1566–A1575, https://doi.org/10.1149/2.0441608jes.
[63] B. Rieger, S. Schlueter, S. Erhard, J. Schmalz, G. Reinhart, A. Jossen, Multi-scale investigation of thickness changes in a commercial pouch type lithium-ion battery, Journal of Energy Storage 6 (2016) 213–221, https://doi.org/10.1016/j.est.2016.01.006.
[64] M. Bauer, B. Rieger, S. Schindler, P. Keil, M. Wachtler, M.A. Danzer, A. Jossen, Multi-phase formation induced by kinetic limitations in graphite-based lithium-ion cells: analyzing the effects on dilation and voltage response, Journal of Energy Storage 10 (2017) 1–10, https://doi.org/10.1016/j.est.2016.11.006.
[65] K.-Y. Oh, J.B. Siegel, L. Secondo, S.U. Kim, N.A. Samad, J. Qin, D. Anderson, K. Garikipati, A. Knobloch, B.I. Epureanu, C.W. Monroe, A. Stefanopoulou, Rate dependence of swelling in lithium-ion cells, J Power Sources 267 (2014) 197–202, https://doi.org/10.1016/j.jpowsour.2014.05.039.
[66] K.-Y. Oh, B.I. Epureanu, A novel thermal swelling model for a rechargeable lithium-ion battery cell, J Power Sources 303 (2016) 86–96, https://doi.org/10.1016/j.jpowsour.2015.10.085.
[67] F.B. Spingler, W. Wittmann, J. Sturm, B. Rieger, A. Jossen, Optimum fast charging of lithium-ion pouch cells based on local volume expansion criteria, J Power Sources 393 (2018) 152–160, https://doi.org/10.1016/j.jpowsour.2018.04.095.
[68] P. Leung, C. Moreno, I. Masters, S. Hazra, B. Conde, M. Mohamed, R. Dashwood, R. Bhagat, Real-time displacement and strain mappings of lithium-ion batteries using three-dimensional digital image correlation, J Power Sources 271 (2014) 82–86, https://doi.org/10.1016/j.jpowsour.2014.07.184.
[69] A.J. Knobloch, Y.A. Plotnikov, C.J. Kapusta, J.H. Karp, Y. Lin, Battery cell health monitoring using eddy current sensing, 2015, Library Catalog: Google Patents.
[70] Y. Plotnikov, J. Karp, A. Knobloch, C. Kapusta, D. Lin, Eddy current sensor for in-situ monitoring of swelling of Li-ion prismatic cells, Boise, Idaho, 434–442, 2015, pp. 10.1063/1.4914639.
[71] A. Knobloch, J. Karp, Y. Plotnikov, C. Kapusta, J. Siegel, N. Samad, A. Stefanopoulou, Novel thin temperature and expansion sensors for li-ion battery monitoring, 2017 IEEE SENSORS, IEEE, Glasgow, 2017, pp. 1–3, https://doi.org/10.1109/ICSENS.2017.8234066.
[72] G. Bohn, J. Taub, A. Linke, S. Bayer, D. Oeser, A. Ziegler, P. Ettl, A. Ackva, High-resolution interferometric measurement of thickness change on a lithium-ion pouch battery, IOP Conference Series: Earth and Environmental Science 281 (2019) 012030, https://doi.org/10.1088/1755-1315/281/1/012030.
[73] K. Alzahrani, D. Burton, F. Lilley, M. Gdeisat, F. Bezombes, M. Qudeisat, Absolute distance measurement with micrometer accuracy using a Michelson interferometer and the iterative synthetic wavelength principle, Opt Express 20 (5) (2012) 5658, https://doi.org/10.1364/OE.20.005658.
[74] B.J. Koch, R.S. Conell, Method and system for determining a state of charge of a battery, 2012, Library Catalog: Google Patents.
[75] D.-S. Yoon, S.-H. Kim, J.-H. Kim, J.-H. Lee, Device and method for measuring thickness of secondary battery cell, 2017, Library Catalog: Google Patents.
[76] J.E. Hopkins, Measurement fixture for a battery cell, 2018.
[77] C. Xiaolin, Automatic detection apparatus for be used for lithium cell, 2018.
[78] J. Yuanyuan, Y. Yi, H. Jun, Small square lithium battery high-precision thickness measuring device, 2019.
[79] J.-G. Yoon, Thickness change measurement apparatus for electrode of secondary battery and secondary battery mounting the same, 2019, Library Catalog: Google Patents.
[80] P. Mohtat, S. Lee, J.B. Siegel, A.G. Stefanopoulou, Towards better estimability of electrode-specific state of health: decoding the cell expansion, J Power Sources 427 (2019) 101–111, https://doi.org/10.1016/j.jpowsour.2019.03.104.
[81] K.P. Birke, Modern Battery Engineering: A Comprehensive Introduction, World Scientific, 2019. Google-Books-ID: heaWDwAAQBAJ
[82] R. Hickey, T.M. Jahns, Measuring Individual Battery Dimensional Changes for State-of-Charge Estimation using Strain Gauge Sensors, 2019 IEEE Energy Conversion Congress and Exposition (ECCE), IEEE, Baltimore, MD, USA, 2019, pp. 2460–2465, https://doi.org/10.1109/ECCE.2019.8912578.
[83] V. Sethuraman, N. Van Winkle, D. Abraham, A. Bower, P. Guduru, Real-time stress measurements in lithium-ion battery negative-electrodes, J Power Sources 206 (2012) 334–342, https://doi.org/10.1016/j.jpowsour.2012.01.036.
[84] M. Majima, S. Ujiie, E. Yagasaki, K. Koyama, S. Inazawa, Development of long life lithium ion battery for power storage, J Power Sources 101 (1) (2001) 53–59, https://doi.org/10.1016/S0378-7753(01)00554-7.
[85] X. Wang, Y. Sone, S. Kuwajima, In situ investigation of the volume change in li-ion cell with charging and discharging, J Electrochem Soc 151 (2) (2004) A273, https://doi.org/10.1149/1.1635827.
[86] X. Wang, Y. Sone, G. Segami, H. Naito, C. Yamada, K. Kibe, Understanding volume change in lithium-ion cells during charging and discharging using in situ measurements, J Electrochem Soc 154 (1) (2007) A14, https://doi.org/10.1149/1.2386933.
[87] W. Zhang, D. Schröder, T. Arlt, I. Manke, R. Koerver, R. Pinedo, D.A. Weber, J. Sann, W.G. Zeier, J. Janek, (Electro)chemical expansion during cycling: monitoring the pressure changes in operating solid-state lithium batteries, Journal of Materials Chemistry A 5 (20) (2017) 9929–9936, https://doi.org/10.1039/C7TA02730C.
[88] J. Cannarella, C.B. Arnold, State of health and charge measurements in lithium-ion batteries using mechanical stress, J Power Sources 269 (2014) 7–14, https://doi.org/10.1016/j.jpowsour.2014.07.003.
[89] J. Cannarella, C.B. Arnold, Stress evolution and capacity fade in constrained lithium-ion pouch cells, J Power Sources 245 (2014) 745–751, https://doi.org/10.1016/j.jpowsour.2013.06.165.
[90] J. Cannarella, C.Z. Leng, C.B. Arnold, On the coupling between stress and voltage in lithium-ion pouch cells, Baltimore, Maryland, USA, 91150K, 2014, p. 10.1117/12.2055152.
[91] S. Mohan, Y. Kim, A.G. Stefanopoulou, On Improving Battery State of Charge Estimation Using Bulk Force Measurements, Control of Robotic Systems, American Society of Mechanical Engineers, Columbus, Ohio, USA, 2015, https://doi.org/10.1115/DSCC2015-9966. V001T13A010
[92] M.A. Figueroa-Santos, J.B. Siegel, A.G. Stefanopoulou, Leveraging cell expansion sensing in state of charge estimation: practical considerations, Energies 13 (10) (2020) 2653, https://doi.org/10.3390/en13102653.
[93] N.A. Samad, Y. Kim, J.B. Siegel, A.G. Stefanopoulou, Battery capacity fading estimation using a force-based incremental capacity analysis, J Electrochem Soc 163 (8) (2016) A1584–A1594, https://doi.org/10.1149/2.0511608jes.
[94] Y. Kim, N.A. Samad, K.-Y. Oh, J.B. Siegel, B.I. Epureanu, A.G. Stefanopoulou, Estimating state-of-charge imbalance of batteries using force measurements, 2016 American Control Conference (ACC), IEEE, Boston, MA, USA, 2016, pp. 1500–1505, https://doi.org/10.1109/ACC.2016.7525128.
[95] L. Feng, S. Zhou, Y. Li, Y. Wang, Q. Zhao, C. Luo, G. Wang, K. Yan, Experimental investigation of thermal and strain management for lithium-ion battery pack in heat pipe cooling, Journal of Energy Storage 16 (2018) 84–92, https://doi.org/10.1016/j.est.2018.01.001.
[96] C. Campanella, A. Cuccovillo, C. Campanella, A. Yurt, V. Passaro, Fibre bragg grating based strain sensors: review of technology and applications, Sensors 18 (9) (2018) 3115, https://doi.org/10.3390/s18093115.
[97] L.W. Sommer, A. Raghavan, P. Kiesel, B. Saha, T. Staudt, A. Lochbaum, A. Ganguli, C.-J. Bae, M. Alamgir, Embedded fiber optic sensing for accurate state estimation in advanced battery management systems, MRS Proceedings 1681 (2014) mrss14–1681–q01–03, , https://doi.org/10.1557/opl.2014.560.
[98] L.W. Sommer, P. Kiesel, A. Ganguli, A. Lochbaum, B. Saha, J. Schwartz, C.-J. Bae, M. Alamgir, A. Raghavan, Fast and slow ion diffusion processes in lithium ion pouch cells during cycling observed with fiber optic strain sensors, J Power Sources 296 (2015) 46–52, https://doi.org/10.1016/j.jpowsour.2015.07.025.
[99] Z. Gong, Z. Xiang, X. OuYang, J. Zhang, N. Lau, J. Zhou, C.C. Chan, Wearable fiber optic technology based on smart textile: a review, Materials 12 (20) (2019) 3311, https://doi.org/10.3390/ma12203311.
[100] J. Meyer, A. Nedjalkov, A. Doering, M. Angelmahr, W. Schade, Fiber optical sensors for enhanced battery safety, Baltimore, Maryland, United States, 94800Z, 2015, 10.1117/12.2183325.
[101] L.K. Willenberg, P. Dechent, G. Fuchs, D.U. Sauer, E. Figgemeier, High-precision monitoring of volume change of commercial lithium-ion batteries by using strain gauges, Sustainability 12 (2) (2020) 557, https://doi.org/10.3390/su12020557.
[102] L.K. Willenberg, P. Dechent, G. Fuchs, M. Teuber, M. Eckert, M. Graff, N. Kürten, D.U. Sauer, E. Figgemeier, The development of jelly roll deformation in 18650 lithium-ion batteries at low state of charge, J Electrochem Soc (2020), https://doi.org/10.1149/1945-7111/aba96d.
[103] M. Nascimento, M. Ferreira, J. Pinto, Simultaneous sensing of temperature and bi-directional strain in a prismatic Li-ion battery, Batteries 4 (2) (2018) 23, https://doi.org/10.3390/batteries4020023.
[104] C.-J. Bae, A. Manandhar, P. Kiesel, A. Raghavan, Monitoring the strain evolution of lithium-ion battery electrodes using an optical fiber bragg grating sensor, Energy Technology 4 (7) (2016) 851–855, https://doi.org/10.1002/ente.201500514.
[105] J.-L. Kou, M. Ding, J. Feng, Y.-Q. Lu, F. Xu, G. Brambilla, Microfiber-based bragg gratings for sensing applications: a review, Sensors 12 (7) (2012) 8861–8876, https://doi.org/10.3390/s120708861.
[106] A. Raghavan, P. Kiesel, L.W. Sommer, J. Schwartz, A. Lochbaum, A. Hegyi, A. Schuh, K. Arakaki, B. Saha, A. Ganguli, K.H. Kim, C. Kim, H.J. Hah, S. Kim, G.-O. Hwang, G.-C. Chung, B. Choi, M. Alamgir, Embedded fiber-optic sensing for accurate internal monitoring of cell state in advanced battery management systems part 1: cell embedding method and performance, J Power Sources 341 (2017) 466–473, https://doi.org/10.1016/j.jpowsour.2016.11.104.
[107] A. Ganguli, B. Saha, A. Raghavan, P. Kiesel, K. Arakaki, A. Schuh, J. Schwartz, A. Hegyi, L.W. Sommer, A. Lochbaum, S. Sahu, M. Alamgir, Embedded fiber-optic sensing for accurate internal monitoring of cell state in advanced battery management systems part 2: internal cell signals and utility for state estimation, J Power Sources 341 (2017) 474–482, https://doi.org/10.1016/j.jpowsour.2016.11.103.
[108] E. Vergori, Y. Yu, Monitoring of Li-ion cells with distributed fibre optic sensors, Procedia Structural Integrity 24 (2019) 233–239, https://doi.org/10.1016/j.

prostr.2020.02.020.
[109] J. Peng, X. Zhou, S. Jia, S. Xu, J. Chen, Design of a sensitivity-enhanced FBG strain sensor and its application in state estimation for lithium-ion battery, in: S. Fu, J. Zhang, J. Yang (Eds.), AOPC 2019: Optical Fiber Sensors and Communication, SPIE, Beijing, China, 2019, p. 10, , https://doi.org/10.1117/12.2539787.
[110] J. Peng, X. Zhou, S. Jia, Y. Jin, S. Xu, J. Chen, High precision strain monitoring for lithium ion batteries based on fiber Bragg grating sensors, J Power Sources 433 (2019) 226692, https://doi.org/10.1016/j.jpowsour.2019.226692.
[111] W. Choi, Y. Seo, K. Yoo, T.J. Ko, J. Choi, Carbon Nanotube-Based Strain Sensor for Excessive Swelling Detection of Lithium-Ion Battery, 2019 20th International Conference on Solid-State Sensors, Actuators and Microsystems & Eurosensors XXXIII (TRANSDUCERS & EUROSENSORS XXXIII), IEEE, Berlin, Germany, 2019, pp. 2356–2359, https://doi.org/10.1109/TRANSDUCERS.2019.8808477.
[112] G.R.O. Jr, B.D. Rutkowski, S.M. BUTT, System and Method for Estimating a State of a Battery Pack, 2012, Library Catalog: Google Patents.
[113] E. Poirier, Electrified vehicle battery pack monitoring assembly and method, 2016, Library Catalog: Google Patents.
[114] C.B. Arnold, J. Cannarella, Mechanical measurement of state of health and state of charge for intercalation batteries, 2017, Library Catalog: Google Patents.
[115] E. Poirier, T.Q. Tran, B.A. Tabatowski-Bush, Sensitive strain-based SOC and SOH monitoring of battery cells, 2017, Library Catalog: Google Patents.
[116] J.Q. Xu, J. Steiber, C.M. Wall, R. Smith, C. NG, Strain measurement based battery testing, 2017, Library Catalog: Google Patents.
[117] A. Fortier, M.G. Pecht, Y. Xing, Embedded Sensors for In-Situ Cell Monitoring of Batteries, 2018, Library Catalog: Google Patents.
[118] A.G. Stefanopoulou, S.N. Mohan, Y. Kim, J.B. Siegel, Bulk force in a battery pack and its application to state of charge estimation, 2018, Library Catalog: Google Patents.
[119] J. Steiber, J.Q. Xu, Monitoring and control of electrochemical cell degradation via strain based battery testing, 2018, Library Catalog: Google Patents.
[120] L. Wang, W. Choi, K. Yoo, K. Nam, T.J. Ko, J. Choi, Stretchable Carbon Nanotube Dilatometer for *In Situ*Swelling Detection of Lithium-Ion Batteries, ACS Applied Energy Materials (2020), https://doi.org/10.1021/acsaem.0c00114. acsaem.0c00114
[121] H. Zappen, G. Fuchs, A. Gitis, D.U. Sauer, In-operando impedance spectroscopy and ultrasonic measurements during high-temperature abuse experiments on lithium-ion batteries, Batteries 6 (2) (2020) 25, https://doi.org/10.3390/batteries6020025.
[122] M. Nascimento, S. Novais, M.S. Ding, M.S. Ferreira, S. Koch, S. Passerini, J.L. Pinto, Internal strain and temperature discrimination with optical fiber hybrid sensors in li-ion batteries, J Power Sources 410–411 (2019) 1–9, https://doi.org/10.1016/j.jpowsour.2018.10.096.
[123] P. Berg, J. Soellner, A. Jossen, Structural dynamics of lithium-ion cells Part I: Method, test bench validation and investigation of lithium-ion pouch cells, Journal of Energy Storage 26 (2019) 100916, https://doi.org/10.1016/j.est.2019.100916.
[124] H. Popp, G. Glanz, K. Alten, I. Gocheva, W. Berghold, A. Bergmann, Mechanical frequency response analysis of lithium-ion batteries to disclose operational parameters, Energies 11 (3) (2018) 541, https://doi.org/10.3390/en11030541.
[125] H.L. Pham, J.E. Dietz, D.E. Adams, N.D. Sharp, Lithium-Ion Battery Cell Health Monitoring Using Vibration Diagnostic Test, Volume 4B: Dynamics, Vibration and Control, American Society of Mechanical Engineers, San Diego, California, USA, 2013, https://doi.org/10.1115/IMECE2013-63962. V04BT04A048
[126] M. Luthfi, State Estimation of Lithium Ion Battery Using Non-Invasive Method, Cartinthia University of Applied Science, Austria, 2018 Master's thesis.
[127] H.L. Pham, Health diagnosis of lithium-ion battery cell using vibration-based test and analysis, Purdue University, USA, 2013 Master's thesis.
[128] H.Y. Choi, I. Lee, J.S. Lee, Y.M. Kim, H. Kim, A study on mechanical characteristics of lithium-polymer pouch cell battery for electric vehicle, Seoul, Republic of Korea, 13–0115, 2013.
[129] R. Li, Z. Hou, L. Lu, P. Wu, Research about influence of SOC on natural frequency of pouch cells, EVS 31 & EVTeC 2018, (2018), p. 5455. Kobe, Japan
[130] P. Berg, J. Soellner, M. Herrmann, A. Jossen, Structural dynamics of lithium-ion cells Part II: investigation of large-format prismatic cells and method evaluation, Journal of Energy Storage 28 (2020) 101246, https://doi.org/10.1016/j.est.2020.101246.
[131] T. Volk, M. Winker, B. Hermann, A. Hiebl, T. Idikurt, H. Rapp, T. Kuttner, Influence of State of Charge and State of Health on the Vibrational Behavior of Lithium-Ion Cell Packs, From ancient to modern acoustics : 23rd International Congress on Sound and Vibration 2016 (ICSV 23) : Athens, Greece, 10-14July 2016 / International Institute of Acoustics & Vibration, Curran Associates, New York, 2016, p. 8. Backup Publisher: Universitt der Bundeswehr Mnchen, Fakultt fr Maschinenbau, MB 3 - Fahrzeugbau und Angewandte Mechanik, Professur: Kuttner, Thomas
[132] J. Galos, A.A. Khatibi, A.P. Mouritz, Vibration and acoustic properties of composites with embedded lithium-ion polymer batteries, Compos Struct 220 (2019) 677–686, https://doi.org/10.1016/j.compstruct.2019.04.013.
[133] R. Lammering, M. Sinapius, U. Gabbert, T. Schuster, P. Wierach, Springer International Publishing, Lamb-Wave Based Structural Health Monitoring in Polymer Composites, (2018). OCLC: 1003258873
[134] J. Achenbach, Wave Propagation in Elastic Solids. Elsevier Science, Amsterdam, 2012. OCLC: 1058394099
[135] S. Ludwig, J. Schmitt, I. Zilberman, S. Wendel, A. Jossen, New Method for Analyzing Ultrasonic based Measurements for Lithium-ion Batteries, Kraftwerk Batterie 2019, (2019). Aachen, Germany
[136] G. Davies, K.W. Knehr, B. Van Tassell, T. Hodson, S. Biswas, A.G. Hsieh, D.A. Steingart, State of charge and state of health estimation using electrochemical acoustic time of flight analysis, J Electrochem Soc 164 (12) (2017) A2746–A2755, https://doi.org/10.1149/2.1411712jes.
[137] V. Redko, V. Khandetskyy, E. Shembel, Apparatus and method for determining service life of electrochemical energy sources using combined ultrasonic and electromagnetic testing, 2010, Library Catalog: Google Patents.
[138] B. Sood, M. Osterman, M. Pecht, Health monitoring of lithium-ion batteries, 2013 IEEE Symposium on Product Compliance Engineering (ISPCE), IEEE, Austin, TX, USA, 2013, pp. 1–6, https://doi.org/10.1109/ISPCE.2013.6664165.
[139] A.G. Hsieh, S. Bhadra, B.J. Hertzberg, P.J. Gjeltema, A. Goy, J.W. Fleischer, D.A. Steingart, Electrochemical-acoustic time of flight: in operando correlation of physical dynamics with battery charge and health, Energy & Environmental Science 8 (5) (2015) 1569–1577, https://doi.org/10.1039/C5EE00111K.
[140] A.G. Hsieh, S. Bhadra, P.J. Gjeltema, D.A. Steingart, Investigating failure of li-ion batteries using in operando electrochemical-acoustic time-of-flight analysis, ECS Meeting Abstracts (2015), https://doi.org/10.1149/MA2015-02/1/85.
[141] L. Gold, T. Bach, W. Virsik, A. Schmitt, J. Müller, T.E. Staab, G. Sextl, Probing lithium-ion batteries' state-of-charge using ultrasonic transmission concept and laboratory testing, J Power Sources 343 (2017) 536–544, https://doi.org/10.1016/j.jpowsour.2017.01.090.
[142] P. Ladpli, F. Kopsaftopoulos, F.-K. Chang, Estimating state of charge and health of lithium-ion batteries with guided waves using built-in piezoelectric sensors/actuators, J Power Sources 384 (2018) 342–354, https://doi.org/10.1016/j.jpowsour.2018.02.056.
[143] P. Ladpli, C. Liu, F. Kopsaftopoulos, F.-K. Chang, Estimating Lithium-ion Battery State of Charge and Health with Ultrasonic Guided Waves Using an Efficient Matching Pursuit Technique, 2018 IEEE Transportation Electrification Conference and Expo, Asia-Pacific (ITEC Asia-Pacific), IEEE, Bangkok, Thailand, 2018, pp. 1–5, https://doi.org/10.1109/ITEC-AP.2018.8433297.
[144] P. Ladpli, C. Liu, F. Kopsaftopoulos, F.-K. Chang, Health Prognostics of Lithium-ion Batteries and Battery-Integrated Structures, Structural Health Monitoring 2019, DEStech Publications, Inc., 2019, https://doi.org/10.12783/shm2019/32215.
[145] P. Ladpli, F.-K. Chang, Battery state monitoring using ultrasonic guided waves, 2019, Library Catalog: Google Patents.
[146] J.B. Robinson, M. Maier, G. Alster, T. Compton, D.J.L. Brett, P.R. Shearing, Spatially resolved ultrasound diagnostics of Li-ion battery electrodes, PCCP 21 (12) (2019) 6354–6361, https://doi.org/10.1039/C8CP07098A.
[147] J.B. Robinson, M. Pham, M.D. Kok, T.M. Heenan, D.J. Brett, P.R. Shearing, Examining the cycling behaviour of li-ion batteries using ultrasonic time-of-flight measurements, J Power Sources 444 (2019) 227318, https://doi.org/10.1016/j.jpowsour.2019.227318.
[148] J.-J. Chang, X.-F. Zeng, T.-L. Wan, Real-time measurement of lithium-ion batteries state-of-charge based on air-coupled ultrasound, AIP Adv 9 (8) (2019) 085116, https://doi.org/10.1063/1.5108873.
[149] L. Oca, N. Guillet, R. Tessard, U. Iraola, Lithium-ion capacitor safety assessment under electrical abuse tests based on ultrasound characterization and cell opening, Journal of Energy Storage 23 (2019) 29–36, https://doi.org/10.1016/j.est.2019.02.033.
[150] Y. Wu, Y. Wang, W.K.C. Yung, M. Pecht, Ultrasonic health monitoring of lithium-ion batteries, Electronics 8 (7) (2019) 751, https://doi.org/10.3390/electronics8070751.
[151] C. Bommier, W. Chang, Y. Lu, J. Yeung, G. Davies, R. Mohr, M. Williams, D. Steingart, In operando acoustic detection of lithium metal plating in commercial licoo2/graphite pouch cells, Cell Reports Physical Science 1 (4) (2020) 100035, https://doi.org/10.1016/j.xcrp.2020.100035.
[152] B. Sood, M.G. Pecht, M.D. Osterman, Systems, methods, and devices for health monitoring of an energy storage device, 2018, Library Catalog: Google Patents.
[153] Y. Shen, Z. Deng, Y. Huang, Method and device for monitoring state of charge and state of health of lithium-ion battery, 2019.
[154] T. Ohzuku, H. Tomura, K. Sawai, Monitoring of Particle Fracture by Acoustic Emission during Charge and Discharge of LiMnO2 Cells, Journal of The Electrochemical Society 144 (10) (1997) 3496, https://doi.org/10.1149/1.1838039. Publisher: The Electrochemical Society
[155] N. Kircheva, S. Genies, D. Brun-Buisson, P.-X. Thivel, Study of solid electrolyte interface formation and lithium intercalation in Li-ion batteries by acoustic emission, J Electrochem Soc 159 (1) (2011) A18–A25, https://doi.org/10.1149/2.045201jes.
[156] N. Kircheva, S. Genies, C. Chabrol, P.-X. Thivel, Evaluation of acoustic emission as a suitable tool for aging characterization of LiAl/LiMnO2 cell, Electrochim. Acta 88 (2013) 488–494, https://doi.org/10.1016/j.electacta.2012.10.121.
[157] A. Tranchot, A. Etiemble, P.-X. Thivel, H. Idrissi, L. Rou, In-situ acoustic emission study of Si-based electrodes for Li-ion batteries, J Power Sources 279 (2015) 259–266, https://doi.org/10.1016/j.jpowsour.2014.12.126.
[158] A. Tranchot, H. Idrissi, P.-X. Thivel, L. Rou, Influence of the Si particle size on the mechanical stability of Si-based electrodes evaluated by in-operando dilatometry and acoustic emission, J Power Sources 330 (2016) 253–260, https://doi.org/10.1016/j.jpowsour.2016.09.017.
[159] N. Yoshida, T. Sakamoto, N. Kuwata, J. Kawamura, K. Sato, T. Hashida, In situ evaluation of mechanical and electrochemical degradation in silicon negative electrode for lithium-ion secondary batteries, 2016 IEEE 16th International Conference on Nanotechnology (IEEE-NANO), IEEE, Sendai, Japan, 2016, pp. 974–977, https://doi.org/10.1109/NANO.2016.7751563.
[160] S. Komagata, N. Kuwata, R. Baskaran, J. Kawamura, K. Sato, J. Mizusaki, Detection of Degradation of Lithium-Ion Batteries with Acoustic Emission Technique, Vienna, Austria, 163–167, 2010, pp. 10.1149/1.3334804.
[161] N. Beganovic, D. Söffker, Estimation of remaining useful lifetime of lithium-ion battery based on acoustic emission measurements, J Energy Resour Technol 141

(4) (2019) 041901, https://doi.org/10.1115/1.4042234.
[162] V. Cattin, P. Perichon, J. Dahmani, B. Schwartzmann, V. Heiries, Detection of electric arcs in large batteries, 2013 World Electric Vehicle Symposium and Exhibition (EVS27), IEEE, Barcelona, Spain, 2013, pp. 1–9, https://doi.org/10.1109/EVS.2013.6914873.
[163] J. Bernard, Method and system for diagnosis of the internal state of a battery through acoustic emission, 2015, Library Catalog: Google Patents.
[164] T. Yamamoto, Inspection apparatus and inspection method for lithium ion secondary battery, and secondary battery module, 2015, Library Catalog: Google Patents.
[165] K. Hojo, Device and Method to Sense Battery Internal State, 2011, Library Catalog: patentscope.wipo.int.
[166] C. Villevieille, M. Boinet, L. Monconduit, Direct evidence of morphological changes in conversion type electrodes in li-ion battery by acoustic emission, Electrochem commun 12 (10) (2010) 1336–1339, https://doi.org/10.1016/j.elecom.2010.07.014.
[167] EL-CELL, Electrochemical dilatometer, Library Catalog: el-cell.com.
[168] M. Rotter, H. Müller, E. Gratz, M. Doerr, M. Loewenhaupt, A miniature capacitance dilatometer for thermal expansion and magnetostriction, Rev. Sci. Instrum. 69 (7) (1998) 2742–2746, https://doi.org/10.1063/1.1149009.
[169] L. Inc., High Definition Fiber Optic Sensing (HD-FOS) for Optimization of Battery Thermal Management, 2015.
[170] M. Riedel, H. Hrter, Faser-Bragg-Gitter: Gefahrlos Temperaturen in einem Elektrofahrzeug bertragen, 2018, Library Catalog: www.next-mobility.news.
[171] Titan advanced energy solutions, 2020, Accessed: 2020-05-15.
[172] Feasible, inc, 2020, Accessed: 2020-05-15.
[173] S. Koch, K. Birke, R. Kuhn, Fast thermal runaway detection for lithium-ion cells in large scale traction batteries, Batteries 4 (2) (2018) 16, https://doi.org/10.3390/batteries4020016.
[174] X. Hu, Z. Jiang, L. Yan, G. Yang, J. Xie, S. Liu, Q. Zhang, Y. Xiang, H. Min, X. Peng, Real-time visualized battery health monitoring sensor with piezoelectric/pyroelectric poly (vinylidene fluoride-trifluoroethylene) and thin film transistor array by in-situ poling, J Power Sources 467 (2020) 228367, https://doi.org/10.1016/j.jpowsour.2020.228367.
[175] Chemali, Kollmeyer, Preindl, Emadi, State-of-charge estimation of li-ion batteries using deep neural networks: a machine learning approach, J Power Sources 400 (2018) 242–255.
[176] Zhang, Xia, Li, Cao, Lai, Zheng, Wang, State of the art of lithium-ion battery SOC estimation for electrical vehicles, Energies (2018).
[177] Ren, Zhao, Hong, Zhao, Wang, Zhang, Remaining useful life prediction for lithium-ion battery: a deep learning approach, IEEE Access (2018).

Appendix E

Excerpt from Conference Presentation for FRF

The following section is an excerpt from a conference presentation [62] held during the course of this thesis. The tested cell is a 12 Ah cell with NMC cathode and graphite anode. The FRF is measured using the setup from [19] in paper 1, which is extended by a laser triangulation sensor to measure the corresponding dilation (details see [62, 79]).

Fig. E.1 shows the natural frequency of the FRF, the differential voltage (eq. E.1) and the cell dilation of the LIB cell over the SOC for the charging process.

$$\frac{dV}{dq}Q_0 = \frac{d(voltage)}{d(capacity)}Q_0 = \frac{V_n - V_{n-1}}{i_n(t_n - t_{n-1}}Q_0 \tag{E.1}$$

Q_0 is the cell capacity in As and in this case is a factor to scale the differential voltage over the SOC.

The correlations between minima, maxima and the turning points in every slope is tangible. The characteristic over-voltages in the differential voltage most likely result from the different potentials from graphite intercalation. The flat regions in the slope of the dilation also indicate this behaviour. Such a plateau is found in the region between around a SOC of 60 to 30 % which correlates to findings of Rieger et al. [84], who found a plateau on a comparable cell setup in the middle region. The slope of the FRF also shows distinctive points in those regions. Those points do not overlap fully, as in contrast to the other measured values, the FRF is not measured continuously but in steps of 5 % for low and high SOC regions and 15 % for middle SOC regions. However, a trend is observable. At a SOC level of 17 % a peak in the differential voltage is found. This peak correlates with a point on the FRF curve where the FRF curve shows a significantly higher gradient. The local minimum in the differential voltage at a SOC of 70 % correlates to the maximum in the FRF. At very high SOC levels of around 95 % a minimum can be found both in the differential voltage and the FRF.

As expected, there is a correlation among the measured values. The main contributions are likely to arise from anode related phenomena. More detailed investigations are necessary to substantiate this assumption.

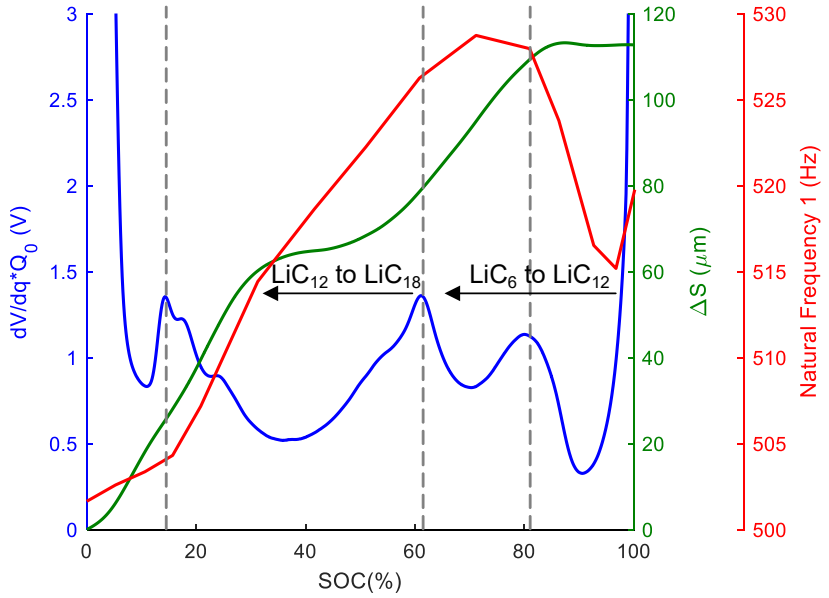

Figure E.1 Natural frequency, dilation and differential voltage over SOC for LIB pouch cell (modified with permission [62, 79]).